이학박사학위논문

Electrical control of photonic crystal lasers with graphene electrode

그래핀 전극을 이용한
광자 결정 레이저의 전기적 제어

2018년 2월

서울대학교 대학원

물리천문학부

김 한 빛

Electrical control of photonic crystal laser with graphene electrode

by
Hanbit Kim

Supervised by
Professor Heonsu Jeon

A Dissertation Submitted to the Faculty of
Seoul National University
in Partial Fulfillment of the Requirements
for the Degree of
Doctor of Philosophy

February 2018

Department of Physics and Astronomy
Graduate School
Seoul National University

Electrical control of photonic crystal lasers with graphene electrode

그래핀 전극을 이용한
광자 결정 레이저의 전기적 제어

지도교수 전 헌 수

이 논문을 이학박사 학위논문으로 제출함.
2018년 2월

서울대학교 대학원
물리천문학부
김 한 빛

김한빛의 박사학위 논문을 인준함.
2018년 2월

위 원 장 김 대 식 (인)

부 위 원 장 전 헌 수 (인)

위 원 차 국 린 (인)

위 원 이 탁 희 (인)

위 원 박 홍 규 (인)

Abstract

Electrical control of photonic crystal laser with graphene electrode

Hanbit Kim

Majoring in Physics

Department of Physics and Astronomy

The Graduate School

Seoul National University

A photonic crystal (PhC) is a structure in which two or more materials with different dielectric constants are periodically arranged with a wavelength scale of light. The light passing through the PhC has a unique light dispersion relation that cannot be seen in light passing through a homogeneous medium. One of the unique optical characteristics of PhC is the photonic band-gap and band-edge phenomenon. The photonic band-gap is a frequency region where the mode of the photon cannot exist, and a PhC cavity laser can be demonstrated in such a manner that light is strongly confined within the cavity by using the photonic band-gap. Also, by using a band-edge mode in which the group velocity of light approaches zero, the optical gain can be enhanced by a standing-wave resonance mode in the optical gain material. Thus, a PhC band-edge laser can be demonstrated.

PhC lasers have great potential in that they can be fabricated in small areas and have low power consumption. However, in order to actually use PhC lasers

in industry, modulation techniques must be preceded. Generally, the modulation speed of the PhC laser has a limitation by the modulation speed of the optical excitation method. Therefore, for high-speed modulation, it is necessary to control the optical absorption electrically. In this study, graphene is used as a light absorber. Graphene is characterized in that the carbon atoms are arranged on a two-dimensional plane and have a large light absorption rate and can control the light absorption rate by controlling the Fermi level.

In this thesis, in the first research topic, the effect of the optical absorber on the PhC laser structure was experimentally characterized. First, PhC band-edge and cavity lasers were fabricated using InGaAsP multiple-quantum-well structures, and we observed clear laser emissions around 1.5 μm. Then, graphene monolayer with the partially removed around the cavity structure was integrated on the PhC cavity laser structure. It was confirmed that as the removal region of graphene is widened, the interaction between graphene and PhC cavity mode is reduced and the output intensity of the laser is increased. In addition, it was confirmed that the single-mode laser operation of the PhC cavity laser is possible with the partially removed graphene monolayer. The characteristics of the PhC band-edge laser integrated graphene or metal patterns on the PhC band-edge laser structure were also observed. When the absorber is placed at the antinode of the resonant mode, the resonant mode is attenuated and the laser oscillation is suppressed by the strong interaction between the absorber and the resonant mode. While, when the absorber is placed at the node of the resonance mode, the interaction between the absorber and the resonance mode is not large and the laser oscillation is maintained. In addition, we confirmed that the tendency of the absorber is consistent with the results obtained by FDTD simulation. This study is meaningful in that it has experimentally characterized the effect of light absorber on the PhC resonance

mode. Further, applicability to the design of the electrode structure of the electrically driven PhC laser is expected.

In the second research topic, electrical modulation of the PhC band-edge laser was demonstrated by controlling the optical absorption of graphene monolayer on the PhC band-edge laser structure. When an electric field is applied to the graphene, the Fermi level of the graphene shifts and the absorption of light can be controlled by inhibiting the band transition. A gate voltage was applied to the graphene to observe a 1.5% of transmittance change. In this experiment, the ion-gel film used as a dielectric material has the advantage that it can be operated at a low gate voltage because of its large capacitance. Subsequently, graphene monolayer was integrated on the PhC band-edge laser structure using the change in transmittance of graphene to demonstrate the electrical modulation. Then, the electrical modulation of the PhC band-edge laser was demonstrated using the change in transmittance of graphene. When the gate voltage was not applied, the laser oscillation was suppressed due to the absorption of the resonance mode by the graphene. However, when a gate voltage of -1.0 V was applied, the laser emission was successful and the characteristics of the laser according to the gate voltage were observed. Observed characteristics are consistent with the results calculated by FDTD simulation, then we have successfully demonstrated the electrical modulation of the PhC band-edge laser. The electrical modulation of PhC band-edge laser is expected to be applied to optical system on chip technology such as optical integrated circuits.

In conclusion, in this thesis, we observed the change of the PhC resonance mode when the optical absorber is integrated on the PhC laser structure. Furthermore, the electrical modulation was demonstrated by controlling the optical absorption rate of the graphene monolayer integrated on the PhC band-

edge laser structure. The results of this study are expected to enhance understanding of the resonance mode and the PhC laser oscillation, and contribute to the application of the PhC lasers to the system on chip.

Keyword: Photonic crystal, Photonic crystal laser, Graphene,
Optical absorption, Electrical modulation, Pauli blocking

Student number: 2010-20362

Contents

List of Figures

Chapter 1

Introduction

1.1 Photonic crystals

1.1.1 Introduction

In the 20th century, the amount of information that can be processed by computers and integrated circuits, which represent the tertiary industrial revolution, has increased exponentially. But it is only the speed of technology that is rapidly increasing, and the fourth industrial revolution era demands faster information processing. Recent technology trends leading to big data processing and machine learning are approaching the limits of conventional electronic integrated circuits. An alternative to the electronic integrated circuit is a photonic integrated circuit that processes the signal with photons. In order to develop a photonic integrated circuit, a very small light source is required. VCSELs, microdisk lasers, and plasmonic lasers have been studied as light sources. Photonic crystal lasers are also being studied as one of the light sources, and their advantages are that they are very small in size and can easily control the characteristics of the light source.

The photonic crystal (PhC) is a 1D, 2D, or 3D periodic dielectric structure with a lattice constant of the wavelength of light. Figure 1-1-1 is schematics of 1D, 2D, and 3D PhC structures. A simple example of a 1D PhC is a quarter-wave stack [1]. The light of a specific wavelength incident on the quarter-wave stack causes constructive interference by a multilayer structure. Many optical devices have been developed since this principle was discovered by Lord Rayleigh in 1887 [2].

The 2D and 3D PhC structures were first introduced by E. Yablonovitch and S. John in 1987 [3,4]. The change in the periodic refractive index in the PhC plays a role of the periodic potential in the photon. If the change in the refractive index is large enough, the light of a certain frequency cannot proceed in any direction. This region is called photonic band-gap. Since the concept of photonic-band gap has been introduced, many studies about novel optics and optical devices using PhC structures have been actively conducted.

A typical structure of PhC research is a 2D slab structure. In the slab structure, light is confined by total reflection in the vertical direction and confined by the photonic band characteristics in the horizontal direction. The 2D slab structure is advantageous in that it is easy to manufacture and the PhC characteristics are clearly exhibited. In this thesis, the PhC lasers was fabricated using 2D PhC slab structure and the studies were conducted to control the characteristics of the laser.

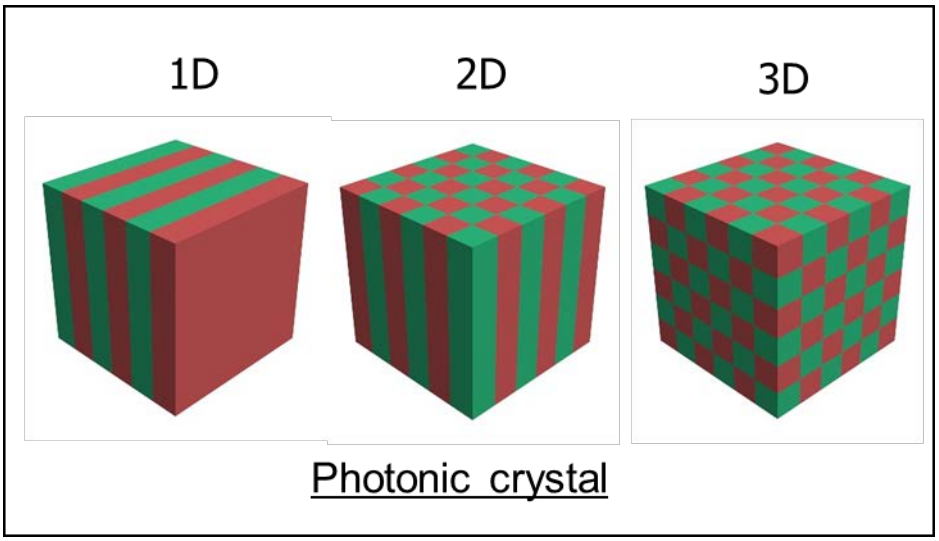

Figure 1-1-1 Simple examples of 1D, 2D, and 3D PhCs.

1.1.2 Photonic band structure

The periodic potential of photons in the PhC is similar to the periodic potential of electrons in the semiconductor crystal [5,6]. In the semiconductor crystal, the periodic Coulomb interaction by the nucleus at each lattice site affects the electrons. Electronic band structures, which mean the allowed energy states of electrons, can be derived by solving the Schrödinger equation. Similarly, in the PhC, the change in the periodic refractive index plays a role of the periodic potential in the photons. Also, photonic band structures can be derived by solving the Maxwell's equations for electromagnetic waves which propagate in the PhC. Figure 1-1-2 shows an example of photonic band structures of 2D hexagonal lattice PhC structure.

In the semiconductor crystal, the electrons in a specific energy region are inhibited from proceeding in a specific direction due to the periodic potential of the atoms. Furthermore, the electrons are inhibited in any direction if the potential is large enough to cause a complete band-gap in which electrons of a specific energy region cannot exist in the semiconductor crystal. Likewise, photonic band-gap is the important optical property of the PhC. If the change in the refractive index is large enough, the photons of a certain frequency will not be able to propagate in any direction, and this region is called a photonic band-gap. With the photonic band-gap properties, PhC cavity laser or PhC waveguide can be demonstrated.

Another important property of PhC is the near-zero group velocity of photons in a certain frequency region at the Brillouin zone edge. This band-edge property is applied to realize the devices like PhC band-edge laser or white-light LED, etc.

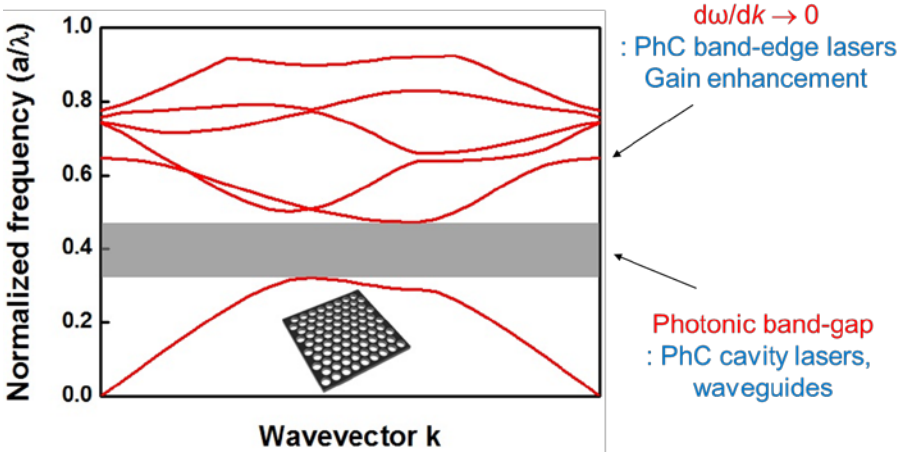

Fig. 1-1-2 Photonic band structure of a 2D hexagonal lattice PhC.

1.1.3 PhC band-edge laser

The slope of the photonic band structure corresponds to the group velocity of the photons [7]. However, the slope at the Brillouin zone edge approaches zero, which means that the group velocity of the light approaches zero. The laser with the photonic band-structure at the Brillouin zone edge of PhC is called the PhC band-edge laser. The PhC band-edge laser was first introduced by J. P. Dowling in 1994 [8]. In the photonic band-edge, as the group velocity of light approaches zero, the gain of the material obtained by the light increases greatly. The enhanced gain can lead to the photonic band-edge lasing [8-10].

PhC band-edge lasers do not have cavity structures unlike conventional lasers. Thus, the PhC band-edge laser has several unique advantages. First, the PhC band-edge laser has a large alignment tolerance in fiber-coupling because it does not have a specific cavity structure [11,12]. It is also advantageous in that it can obtain higher output power than PhC cavity laser from the spatially extended mode [13]. Since the PhC band-edge laser structure has a periodic structure without a defect, it can be fabricated using an alternative lithography technique such as laser interference lithography [13] or nanosphere lithography [14] instead of conventional E-beam lithography. An example of 2D hexagonal lattice PhC band-edge laser is shown in Fig. 1-1-3. Furthermore, it is also possible to fabricate in-plane-emitting lasers using the Brillouin zone boundary band-edge point and to fabricate surface-emitting lasers using the Brillouin zone center band-edge point.

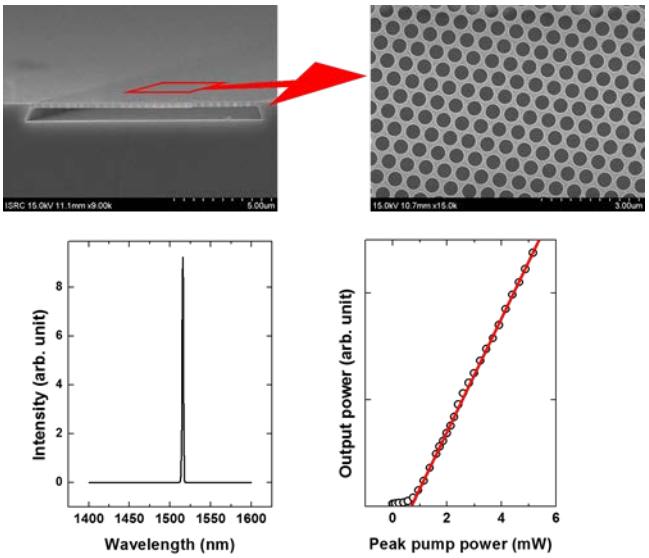

Figure 1-1-3 2D hexagonal lattice PhC band-edge laser [14].

1.1.4 PhC cavity laser

In addition to the PhC band-edge laser, the PhC cavity laser is one of the laser using the optical properties of the PhC. While the PhC band-edge laser is composed of perfectly periodic patterns, the PhC cavity laser is composed of periodic patterns and a defect structure. The PhC cavity laser has a very small size, orders of wavelength of photons, cavity and a very large Q-factor. If the cavity size is small enough to support only a single mode and the generated photons in the defect region are emitted externally through a single mode, a laser with a very low threshold can be fabricated.

Schematic of a square lattice PhC cavity laser structure is drawn in Fig. 1-1-4. The PhC cavity laser structure is formed of a periodic square-lattice PhC structure and a single defect. As shown in Fig. 1-1-4, the photons generated in the defect structure are confined laterally by the photonic band-gap and vertically by the total internal reflection due to the difference of the refractive index between the PhC slab and air-cladding. An example of a square lattice PhC cavity laser with a single defect is shown in Fig. 1-1-5.

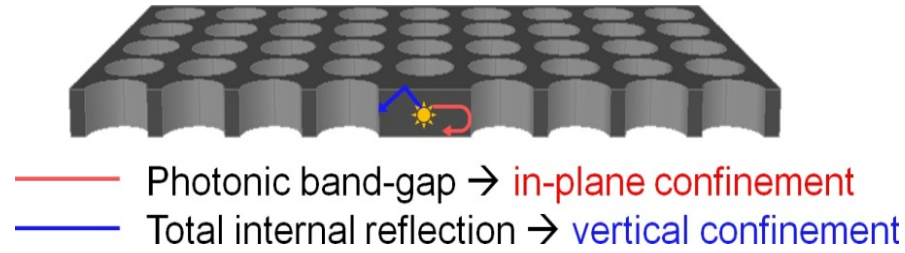

Figure 1-1-4 Schematic drawing of single-defect PhC cavity laser.

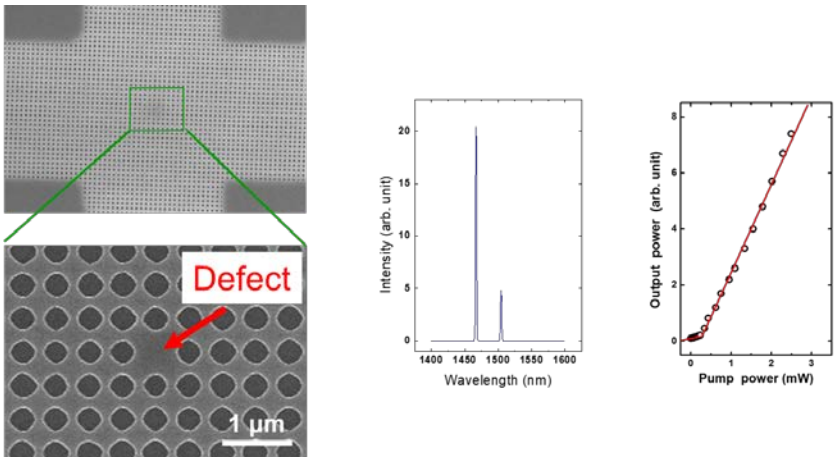

Figure 1-1-5 Single-defect PhC cavity laser [15].

1.1.5 Modulation of PhC laser

Despite the advantages of PhC lasers, there is no example yet of using PhC lasers in the industry. There are several problems to be solved for the commercialization of PhC lasers, one of which is high-speed modulation. Generally, the modulation speed of the PhC laser has a limitation by the modulation speed of the optical excitation method as shown in Fig. 1-1-6. Therefore, for high-speed modulation, electrical modulation of the PhC laser is required [16]. Then, for electrical modulation, an absorber that can control the absorption rate electrically is needed. In this study, graphene is used as a light absorber. Graphene is characterized in that the carbon atoms are arranged on a two-dimensional plane and have a large light absorption rate and can control the light absorption rate by controlling the Fermi level.

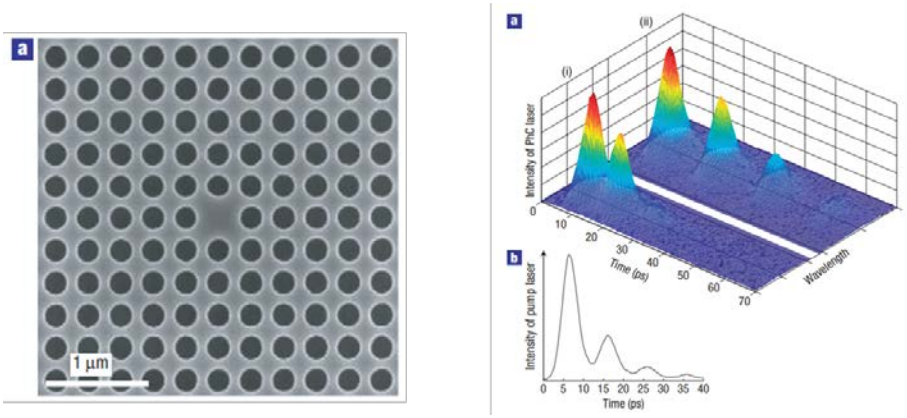

Figure 1-1-6 Ultrafast PhC nanocavity laser [15].

1.2 Graphene

1.2.1 Introduction

Graphene is an allotrope of carbon consisting of a single layer of densely packed carbon atoms arranged in a hexagonal crystalline lattice [17]. Graphene was rediscovered, isolated, and characterized in 2004 as shown in Fig. 1-1-7 by Andre Geim and Konstantin Novoselov at the University of Manchester. Within the lattice of graphene, each carbon atom has four bonds – three of σ-bonds with each of its three neighbors and one of π-bond oriented out of plane. Graphene's stability is due to its tight carbon-carbon bonding by the sp^2 orbital hybridization, consisting of the orbitals *s*, p_x and p_y that constitute the σ-bond, and p_z electron which makes up the π-bond [18].

These bonds are responsible for most of graphene's unique energy band structure, where conduction and valence bands meet at the Dirac points, so the graphene is a zero-gap semiconductor. Electrons in the graphene travel at Fermi velocity ($v_F \sim 10^6$ m/s), and act like the massless 2D Dirac fermions [19,20]. Figure 1-1-8 shows the Hall conductivity of graphene plotted as a function of carrier concentrations that represents the quantum Hall effects. Graphene also exhibits notable electron mobility ($\sim 15{,}000\ cm^2/V{\cdot}s$) with ambipolar conduction, nearly identical mobilities of electron and hole, at a high carrier density ($\sim 10^{12}\ cm^{-2}$) [21].

The behaviors of 2D Dirac fermions in graphene also lead to unique optical properties [22]. One of the unique optical property of the graphene is a high opacity for an atomic monolayer, absorbing 2.3% of the incident light at broad spectral range. The optical absorption of the graphene can be controlled by shifting the Fermi energy of the graphene by electrical gating or chemical doping.

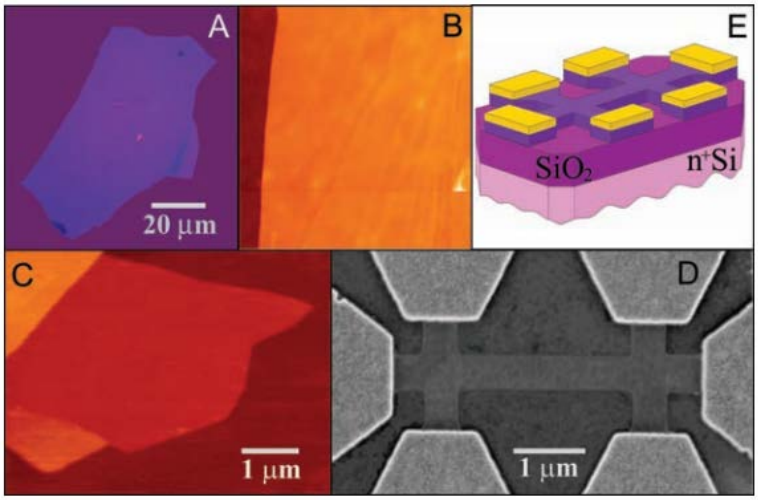

Figure 1-1-7 2D graphene films [17].

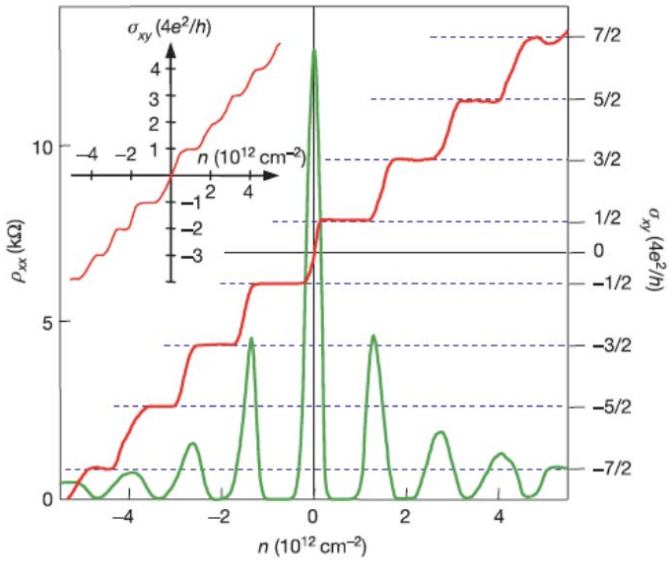

Figure 1-1-8 Quantum hall effects for massless Dirac fermions [19].

1.2.2 Optical properties of graphene

Graphene monolayer has a very high opacity of $\pi\alpha \approx 2.3\%$ of red light, where α is the fine-structure constant [23]. However, the interaction length between the optical field and the graphene is limited to the thickness of graphene, an atomic scale of ~3.3 Å, the result is that 97.7% of the optical power is transmitted without large absorption [24]. In other words, the interaction length must be increased to increase absorption by graphene. However, there is a limit to increase the interaction length by increasing the number of graphene layers.

A good strategy for increasing absorption of graphene is to use the waveguide structure [25]. The absorption rate by the interaction of graphene on the waveguide structure with the evanescent field of the waveguide mode is less than that of the normal incident light. However, the interaction length between waveguide mode and graphene can be dramatically increased. When graphene is integrated on the waveguide structure, the absorption is proportional to the waveguide length. Figure 1-1-10 shows the illustrated diagram of the optical absorption of graphene for normal incident light and waveguide mode. Many opto-electronic devices such as a graphene optical modulator [26] have been studied using a waveguide-integrated structure of graphene.

In addition, another structure for increasing the absorption of graphene is a PhC structure [27]. The resonant mode of the PhC is a kind of waveguide mode that proceeds inside a slab. Therefore, by using the interaction between graphene and the resonant mode of the PhC, graphene absorption can be greatly increased in a small area. Recently, modulation studies of PhC cavity lasers using absorption characteristics of PhCs have been published [28].

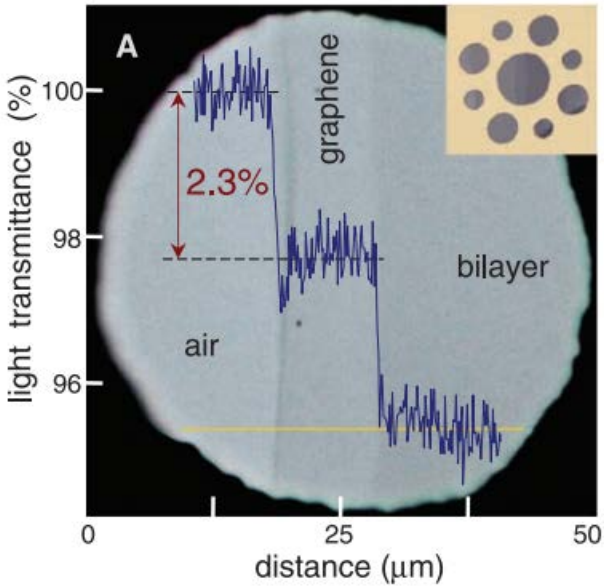

Figure 1-1-9 Transmittance of the monolayer and bilayer graphene [23].

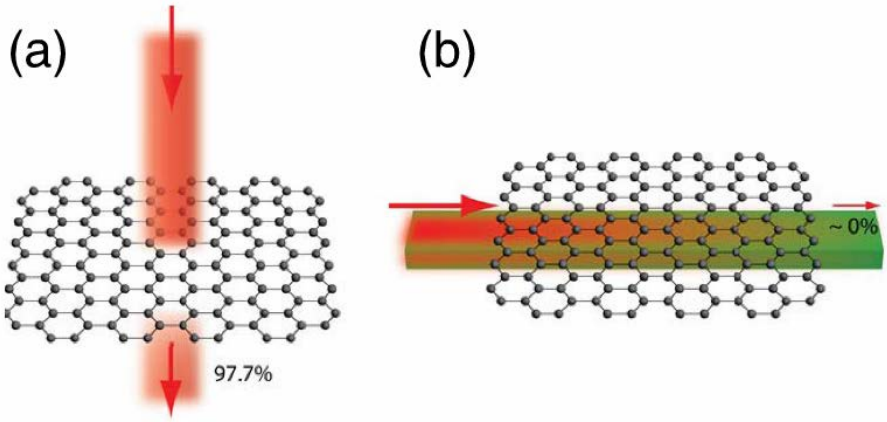

Figure 1-1-10 Illustrated optical absorption of graphene [24].

1.2.3 Opto-electronic devices using optical absorption of graphene

Graphene displays notable electron mobility (~ 15,000 $cm^2/V \cdot s$) at a high carrier density (~ 10^{12} cm^{-2}), and the resistivity of graphene monolayer would be 10^{-6} Ω·cm. Also, the 2D Dirac fermion behavior in graphene lead to unique optical properties of graphene. The most unique optical property of the graphene is a high opacity for an atomic monolayer, absorbing $\pi\alpha \approx 2.3\%$ of the incident light. The optical absorption of the graphene can be tuned by shifting the Fermi energy of the graphene by electrical gating or chemical doping. By combining novel electrical and optical properties of the graphene, graphene has emerged as a promising material for opto-electronic devices.

Although the graphene has high opacity of 2.3% by the strong light-graphene interaction, the optical absorption is still low in absolute terms to use absorption properties for real devices. To apply the absorption properties of graphene to opto-electronic applications, many studies have been conducted to increase the absorption of graphene. As a result, several studies and prototypes have been reported in recent years, such as optical modulators [26], mode-locked laser with graphene as a saturable absorbers (as shown in Fig. 1-1-11) [29], and photodetectors (as shown in Fig. 1-1-12) [30,31]. The combination of photonics and graphene will serve as an opportunity to expand the area of advanced photonic devices.

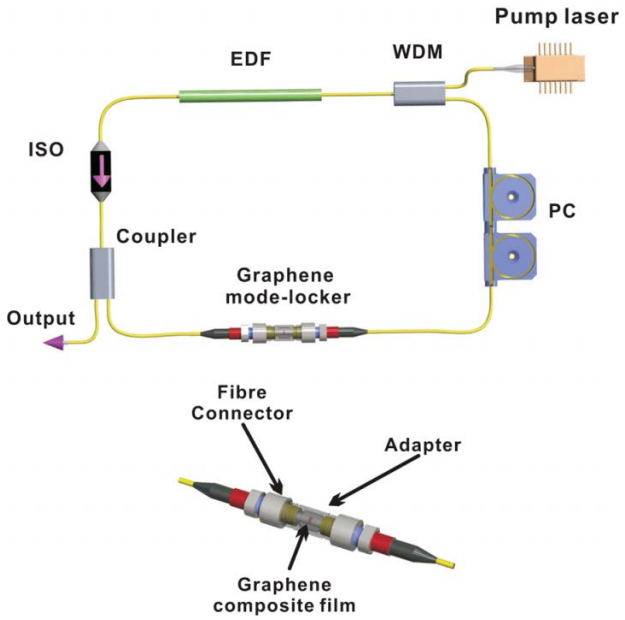

Figure 1-1-11 Graphene mode-locked ultrafast laser [29].

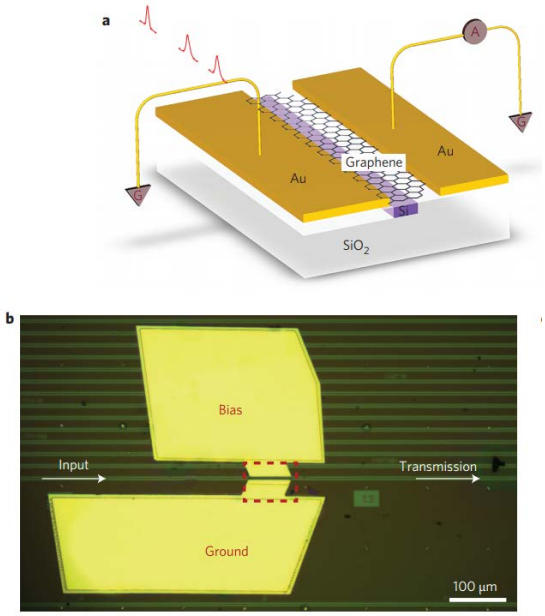

Figure 1-1-12 Chip-integrated ultrafast graphene photodetector with high responsivity [31].

1.3 Computational Method

1.3.1 Plane wave expansion method

The plane wave expansion (PWE) method represents a computational simulation technique in electromagnetism that solves the eigenvalue problems of the Maxwell's equations. The solution of the homogeneous Helmholtz equation has a plane wave form which is the basis for a periodic media. The PWE method is based on the Bloch theorem, the electric field (E-field) or magnetic field (H-field) can be expanded into appropriate Fourier series along their reciprocal lattice vector. Likewise, the dielectric permittivity is also expanded into the Fourier series. Then, these Fourier series equations replace infinite-dimensional matrix eigenvalue problems that can be solved with the appropriate approximation.

Among the PhC community, PWE method is a very powerful tool for calculating the photonic band structure [32]. Also, PWE is useful for calculating modal solutions of Maxwell's equations for inhomogeneity or periodic geometry.

1.3.2 Finite-difference time-domain method

The finite difference time domain method (FDTD) is one of the most powerful computational methods for solving electromagnetic problems in the PhC research. Unlikely the PWE method, FDTD methods solve the Maxwell’s equations directly, and provide straightforward models for arbitrary structures. Furthermore, FDTD methods deal with the time-domain terms, so, it can cover a wide frequency band with a single simulation run.

The FDTD method can be classified as a grid-based differential time-domain numerical modeling method [33]. Time-dependent Maxwell's equations are discretized to the space and time partial derivatives. The finite-difference equations are solved in a leap-frog manner. The vector components of the E-field in a volume of space are solved at a given instant in time; then the vector components of the H-field in the same spatial volume are solved at the next instant in time; and the process iterates repeatedly until the steady-state electromagnetic behavior is fully converged.

1.4 Outline of the Manuscript

In this thesis, I introduced the optical absorbers such as graphene and metal on the PhC laser structure. The absorber interacts with the resonant mode of the PhC, and as a result, the characteristics of the PhC lasers change. The goal of this study is to observe and control the change of the PhC lasers.

In chapter 2, I will discuss the effect of the optical absorber on the PhC resonance mode. Three experiments were conducted to investigate the effect of the optical absorber. Each experiment is designed to observe the effect of the optical absorber on the PhC resonance mode. I will introduce each experiment and discuss the results.

In chapter 3, I will describe the electrical modulation of the PhC laser with graphene monolayer. First, we will observe the change in transmittance of graphene monolayer by electrolyte gating. Next, the graphene-integrated PhC laser structure will be described. Also, I will discuss the PL measurement results of PhC laser according to the gate voltage. Then, I will analyze the modulation characteristics.

Finally, in chapter 4, the conclusion and the perspectives will be presented.

References

[1] P. Yeh, *Optical Waves in Layered Media* (Wiley 2005).

[2] J. W. Strutt (Lord Rayleigh), "On the maintenance of vibrations by forces of double frequency, and on the propagation of waves through a medium endowed with a periodic structure," Philosophical Magazine Series **5**, 145-159 (1887).

[3] E. Yablonovitch, "Inhibited spontaneous emission in solid-state physics and electronics," Physics Review Letters **58**, 2059-2062 (1987).

[4] S. John, "Strong localization of photons in certain disordered dielectric superlattices," Physics Review Letters **58**, 2486-2489 (1987).

[5] K. Inoue, and K. Ohtaka, *Photonic Crystals: Physics, Fabrication and Applications* (Springer 2004).

[6] J. D. Joannopoulos, S. G. Johnson, J. N. Winn, and R. D. Meade, *Photonic Crystals: Molding the Flow of Light* (Princeton University Press 2008).

[7] K. Inoue and K. Ohtaka, Photonic Crystals: Physics, Fabrication and Applications (Springer, 2004).

[8] J. P. Dowling, M. Scalora, M. J. Bloemer, C. M. Bowden, "The photonic band edge laser: A new approach to gain enhancement," Journal of Applied Physics **75**, 1896-1899 (1994).

[9] S. Nojima, "Optical-gain enhancement in two-dimensional active photonic crystals," Journal of Applied Physics **90**, 545-551 (2001).

[10] M. Imada, S. Noda, A. Chutinan, T. Tokuda, M. Murata, and G. Sasaki, "Coherent two-dimensional lasing action in surface-emitting laser with triangular-lattice photonic crystal structure," Applied Physics Letters **75**, 316-318 (1999).

[11] Y. Park, S. Kim, C. Moon, H. Jeon, and H. J. Kim, "Butt-end fiber coupling to a surface-emitting Γ-point photonic crystal band edge laser," Applied Physics Letters **90**, 171115 (2007).

[12] S. Kim, Y. Park, K. Hwang, J. Lee, H. Jeon, and H. J. Kim, "High-power and large-alignment-tolerance fiber coupling of honeycomb-lattice photonic crystal Γ-point band-edge laser," Journal of the Optical Society of America B **26**, 1330-1333 (2009).

[13] S. Kim, S. Ahn, J. Lee, H. Jeon, P. Regreny, C. Seassal, E. Augendre, and L. D. Cioccio, "Milliwatt-level fiber-coupled laser power from photonic crystal band-edge laser," Optics Express **19**, 2105-2110 (2011)

[14] S. Ahn, H. Kim, H. Jeon, J. Oh, Y. Do, and H. Kim, "Two-dimensional hexagonal lattice photonic crystal band-edge laser patterned by nanosphere lithography," Applied Physics Express **5**, 042102 (2012)

[15] S. Ahn, S. Kim, and H. Jeon, "Single-defect photonic crystal cavity laser fabricated by a combination of laser holography and focused ion beam lithography," Applied Physics Letters **96**, 131101 (2010)

[16] H. Altug, D. Englund, and J. Vuckovic, "Ultrafast photonic crystal nanocavity laser," Nature Physics **2**, 484-488 (2006)

[17] K. S. Novoselov, A. K. Geim, S. V. Morozov, D. Jiang, Y. Zhang, S. V. Dubonos, I. V. Grigorieva, and A. A. Firsov, "Electric Field Effect in Atomically Thin Carbon Films," Science **306**, 666-669 (2004).

[18] A. H. C. Neto, F. Guinea, N. M. R. Peres, K. S. Novoselov, and A. K. Geim, "The electronic properties of graphene," Reviews of Modern Physics **81**, 109-162 (2009)

[19] K. S. Novoselov, A. K. Geim, S. V. Morozov, D. Jiang, M. I. Katsnelson, I. V. Grigorieva, S. V. Dubonos, and A. A. Firsov, “Two-dimensional gas of massless Dirac Fermions in graphene,” Nature Nature **438**, 197-200 (2005)

[20] K. I. Bolotin, K. J. Sikes, Z. Jiang, M. Klima, G. Fudenberg, J. Hone, P. Kim, and H. L. Stormer, "Ultrahigh electron mobility in suspended graphene," Solid State Communications **146**, 351-355 (2008).

[21] K. S. Novoselov, V. I. Fal’ko, L. Colombo, P. R. Gellert, M. G. Schwab, and K. Kim, “A roadmap for graphene,” Nature **490**, 192-200 (2012)

[22] F. Bonaccorso, Z. Sun, T. Hasan, and A. C. Ferrari, “Graphene photonics and optoelectronics,” Nature Photonics 4, 611-622 (2010)

[23] R. R. Nair, P. Blake, A. N. Grigorenko, K. S. Novoselov, T. J. Booth, T. Stauber, N. M. R. Peres, and A. K. Geim, "Fine Structure Constant Defines Visual Transparency of Graphene," Science **320**, 1308 (2008).

[24] H. Li, Y. Anugrah, S. J. Koester, and M. Li, "Optical absorption in graphene integrated on silicon waveguides," Appl. Phys. Lett. **101**, 111110 (2012)

[25] S. J. Koester, and M. Li, “Waveguide-Coupled Graphene Optoelectronics,” IEEE Journal of selected topics in quantum electronics **20**, 84-94 (2014)

[26] M. Liu, X. Yin, E. Ulin-Avila, B. Geng, T. Zentgraf, L. Ju, F. Wang, and X. Zhang, "A graphene-based broadband optical modulator," Nature **474**, 64-67 (2011).

[27] X. Gan, K. Mak, Y. Gao, Y. You, F. Hatami, J. Hone, T. Heinz, D. Englund, "Strong Enhancement of Light–Matter Interaction in Graphene Coupled to a Photonic Crystal Nanocavity," Nano Letter **12**, 5626-5631 (2012).

[28] M. Hwang, H. Kim, K. Kim, K. Jeong, J. Park, J. Choi, J. Kang, J. Lee, W. Park, J. Song, M. Seo, and H. Park, "Switching of Photonic Crystal Lasers by Graphene," Nano Letter **17**, 1892-1898 (2017).

[29] Z. Sun, T. Hasan, F. Torrisi, D. Popa, G. Privitera, F. Wang, F. Bonaccorso, D. M. Basko, and A. C. Ferrari, “Graphene mode-locked ultrafast laser,” ACS Nano **4**, 803-810 (2010)

[30] F. Xia, T. Mueller, Y. Lin, A. Valdes-Garcia, and P. Avouris, "Ultrafast graphene photodetector," Nature Nanotechnology **4**, 839-843 (2009).

[31] X. Gan, R. Shiue, Y. Gao, I. Meric, T. F. Heinz, K. Shepard, J. Hone, S. Assefa, and D. Englund, “Chip-integrated ultrafast graphene photodetector with high responsivity,” Nature Photonics **7**, 883-887 (2013)

[32] S. Shi, C. Chen, and D. W. Prather, “Plane-wave expansion method for calculating band structures of photonic crystal slabs with perfectly matched layers,” Journal of the Optical Society of America A **21**, 1769-1775 (2004)

[33] K. S. Yee, “Problems involving Maxwell’s equations in isotropic media,” IEEE Transactions on Antennas and Propagation **14**, 802-807 (1966)

Chapter 2

Experimental characterization of modal absorption of PhC laser affected by the patterned electrode

2.1 Introduction

The absorption rate of light perpendicular to graphene monolayer is only 2.3% [1] due to very short interaction length (3.3 Å). However, when graphene is integrated on the waveguide structure, absorption of the waveguide mode can be increased by increasing the interaction length between waveguide mode and graphene [2]. In this case, absorption of waveguide mode by graphene monolayer occurs to 0.1-0.2 dB/μm. A loss of 0.2 dB/μm means that 99% waveguide mode is absorbed in a 100-μm-long waveguide structure. Studies, such as the optical modulators [3-4] and photodetectors [5-6], have been conducted in a way to increase absorption by using waveguide structures.

Meanwhile, another study to increase light interaction with graphene uses PhC structures [7]. According to Ref. 7, they reduced the cavity reflection by over 100 times with the strong coupling between localized mode in the PhC nanocavity and graphene. Using the PhC structure, a large absorption can be obtained in a compact region than the waveguide structure.

Also, we can think of the strong coupling between graphene and PhC modes to

extend to the active device – PhC laser. When graphene is integrated on a PhC laser structure, it can be expected that the resonance mode will be absorbed due to the strong coupling between the graphene and the PhC mode, thereby suppressing laser emission. However, by controlling the absorption of graphene integrated on PhCs, researchers observed the optical properties in the PhC structure [8] or fabricated a photonic device [9].

Figure 2-1-1 is a SEM image of honeycomb lattice PhC band-edge laser structure with graphene sheet for experimental verification of optical absorption in PhC resonant mode by graphene. It can be seen that the graphene is well transferred without damage to the PhC band-edge laser structure. The results of the PL measurement of the fabricated samples are shown in the Fig. 2-1-2. In the structure without graphene, a sharp laser peak can be observed. However, as expected, no laser signal could be observed when graphene was integrated on the PhC band-edge laser structure. In other words, the absorption of resonance mode by graphene was observed experimentally in the PhC band-edge laser structure.

In this study, we aim to observe the characteristics of PhC lasers when there is the light absorber on the PhC laser structure, and to observe the changes in the characteristics of the PhC lasers when the light absorber changes.

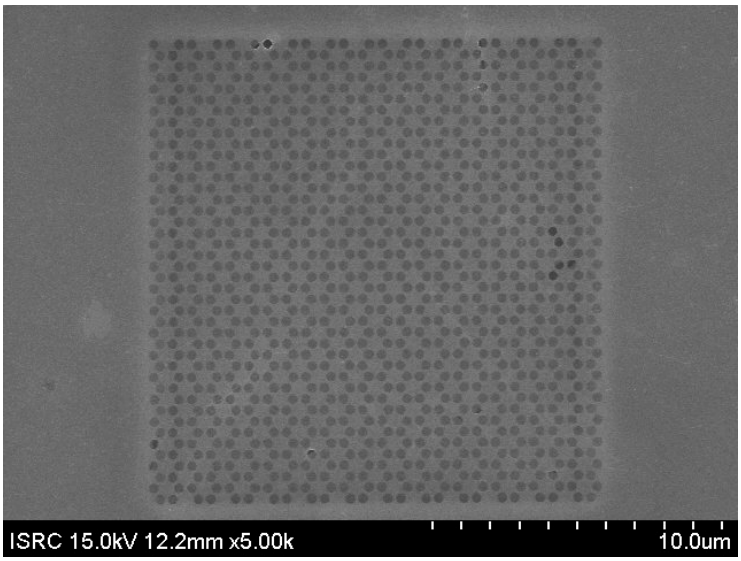

Figure 2-1-1 SEM image of honeycomb lattice PhC band-edge laser structure with graphene sheet.

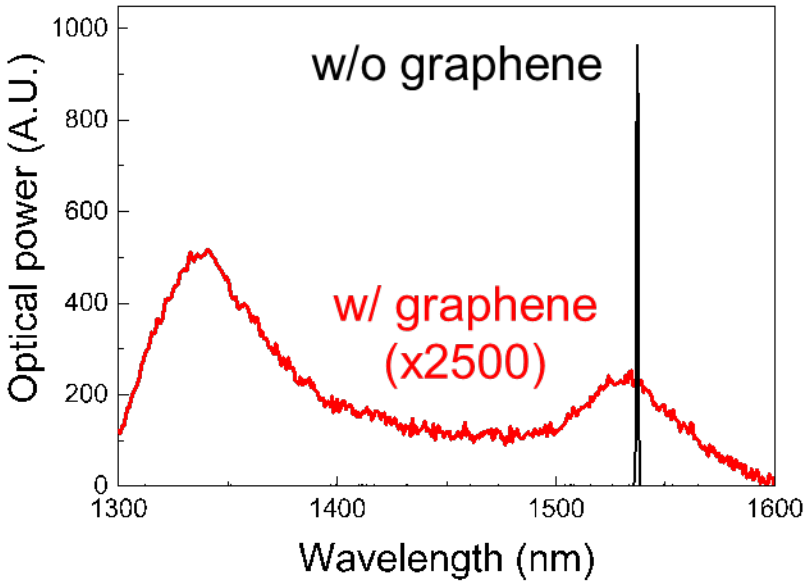

Figure 2-2-2 Measured PL spectra of PhC band-edge laser before transferring graphene and after transferring graphene.

2.2 Effect of PhC cavity laser on window pattern of graphene

2.2.1 Introduction

The PhC L3 cavity has a cavity mode with a very high Q-factor [10]. Figure 2-2-1 shows the resonance mode of the PhC L3 cavity. As can be seen, the cavity mode is focused at the center of the PhC pattern. Therefore, if the center area of the graphene covering the entire PhC pattern is etched, the interaction between the graphene and the cavity mode can be changed, and as a result, the characteristics of the PhC cavity laser can be expected to change.

In this experiment, we investigated the characteristics of the PhC cavity laser by varying the area of the window pattern at the center of graphene.

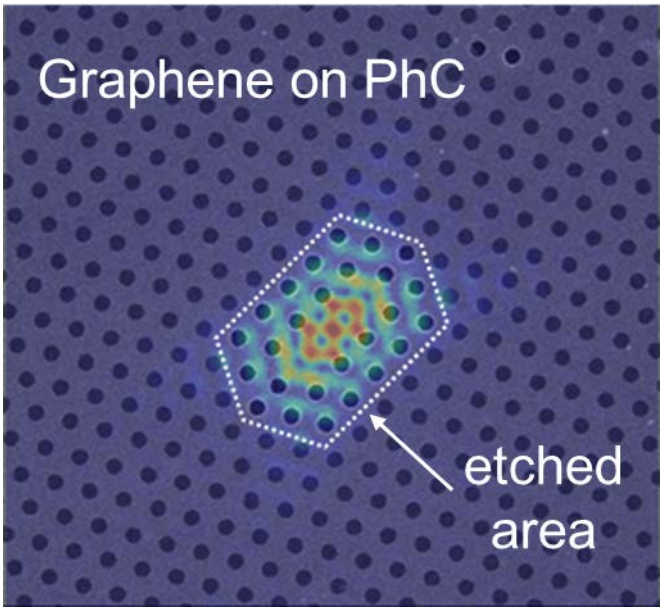

Figure 2-2-1 Schematic of PhC cavity mode and graphene with window pattern.

2.2.2 Interaction between cavity mode and graphene

To observe the change in the characteristics of the PhC cavity laser, samples were designed as shown in Fig. 2-2-2. A sample with all-graphene-covered (sample#0) and all-graphene-removed (sample#7) was set as a reference, and the sample was classified into six samples (sample#1 - #6) according to the size of the window pattern. The characteristics of the PhC cavity lasers were measured for each sample.

The absorption of light by graphene can be expressed as the product of the intensity of the electric field parallel to the graphene plane and the optical conductivity of the graphene [11]. To determine the degree of absorption intensity of the cavity mode by graphene, we calculated the overlap factor to see how the graphene and cavity mode overlap. If the overlap factor is 100% when the PhC pattern is all covered with the graphene and the overlap factor is 0% when the graphene is removed entirely, the overlap factors between the two reference samples are as shown in Fig 2-2-2. It can be seen that the overlap factor decreases sharply as the area of the window pattern is widened.

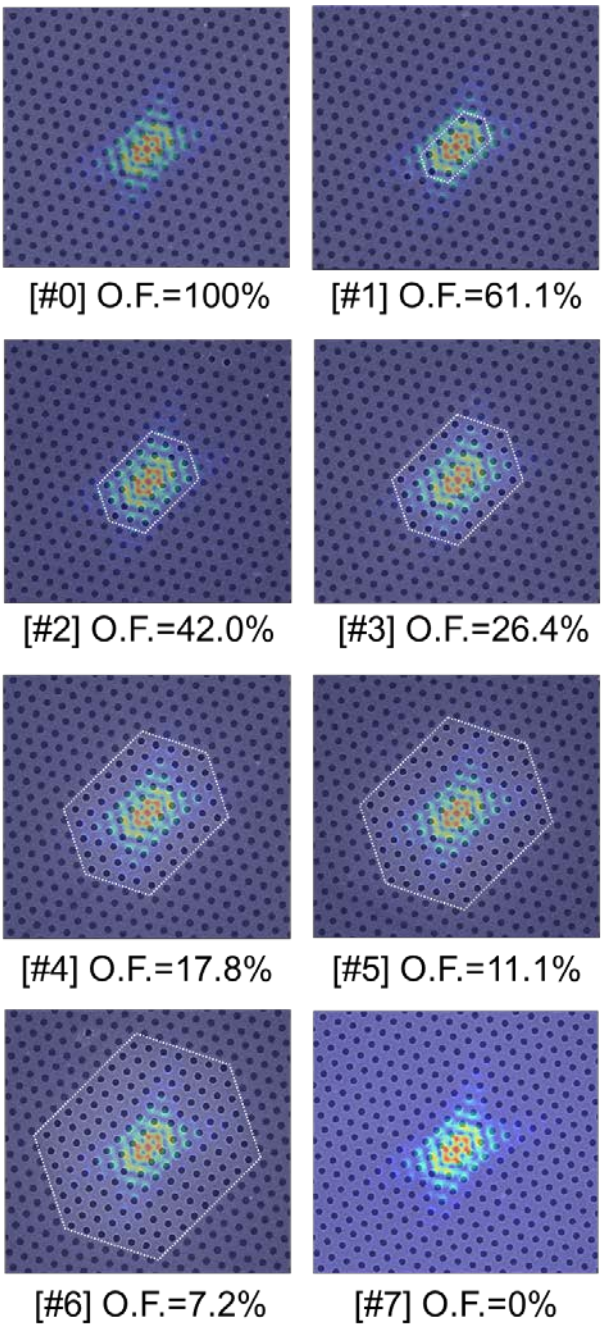

Figure 2-2-2 Designs of the window patterns of graphene and calculated overlap factors of various samples.

2.2.3 Device fabrication

Figure 2-2-3 shows the SEM images of the fabricated PhC cavity laser structures integrated with graphene layer with the window patterns. In the SEM image, the area that looks bright is the part where graphene is removed. It can be seen that the graphene pattern is clear and well-formed without any damage.

Device fabrication began with the deposition of a 50-nm-thick Si_3N_4 hardmask layer on a semiconductor epistructure, composed of a 230-nm-thick InGaAsP multi-quantum well layer (MQW) and a 1000-nm-thick InP sacrificial layer, using plasma-enhanced chemical vapor deposition (PECVD) method. An array of PhC L3 cavity patterns were generated by electron-beam lithography. The period of triangular lattice structure was 500 nm while the air-hole radius was 0.25*a*. The size of each PhC pattern was ~20×20 μm^2. The PhC patterns were transferred down to the Si_3N_4 and MQW layers sequentially by reactive-ion etch (RIE) using the gas mixtures of O_2/CF_4 and CH_4/H_2, respectively. Then, wet-etching was performed at 4°C using hydrochloric acid (HCl) aqueous solution (3:1) to selectively remove the InP sacrificial layer, which resulted in a completed PhC cavity laser sample in a free-standing membrane form.

A monolayer graphene sheet, which was grown on a Cu foil by thermal chemical vapor deposition (TCVD) method. After a PMMA layer was spin-coated directly on the graphene sheet as a temporary handling layer, we removed the Cu foil in a $FeCl_3$ solution to obtain in a free-standing PMMA/graphene film floating on water. The PMMA/graphene film was then transferred onto the PhC cavity laser sample. Next, window pattern was formed on graphene by electron-beam lithography using PMMA as E-beam resist. The graphene of the window part was removed by O_2 plasma. The etching conditions using O_2 plasma are as follows. The etching time was 7 seconds, the power was 50 W, the flow rate of O_2 gas was 20 sccm, and the pressure of the chamber was 132 mTorr. Then, the PMMA layer was removed with acetone.

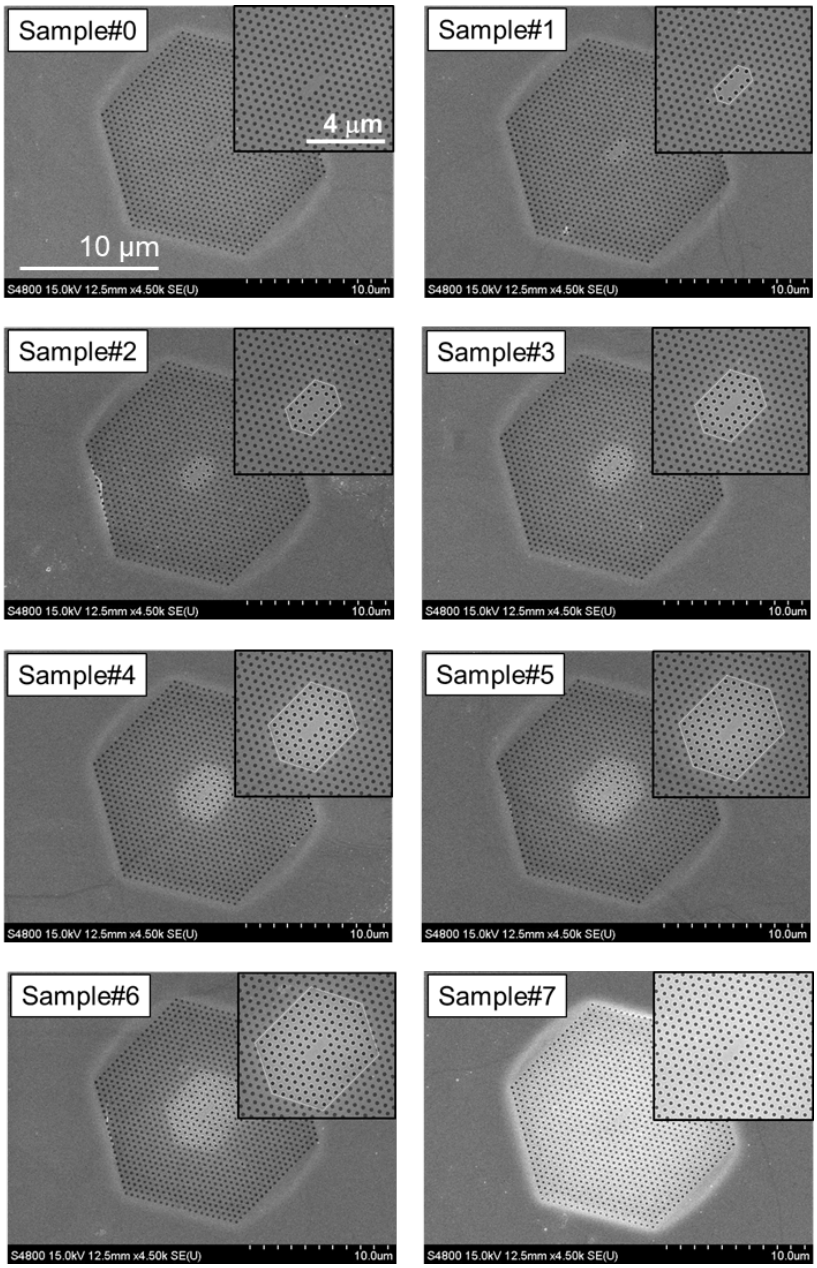

Figure 2-2-3 SEM images of fabricated PhC cavity lasers with window patterns. Insets are magnified images of defects of PhC laser structures and window patterns of graphene.

2.2.4 Measured PL spectra

Figure 2-2-4 is the result of PL measurement for the fabricated sample. Except for reference samples where graphene covered all PhC patterns, all PhC cavity lasers were successful. The graph showing peak intensity for easy comparison of the laser output is shown in Fig. 2-2-5. The intensity of the laser emission increases as the area of the window pattern increases, but the intensity of the laser emission saturates after the third sample (sample #3).

Figure 2-2-6 shows the threshold density measurement for each sample to clearly compare the tendency with window size. Similar to the previous intensity measurement, the threshold density decreased until the sample #3 and then saturated. It was experimentally confirmed that the interaction between graphene and cavity mode is no longer significant from the sample #3.

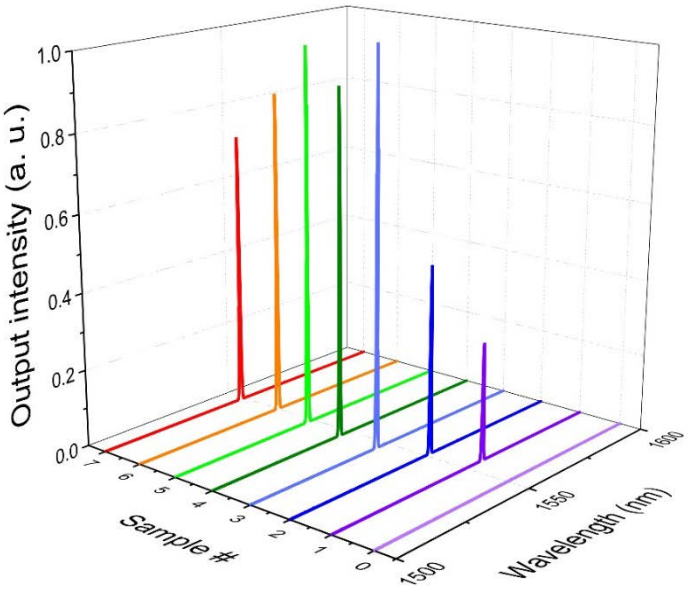

Figure 2-2-4 Measured PL spectra of PhC cavity laser with various areas of window patterns on the graphene.

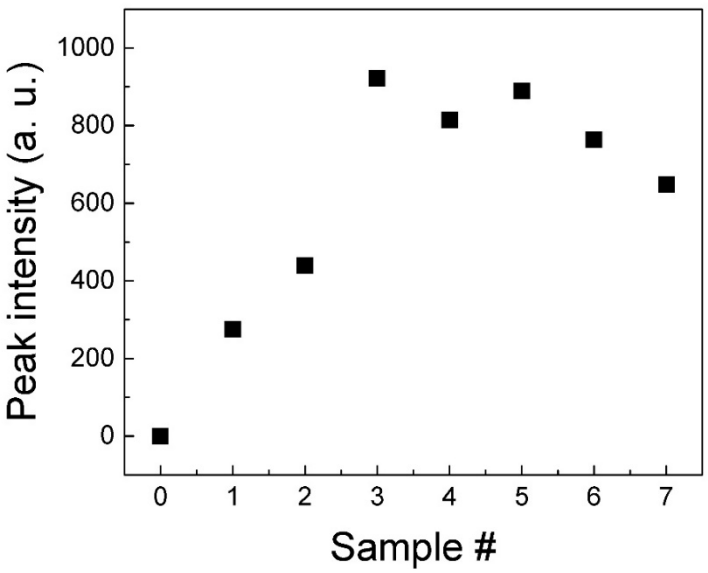

Figure 2-2-5 Measured peak intensity of PhC cavity laser with various areas of window patterns on the graphene.

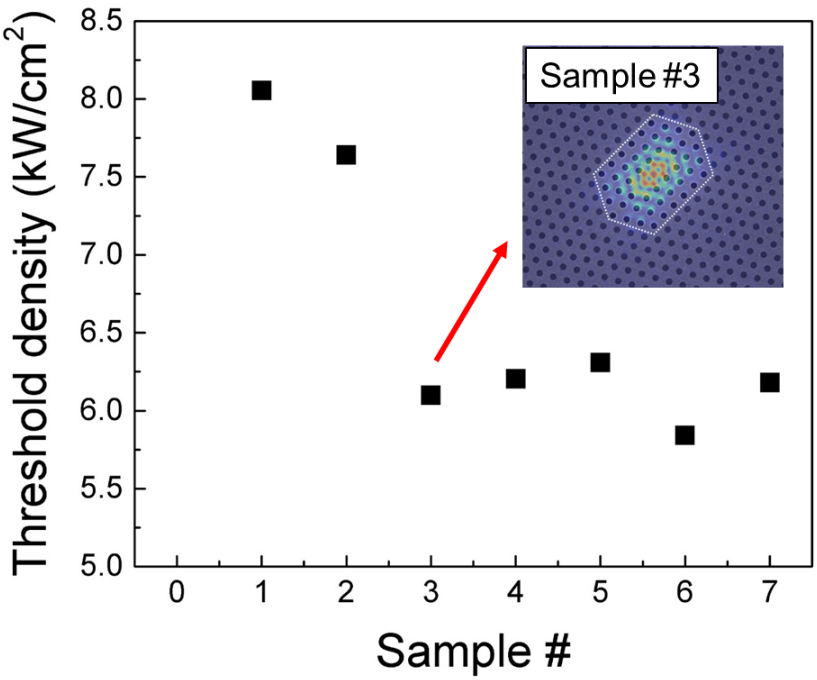

Figure 2-2-6 Measured threshold density of PhC cavity laser with various areas of window patterns on the graphene.

2.2.5 Single-mode operation of PhC laser with window-patterned graphene

In the PhC cavity structure, the cavity laser emits by the cavity mode at the central region of the PhC pattern emits, but the band-edge mode emits due to the periodic structure of the peripheral region of the PhC pattern. There are PhC cavity modes inside the photonic band-gap, and a photonic band-gap necessarily exists between the two band-edges. Therefore, the PhC cavity modes always have band-edge modes close together. In general, PhC cavity lasers have lower threshold than PhC band-edge lasers, but both modes oscillate according to excitation condition [12]. Figure 2-2-7 shows the multi-mode lasing where both PhC cavity and band-edge mode lasers are oscillated simultaneously. Sometimes, however, single-mode laser operation is important in terms of optical signaling.

In this case, graphene sheet with a window pattern can be helpful in a single-mode laser operation of PhC cavity lasers. The graphene, which reduces the overlap region with the cavity mode, does not interfere with the oscillation of the PhC cavity laser because the interaction with the cavity mode is not large. However, it still has a large interaction with the band-edge mode due to the periodic structure of the periphery of the PhC structure. Therefore, laser oscillation at band-edge mode suppressed by graphene, and PhC cavity lasers enable single-mode laser operation only in cavity mode. Figure 2-2-8 is the result of a PL measurement in a PhC cavity structure with graphene sheet with a window pattern. In comparison with the results of Fig. 2-2-7, it is experimentally observed that band-edge mode laser is suppressed and only single-mode laser operates by cavity mode.

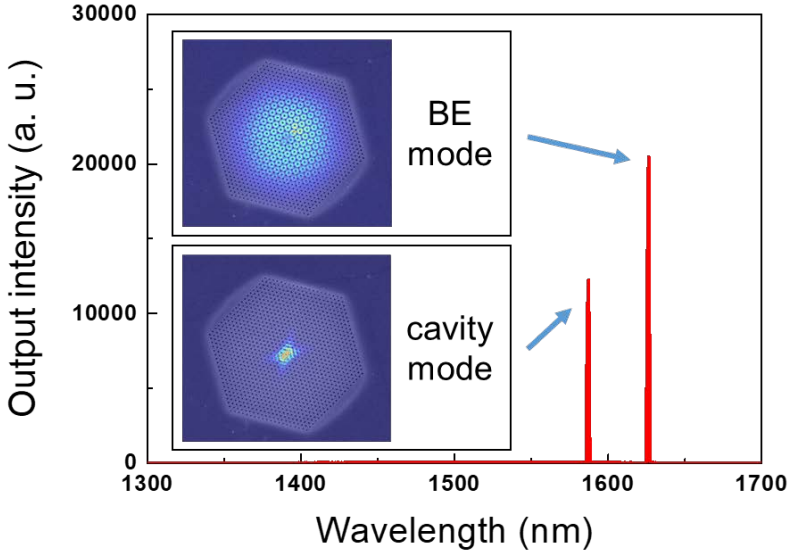

Figure 2-2-7 Two laser peaks of PhC cavity laser due to cavity mode at the center of PhC pattern and band-edge mode at the boundary of PhC pattern.

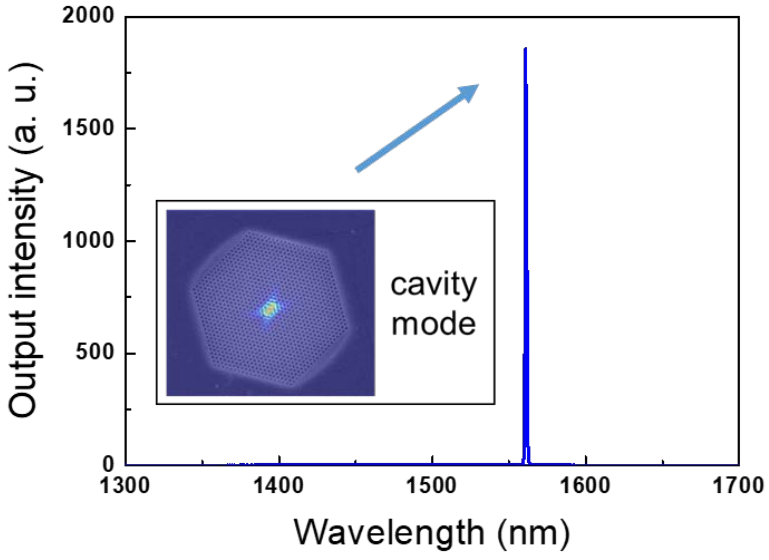

Figure 2-2-8 Single-mode operation of PhC cavity laser with window patterned graphene.

2.3 Effect of PhC band-edge laser on grating pattern of graphene

2.3.1 Introduction

PhC band-edge laser is a laser using slow light near the photonic band-edge in periodic PhC structure without defect structure [13]. The PhC band-edge laser structure has a periodic standing-wave resonance mode [14]. Therefore, the PhC band-edge resonance mode exhibits antinodes with relatively strong intensities and nodes with relatively weak intensities periodically. Figure 2-3-1 is the transverse electric field profile of the resonance mode at the Γ_1-point band-edge of the square lattice PhC structure. The red colors represent antinodes with the high electric field and the blue colors represent nodes with the low electric field.

Since the PhC band-edge mode appears in the entire region of the PhC pattern, it is not possible to reduce the interaction between the band-edge mode and the graphene by using the window pattern as in the cavity mode. Instead, it is possible to reduce interaction between band-edge mode and graphene by using periodically appearing nodes of the PhC band-edge mode. Figure 2-3-2 and 2-3-3 are schematics of an array of graphene grating patterns located at the antinodes and nodes of the resonant mode at the Γ_1-point band-edge of the square lattice PhC structure. In both cases, the area of the graphene gratings on the PhC pattern is the same, but the interactions between the graphene gratings and the standing-wave formed resonance mode can be expected to be very different.

In this experiment, it is aimed to experimentally verify the characteristics of the standing-wave-formed resonance mode of the PhC band-edge laser by comparing the characteristics of PhC band-edge lasers when grating patterns of graphene are located at the antinodes and at the nodes of the resonant mode.

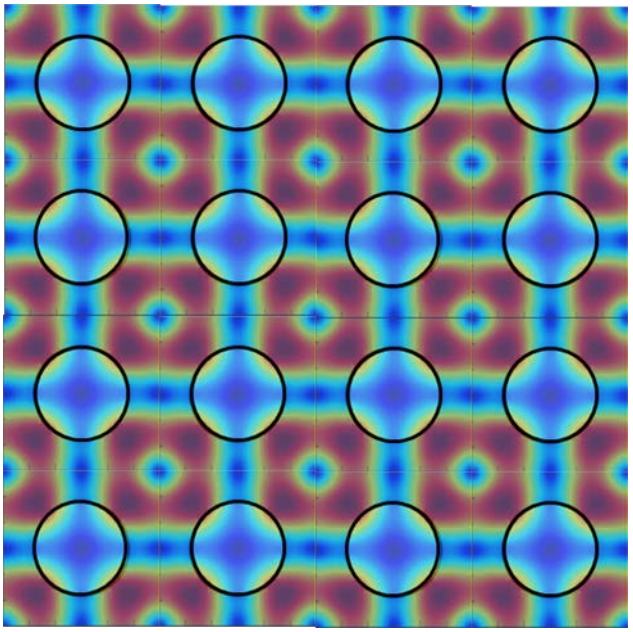

Figure 2-3-1 Resonance mode at the Γ_1-point band-edge of the square lattice PhC structure

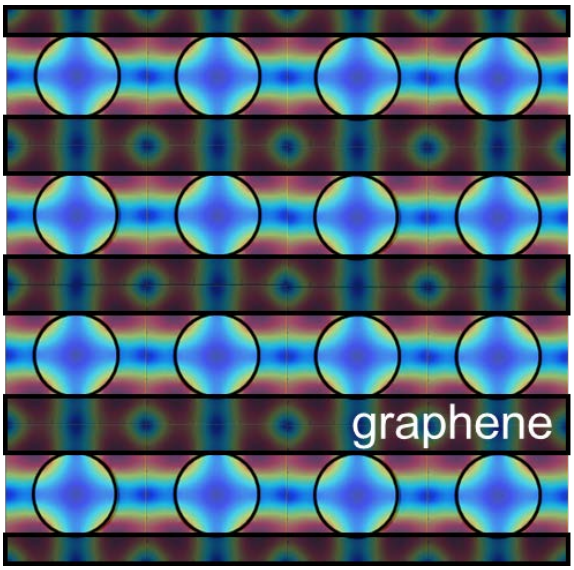

Figure 2-3-2 Schematic of the graphene gratings on the antinode of the Γ_1 band-edge mode of the square lattice PhC structure

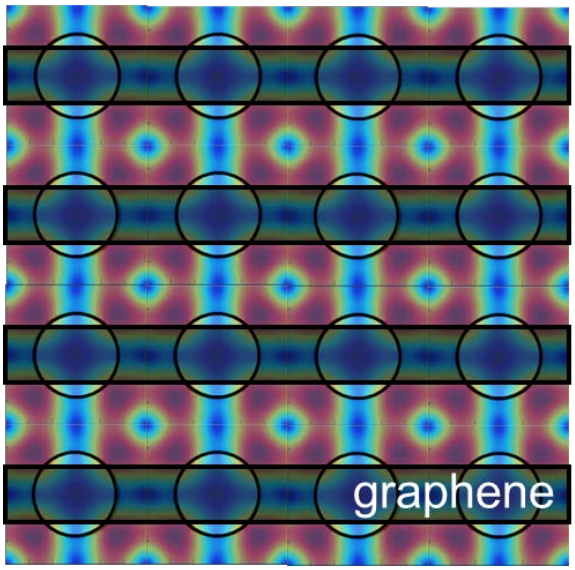

Figure 2-3-3 Schematic of the graphene gratings on the antinode of the Γ_1 band-edge mode of the square lattice PhC structure

2.3.2 Calculation of Q-factors and optical absorptions

In the case of arranging the graphene grating patterns on the antinodes and nodes of the resonant mode, the change of intensity of the resonant mode was calculated respectively using the FDTD method.

A high Q-factor in PhCs means that light in the structure is difficult to escape [15]. That is, Q-factor and decay rate are inversely related to each other. Therefore, the decrease in Q-factor should be larger when the absorption is large. The changes in Q-factor by the width of graphene gratings calculated by FDTD simulations for both cases are shown in Fig 2-3-4. As expected, as the width of the gratings increases, the Q-factor decreases rapidly when the graphene pattern is located at the antinode, whereas it gradually decreases when it is located at the node.

On the other hand, the absorption by graphene can be directly calculated by using the optical conductivity of graphene. In general, the optical absorption of a graphene monolayer occurs predominantly by the interband transition so that the optical power absorbed by graphene on the x-y plane can be expressed as $\langle P \rangle = \frac{\sigma_0}{2}\int(|E_x|^2 + |E_y|^2)dxdy,$ where σ_0 is optical conductivity of graphene [11]. The change of absorption by the graphene gratings calculated using FDTD simulation for both cases is shown in Fig 2-3-5. Similar to the tendency of the change of Q-factor, as the width of the gratings increases, the absorption rate increases rapidly when the graphene gratings are at the antinode, the absorption rate increases gradually when the graphene gratings are in the node.

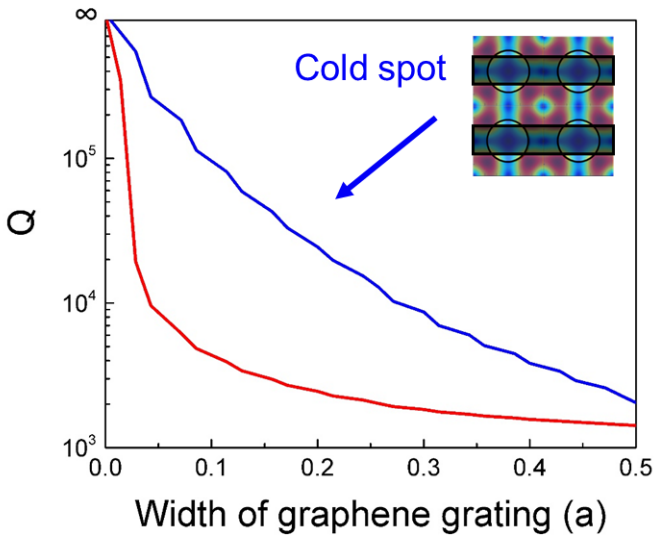

Figure 2-3-4 Q-factor calculation of PhC-graphene structures with the graphene gratings on the antinode and node of the Γ_1 band-edge mode of the square lattice PhC structure, respectively.

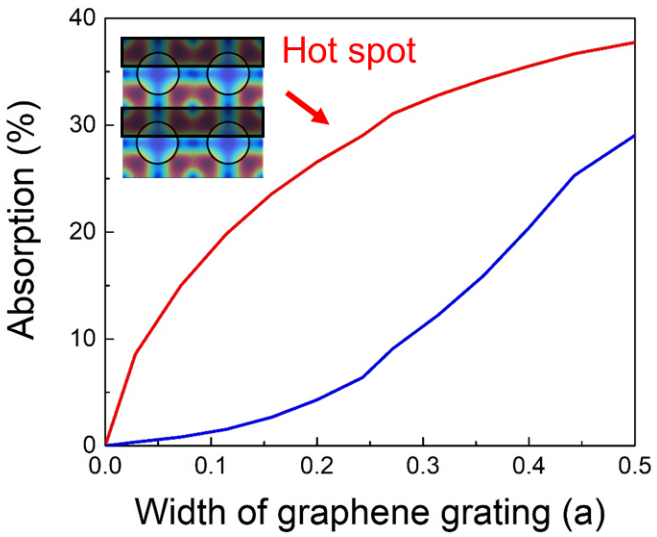

Figure 2-3-5 Optical absorption calculation of PhC-graphene structure with the graphene gratings on the antinode and node of the Γ_1 band-edge mode of the square lattice PhC structure, respectively.

2.3.3 Device fabrication

Figure 2-3-6 and 2-3-7 show the SEM images of the fabricated PhC band-edge lasers with grating patterns of graphene. Figure 2-3-6 is a SEM image of a sample fabricated on a square lattice PhC structure with a graphene grating arranged in the node part of the resonant mode. On the contrary, Fig. 2-3-7 shows a sample fabricated such that a graphene grating on the square lattice PhC structure is arranged in the antinode part of the resonant mode.

Device fabrication began with the deposition of a 50-nm-thick Si_3N_4 hardmask layer on a semiconductor epistructure, composed of a 230-nm-thick InGaAsP MQW layer and a 1000-nm-thick InP sacrificial layer, using PECVD method. An array of square lattice PhC band-edge patterns was generated by electron-beam lithography. The period of square lattice structure was a = 600 nm while the air-hole radius was 0.3a. The size of each PhC pattern was ~ 20×20 μm^2. The PhC patterns were transferred down to the Si_3N_4 and MQW layers sequentially by RIE using the gas mixtures of O_2/CF_4 and CH_4/H_2, respectively. Then, wet-etching was performed at 4°C using HCl aqueous solution (3:1) to selectively remove the InP sacrificial layer, which resulted in a completed PhC band-edge laser sample in a free-standing membrane form.

A multi-layer graphene sheet, which was grown on a Ni-deposited on Si substrate by TCVD method. Then, a grating pattern of photoresist was formed on the graphene sheet by laser interference lithography (LIL) method [16]. The LIL method is an efficient lithography technique that can produce periodic 1D or 2D patterns on a large area at low cost and high throughput using a laser interference patterns [17]. Grating pattern was fabricated with a fixed width of 200 nm due to the limitation of the laser interference lithography method. The graphene was etched using O_2 plasma to transfer the grating pattern to the graphene. The etching conditions using O_2 plasma are as follows. The etching time was 30 seconds, the RF power was 50 W, the flow rate of O_2 gas was 50 sccm, and the pressure of the chamber was 50 mTorr. The

photoresist was removed with acetone to complete the graphene grating pattern.

Next, after a PMMA layer was spin-coated directly on the graphene grating pattern as a temporal handling layer, we removed the Ni layer in a $FeCl_3$ solution to obtain in a free-standing PMMA/graphene-grating film floating on water. The PMMA/graphene-grating film was then transferred and aligned by hand onto the PhC band-edge laser sample. Then, the PMMA layer was removed with acetone.

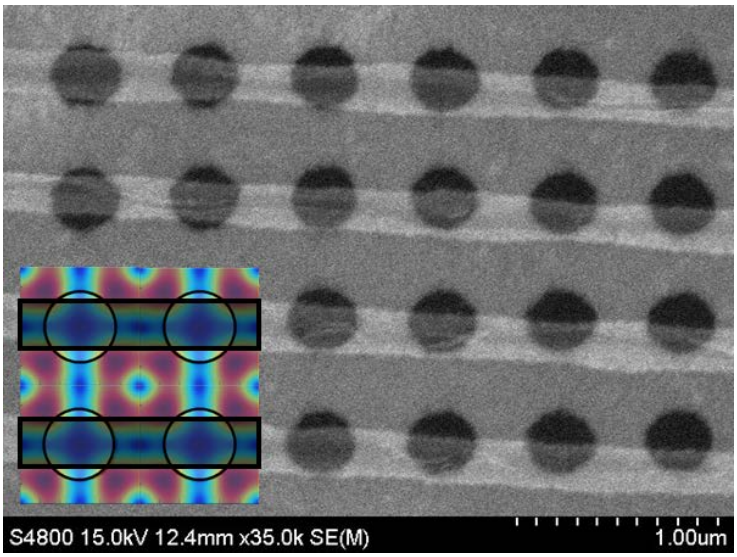

Figure 2-3-6 SEM image of the device with the graphene gratings on the node of the Γ_1 band-edge mode of the square lattice PhC structure. Inset refers the position of graphene gratings on the resonance mode.

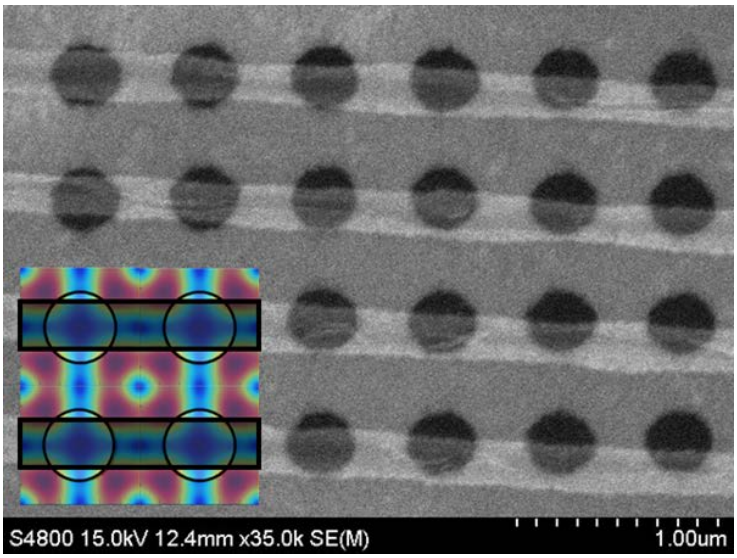

Figure 2-3-7 SEM image of the device with the graphene gratings on the node of the Γ_1 band-edge mode of the square lattice PhC structure. Inset refers the position of graphene gratings on the resonance mode.

2.3.4 Laser interference lithography

Laser interference lithography (LIL) is a lithography technique useful for making periodic sub-micron scale patterns on large area substrates. LIL is basically a method that uses interference phenomenon of coherent multiple laser beams. The intensity distribution of the interference pattern for two coherent laser beams is expressed as the sum of the electric field.

$$I_{12} = \left|\overrightarrow{E_1}(\vec{r}) + \overrightarrow{E_2}(\vec{r})\right|^2 = I_1 + I_2 + 2\sqrt{I_1 I_2}\cos\left[\frac{2\pi}{\lambda}(\sin\theta_1 + \sin\theta_2)x\right].$$

The schematic of the LIL system based on a Lloyd's mirror interferometer is shown in the Fig. 2-3-8. In out LIL system, 405-nm diode laser is used as the light source. The spatial filter, which consists of an objective lens and a pinhole. The expanded laser beam is incident on Lloyd's mirror interferometer and the interference pattern of incident light and reflected light is transferred to the sample surface. The period of the interference pattern is determined by the incident angle, which can be easily controlled by the rotation of the interferometer. The period of the interference pattern is as follows.

$$\Lambda = \frac{\lambda}{2(\sin\theta_1 + \sin\theta_2)},$$

where the λ is the wavelength of diode laser (In our system, λ = 405 nm). In general, the angle of incident beam and the angle of reflected beam is same $(\theta_1 = \theta_2)$ for the flat mirror.

Figure 2-3-9 is the SEM images of 1D and 2D photoresist patterns by the LIL method. The 1D grating pattern is formed by a single exposure of the interference pattern of two laser beams. The 2D square-lattice pattern is generated by an additional exposure after the first exposure and sample rotation. The width or size of grating patterns is determined by the exposure time. Using the LIL method, we can make not only the periodic grating patterns, but also PhC structures at a large area with high throughputs.

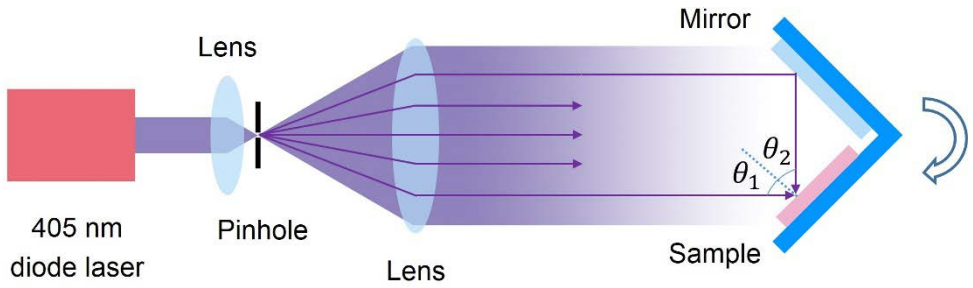

Figure 2-3-8 Schematic of the LIL setup based on a Lloyd's mirror interferometer.

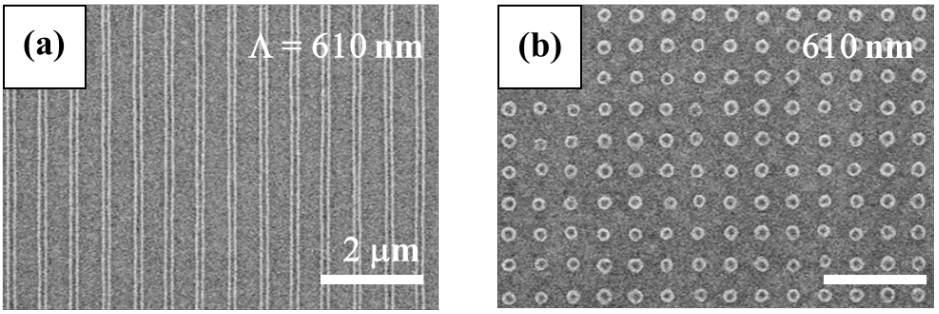

Figure 2-3-9 SEM images of fabricated (a) 1D and (b) 2D gratings using the LIL method.

2.3.5 Measurement of PL spectra

The graphene-grating film was transferred and aligned by hand onto the PhC patterns. Therefore, when the graphene grating pattern is transferred to the PhC band-edge laser structure, some misaligned areas can be seen in Fig. 2-3-6 and 2-3-7. However, the difference between the configurations of the two samples was clearly revealed, and the PL measurement of the two samples obtained meaningful results.

Figure 2-3-10 is the result of a PL measurement of the PhC band-edge laser sample where the graphene grating patterns are located on the node of the resonance mode. Although it showed about one-third of PL intensity compared to the PL intensity of the PhC band-edge laser sample without graphene, we were able to observe clear laser peaks. The result of the PL measurement of the PhC band-edge laser sample where the graphene grating patterns are located at the antinode of the resonance mode is shown in Fig. 2-3-11. When the graphene grating was located on the antinode of the resonant mode, no laser signal could be observed as shown in Fig. 2-3-11. This is because the interaction between graphene and the antinode of the resonance mode is strong, so the resonance mode is suppressed [18]. As shown in Fig. 2-3-4 and 2-3-5, the large difference between the PhC band-edge laser sample where the graphene gratings are located on the antinode and the PhC band-edge laser sample where the graphene gratings are located on the node can be experimentally confirmed by the exhibition or suppression of the laser oscillation.

On the other hand, the comparison of the PL measurements between the sample with graphene gratings on the node of the resonance mode and the sample without graphene sheet are shown in Fig. 2-3-12. Although the graphene gratings are located on the node of the resonance mode, but the intensity and slope efficiency are lower than that of the without-graphene sample, indicating that there is absorption by graphene. However, the threshold density does not show a large difference between the two samples, which shows experimentally that the absorption rate of the graphene located on the node of the resonance mode is not large as shown in Fig 2-3-5.

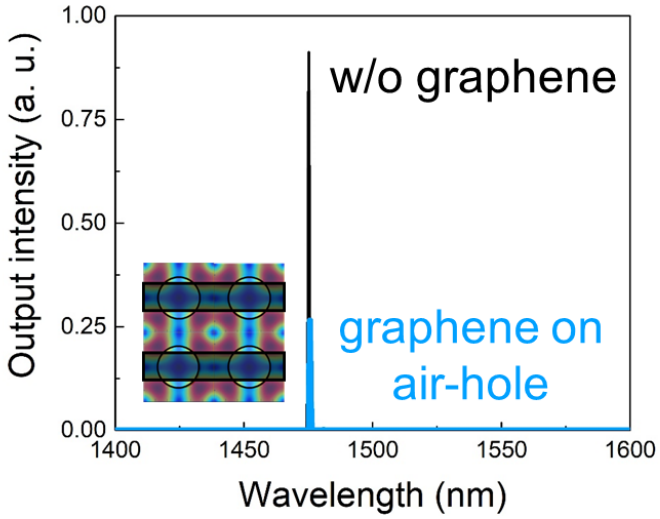

Figure 2-3-10 Measured PL spectrum of the device with the graphene gratings on the node of the Γ_1 band-edge mode of the square lattice PhC structure. Inset refers the position of graphene gratings on the resonance mode.

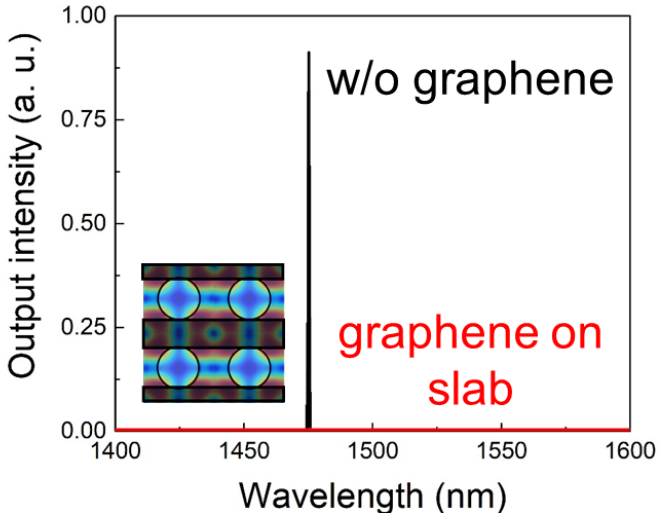

Figure 2-3-11 Measured PL spectrum of the device with the graphene gratings on the node of the Γ_1 band-edge mode of the square lattice PhC structure. Inset refers the position of graphene gratings on the resonance mode.

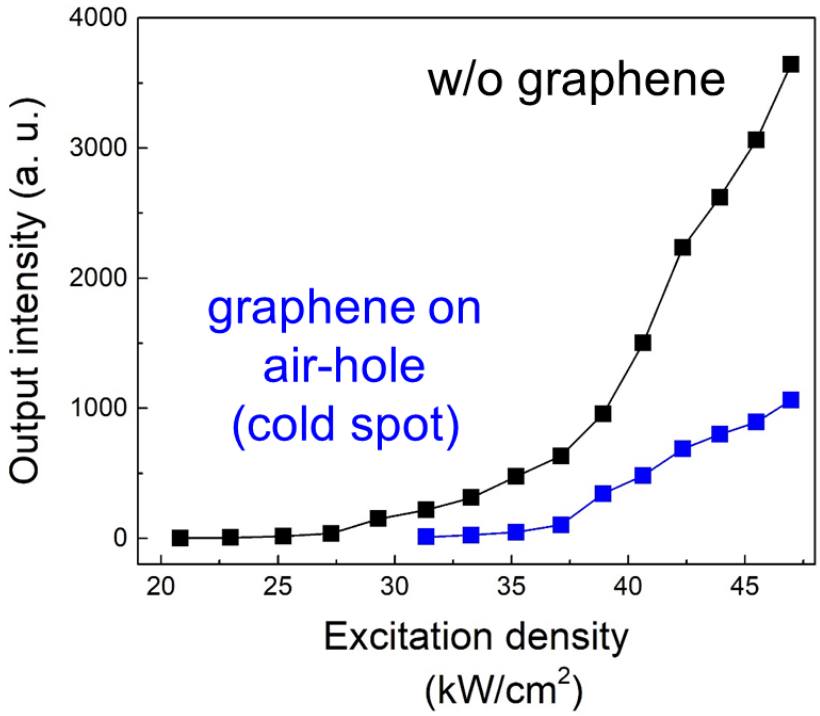

Figure 2-3-12 Measured output intensity of the devices with the graphene gratings on the node of the Γ_1 band-edge mode of the square lattice PhC structure.

2.4 Effect of PhC band-edge laser on Au particles

2.4.1 Introduction

In Sections 2.2 and 2.3 above, the characteristics of PhC lasers were examined when PhC laser structures had the graphene patterns as the light absorber. As a result, the interaction between graphene and PhC resonance mode could be observed experimentally. However, graphene is still limited in its feasibility, despite its vast possibilities and outstanding properties. As the general light absorber, metals can be considered. The transmittance of light perpendicular to the monolayer graphene is ~97.7%, but the transmittance is very low with a 50-nm-thick Au film, which is the thickness corresponding to the skin depth of Au at a wavelength of 1.5 μm. Therefore, we investigated whether the change of PhC resonance mode can be observed even in Au patterns which are more general light absorber.

The PhC band-edge laser structures contain the honeycomb lattice PhC patterns. Figure 2.4.1 is the calculated band structure for the honeycomb lattice PhC structure. Since the honeycomb lattice PhC structure has no air-hole at the center of the unit-cell, it is easy to observe the characteristics of the resonant mode by forming the metal patterns at the center. The structural parameters were chosen such that the first (Γ_1) or second (Γ_2) zone center PBE mode matches with the emission band of the InGaAsP MQW, the electric field profile for each mode is shown in Fig. 2.4.2 and 2.4.3. The two modes form the antinode and node of the resonance mode in the center of the unit-cell, respectively, so that it is easy to compare the effect of the absorber.

In this experiment, it is aimed to experimentally confirm the characteristics of the standing-wave-formed resonance mode of the PhC band-edge laser by comparing the characteristics of PhC band-edge lasers when various sizes of Au patterns are located at the antinodes and at the nodes.

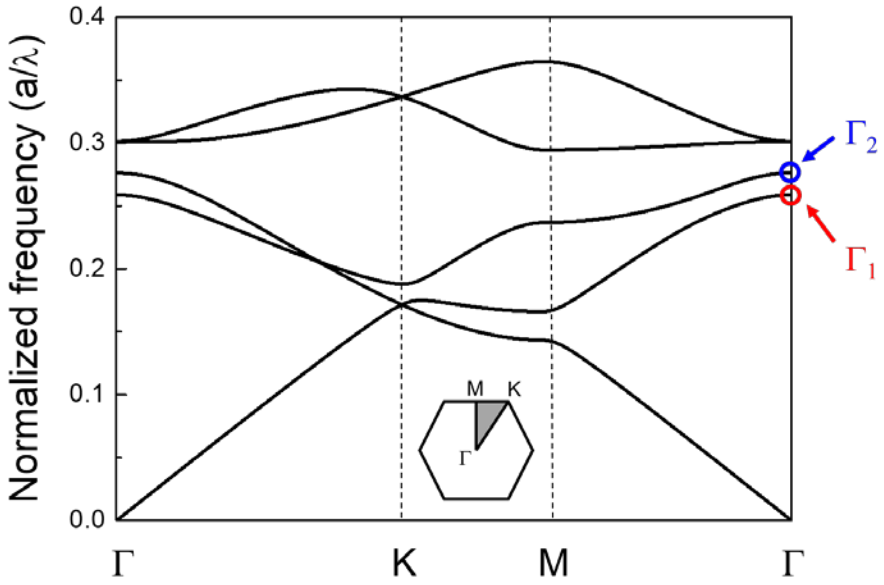

Figure 2-4-1 Band structure calculated for the honeycomb lattice PhC structure.

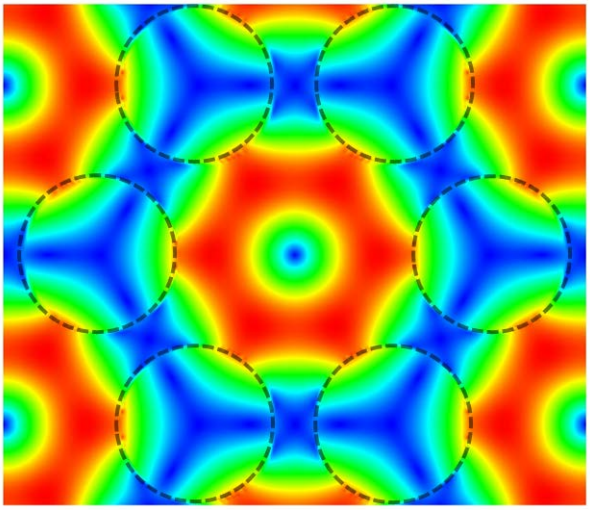

Figure 2-4-2 Transverse electric field profile of the Γ_1 band-edge mode.

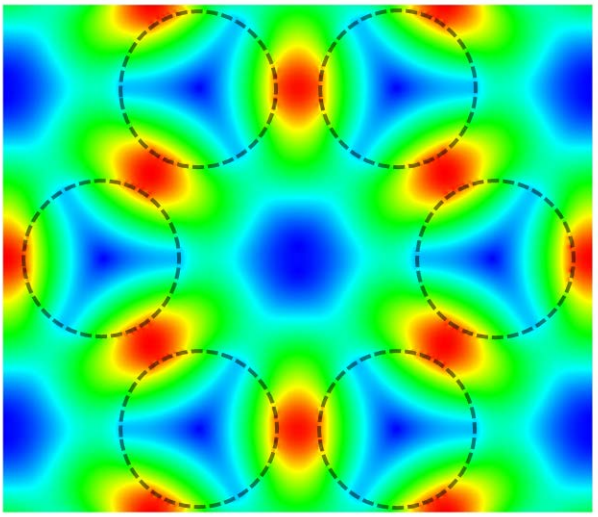

Figure 2-4-3 Transverse electric field profile of the Γ_2 band-edge mode.

2.4.2 Calculation of Q-factors

In the case of arranging the Au patterns on the antinodes and nodes of the resonant mode, the change of the resonant mode was calculated using the FDTD method.

Q-factor and decay rate are inversely related to each other. Therefore, the decrease in Q-factor should be larger when the absorption is large. The changes in Q-factor calculated by FDTD simulations with radius of Au patterns for both cases are shown in Fig 2-4-4. As expected, as the radius of the Au patterns increases, the Q-factor decreases rapidly when the Au patterns are located at the antinode. On the other hand, when the Au patterns are located at the node, there is no significant change in the Q-factor up to a radius of $r = 0.2a$, but then gradually decreased.

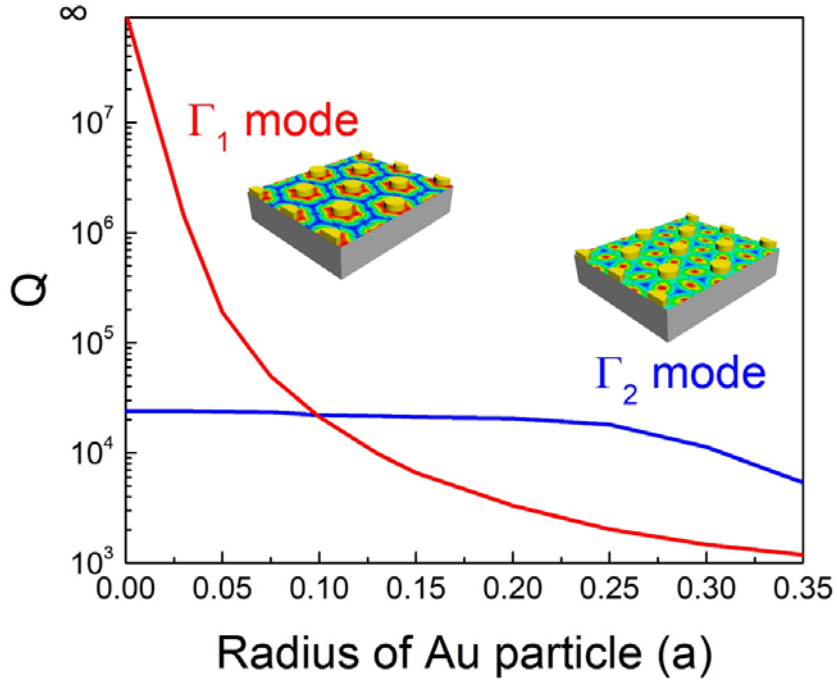

Figure 2-4-4 FDTD-simulated Q-factors of the Γ_1 and Γ_2 band-edge modes as the function of the radius of Au particle.

2.4.3 Device fabrication

Figure 2-4-5 shows the SEM images of the fabricated PhC band-edge laser structures with various sizes of Au patterns. A sample without Au pattern was set as a reference sample, and samples with seven sizes of Au patterns were fabricated.

Device fabrication began with the deposition of a 50-nm-thick Si_3N_4 hardmask layer on a semiconductor epi-structure, composed of a 230-nm-thick InGaAsP multi-quantum well layer and a 1000-nm-thick InP sacrificial layer, using PECVD method. An array of honeycomb lattice PhC band-edge patterns was generated by electron-beam lithography. The distances between two nearest air-holes is a_1 = 440 nm for Γ_1 photonic band edge-mode and a_2 = 480 nm for Γ_2 photonic band edge-mode, while the air-hole radius was 0.35a for both modes. The size of each PhC pattern was ~ 20×20 μm^2. The PhC patterns were transferred down to the Si_3N_4 and MQW layers sequentially by RIE using the gas mixtures of O_2/CF_4 and CH_4/H_2, respectively. After fabricating the PhC structure, an array of patterns for the Au particles was formed on the PhC structure by electron-beam lithography. The radii of the patterns were between r = 0.075a and r = 0.35a. As shown in insets of Fig. 2-4-5, the metal patterns between air-holes is well formed without large errors. Then, in order to form the metal patterns, titanium as an adhesive layer and gold were deposited at 10 nm and 50 nm, respectively, by electron-gun evaporator. Finally, the metal patterns are completed by removing the E-beam resist through the lift-off process. After lift-off, RTA was performed at 300°C for 30 seconds to enhance the adhesion of the metal patterns. Then, wet-etching was performed at 4°C using HCl aqueous solution (3:1) to selectively remove the InP sacrificial layer, which resulted in a completed PhC band-edge laser sample in a free-standing membrane form.

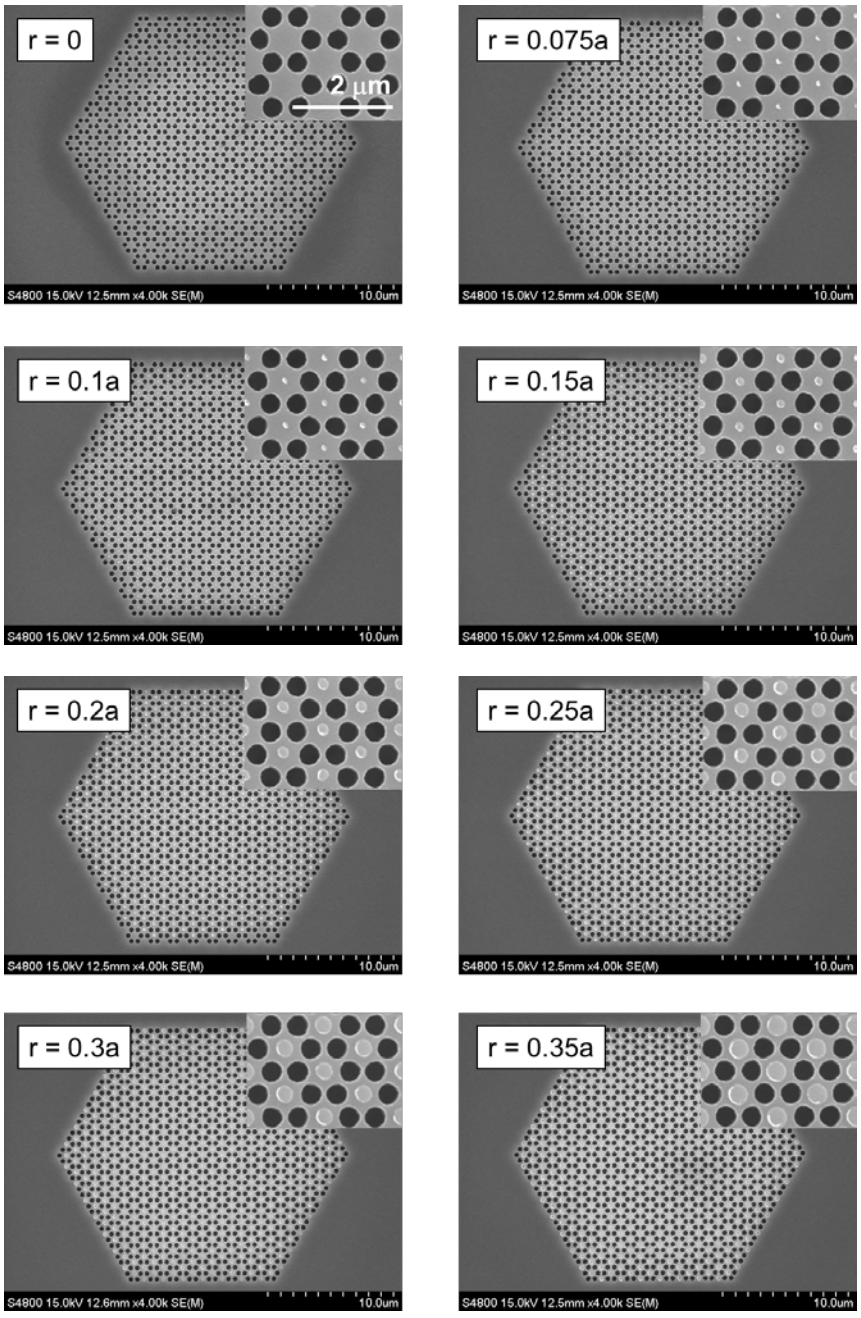

Figure 2-4-5 SEM images of the PhC band-edge laser structure with different radii of Au particles (r = 0 - 0.35a).

2.4.4 Measurement of PL spectra

Figure 2-4-6 and Figure 2-4-7 are the results of PL measurement of samples with excitation density of 0.670 kW/cm^2 where the Au patterns are located at the antinode and node in resonance mode, respectively. Similar to the sample with the graphene grating patterns, when the Au particle is located on the antinode, the interaction is strong. As the radius of the patterns increases, the PL intensity sharply decreases and the laser oscillates up to the radius of $r = 0.15a$. However, when the Au particle is located on the node, there was no significant change in the PL intensity until the radius of the patterns is $r = 0.2a$. After that, the PL intensity is greatly reduced, but the laser oscillation is successful except for the final sample of $r = 0.35a$.

Figure 2-4-6 and Figure 2-4-7 show peak intensities easily to show tendency of change of intensity. When the Au particle is on the antinode, the peak intensities tend to decrease sharply as shown in Fig. 2.4.6. However, when Au particles are present on the node, the peak intensities decrease gradually until the radius reaches $r = 0.2a$, then decrease rapidly thereafter as shown in Fig. 2.4.7. The trend tendency of the peak intensities is consistent with the change tendency obtained from the above Q-factor calculation. That is, the influence of theoretically calculated Au particles on the resonance mode was experimentally well observed.

Figure 2-4-8 and 2-4-9 are the observation of the threshold density to clearly observe the effect of the absorber. Similarly, when the Au particle is located on the antinode of the resonant mode, the threshold density increases sharply with increasing radius, but when it is located on the node, the threshold density gradually increases until $r = 0.2a$, and then the sharp increase is observed again.

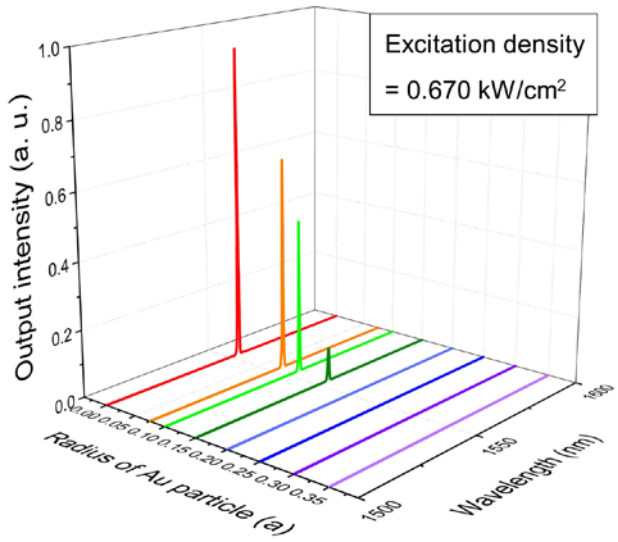

Figure 2-4-6 Measured PL spectra of the Γ_1-point PhC band-edge laser with different radii of Au particles.

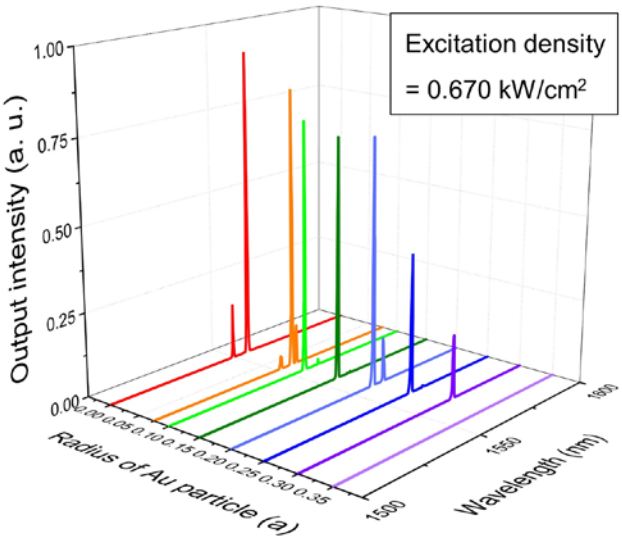

Figure 2-4-7 Measured PL spectra of the Γ_2-point PhC band-edge laser with different radii of Au particles.

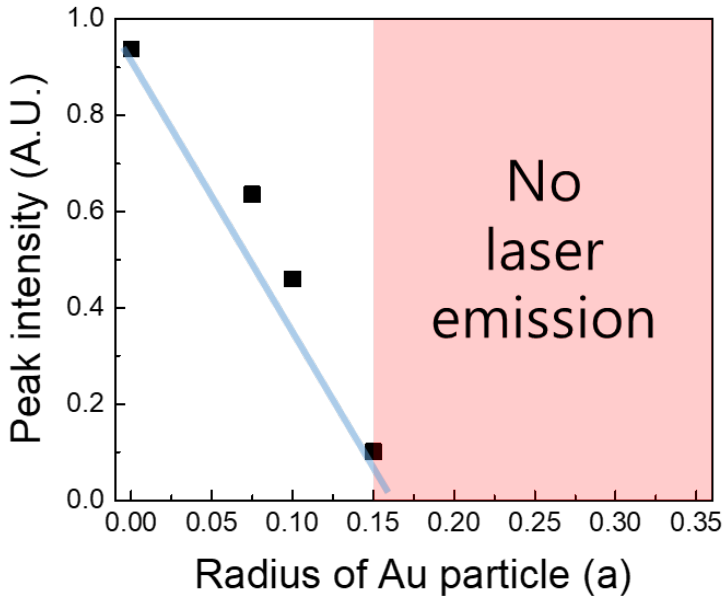

Figure 2-4-8 Measured peak intensity of the Γ_1-point PhC band-edge laser with different radii of Au particles.

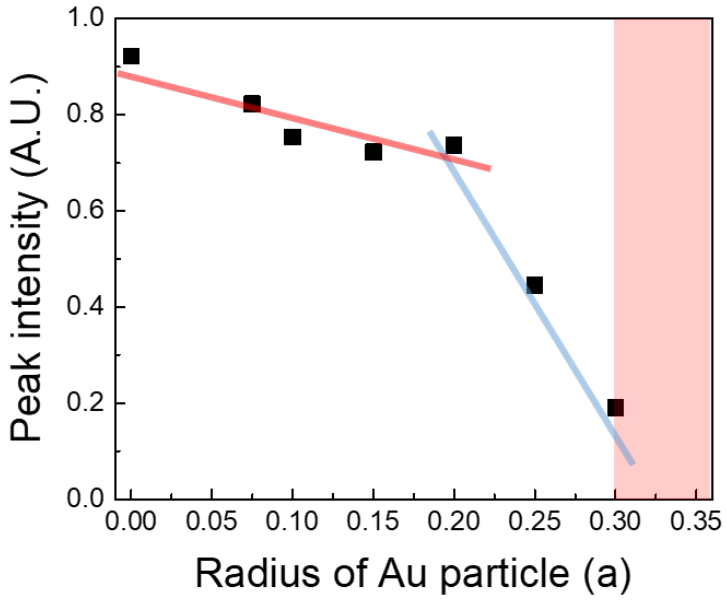

Figure 2-4-9 Measured peak intensity of the Γ_2-point PhC band-edge laser with different radii of Au particles.

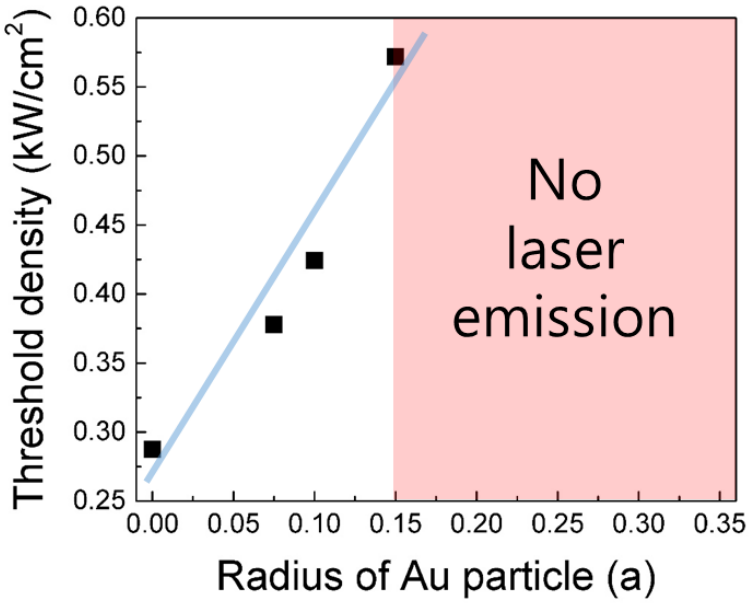

Figure 2-4-10 Measured threshold density of the Γ_1-point PhC band-edge laser with different radii of Au particles.

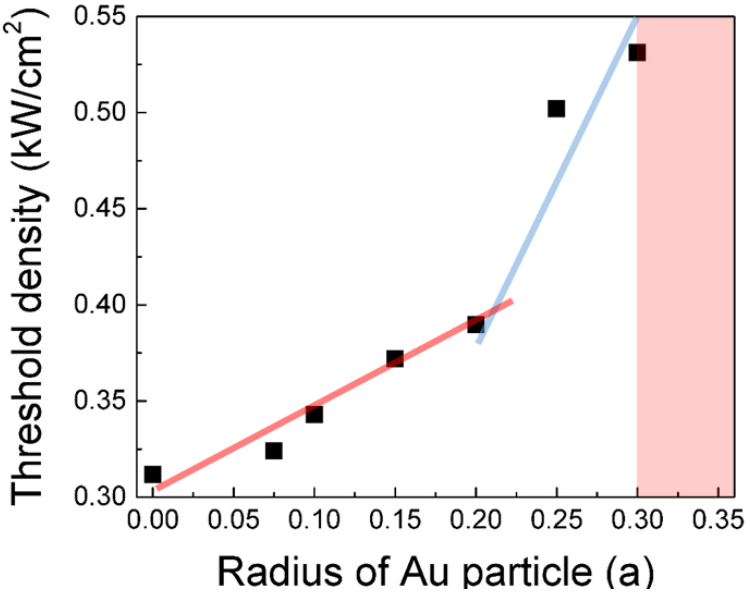

Figure 2-4-11 Measured threshold density of the Γ_2-point PhC band-edge laser with different radii of Au particles.

2.5. Design of electrodes of electrically injected PhC laser

2.5.1 Contact design for electrically injected PhC laser

In chapter 2, when the absorber is present on the PhC structure, the change in resonance mode is theoretically calculated and experimentally observed. The effect of the PhC on the resonance mode is also meaningful enough. However, the structure of the absorber, which does not greatly increase the interaction between PhC resonance modes and the absorber, can be applied to the contact design of the electrically driven PhC laser. Figure 2-5-1 and 2-5-2 are representative electrically driven PhC laser studies, electrically driven single-cell PhC laser [19] and electrically driven nanobeam laser [20]. The common feature of both studies is that the electrode structure is designed so that holes are injected directly into the PhC pattern, but the cavity mode is not disturbed by the electrode structure. Likewise, we believe that applying this study will allow us to design an electrode structure that directly contacts the PhC pattern, but causes minimal interaction with the resonant mode.

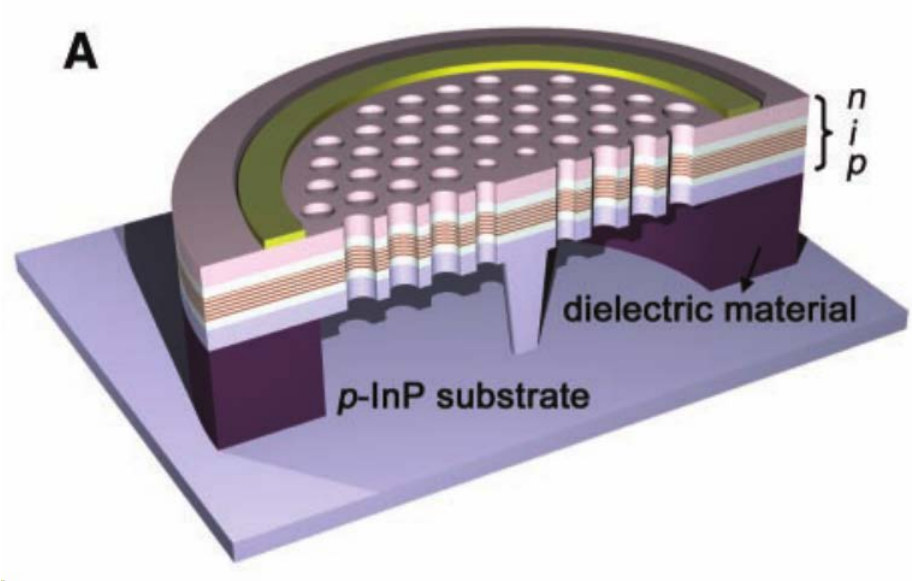

Figure 2-5-1 Electrically driven single-cell PhC laser [19].

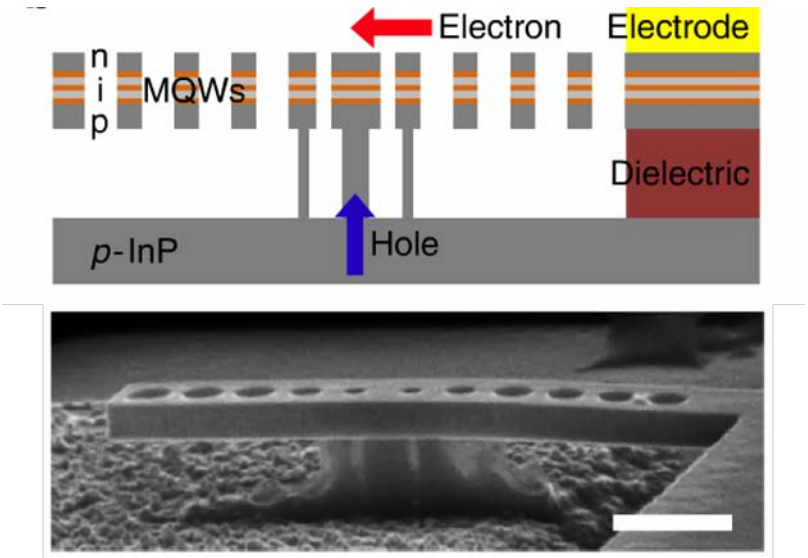

Figure 2-5-2 Electrically driven nanobeam laser [20].

2.5.2 Graphene-contact IR-LED structure

A simple IR-LED was fabricated to investigate the electrical characteristics of a semiconductor light-emitting diode device to see if a device could be fabricated with graphene as the p-contact. Figure 2-5-3 shows the epi structure of p-i-n InGaAsP MQW wafer used for IR-LED device. This wafer contains three pairs of InGaAsP MQW layers and strongly p-doped and n-doped layers.

The simple layout of the IR-LED structure is shown in Fig. 2-5-4. Device fabrication began with the deposition of a 50-nm-thick Si_3N_4 hardmask layer on a semiconductor epi structure using PECVD method. The Si_3N_4 layer also serves as a hardmask and current blocking layer. An opening pattern for light emitting region was generated by electron-beam lithography, and the pattern were transferred down to Si_3N_4 layer by reactive-ion etch using the gas mixtures of O_2/CF_4. Then device isolation pattern was formed by E-beam lithography and Si_3N_4 and MQW layers were etched through RIE etch using the gas mixtures of O_2/CF_4 and CH_4/H_2, respectively. After, the graphene layer was transferred to the device as a p-contact layer, the graphene isolation pattern was formed by E-beam lithography, and the graphene was etched using O_2 plasma. Finally, Ag disk as the p-contact pad was formed by ink-jet printing method [21]. Microscope image of the fabricated graphene-contact IR-LED is shown in Fig. 2-5-5.

Figure 2-5-6 and 2-5-7 show the electrical characteristics of the fabricated IR-LED device. The I-V curve showed clear diode characteristics as shown in Fig. 2-5-6, with a turn-on voltage of about 1.2 V and an electrical resistance of 2.75 kΩ. It was confirmed that graphene as the p-contact was well formed due to a similar tendency to the electrical characteristics shown in the literature [22]. On the other hand, the measured EL result is in Fig. 2-5-7. As the current increases, the tendency of increasing the EL intensity is appeared. Thus, it is experimentally confirmed that graphene can be used as a transparent electrode in a light-emitting-diode structure.

		layer	Thickness(Å)
p-ohmic		p++InGaAs	1000
cap		p-InP	500
clad		p-1.24Q InGaAsP 640C	600
QWs		i-1.24Q InGaAsP 640C	235
	x3	i-InGaAs	70
		1.24Q InGaAsP 640C	210
		i-1.24Q InGaAsP 640C	25
clad		n-1.24Q InGaAsP	600
sacrificial		n-InP	10000
etch stop		n-InGaAs	500
buffer		n-InP	2000
wafer	n-InP 2-inch		

Figure 2-5-3 Epi structure of p-i-n InGaAsP MQW wafer.

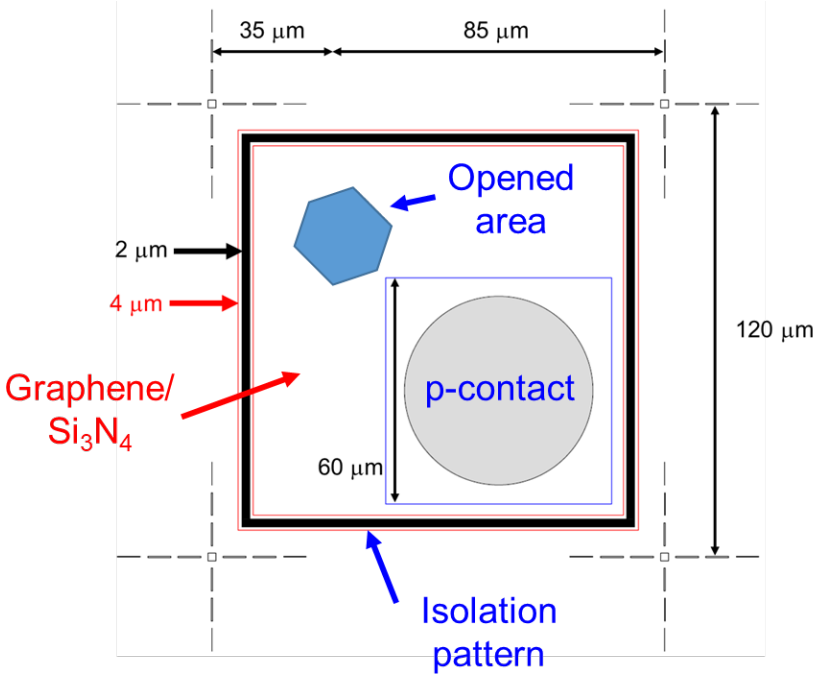

Figure 2-5-4 Device layout of the graphene-contact IR-LED.

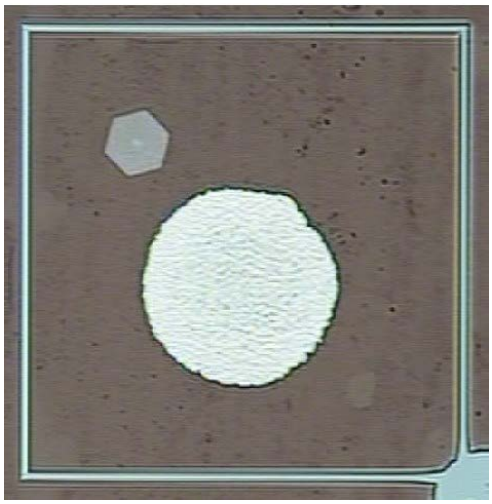

Figure 2-5-5 Microscope image of the fabricated graphene-contact IR-LED.

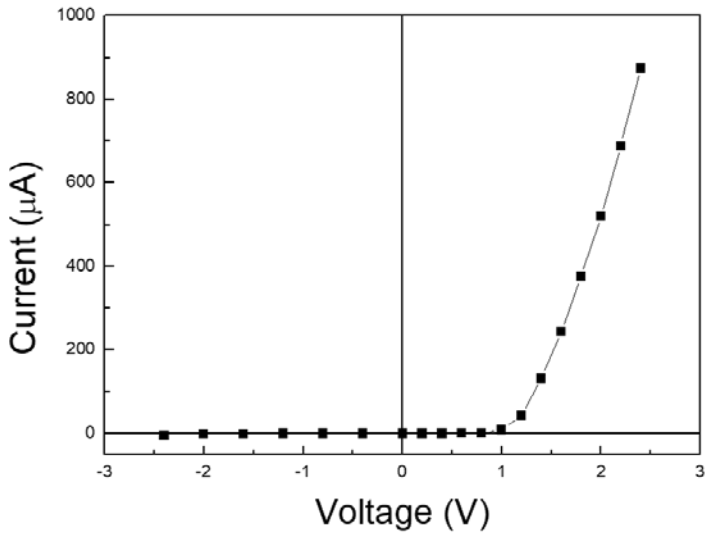

Figure 2-5-6 I-V curve of the graphene-contact IR-LED.

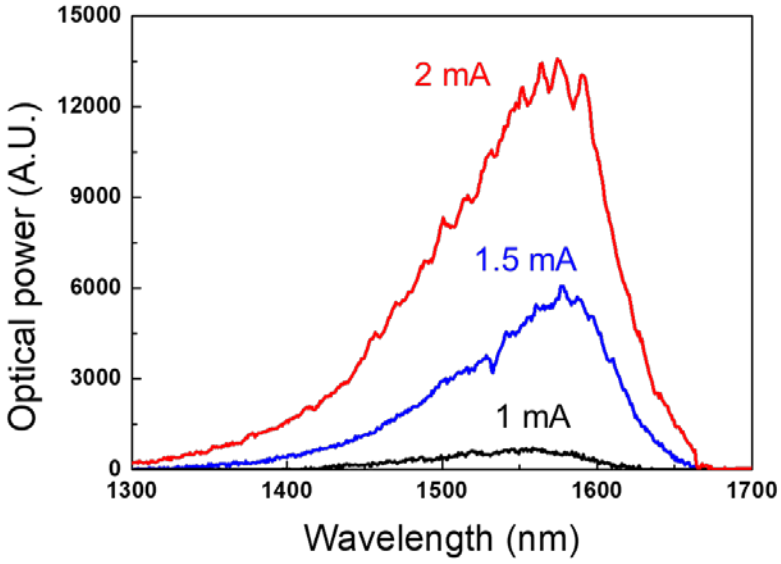

Figure 2-5-7 Measured EL spectra of the graphene-contact IR-LED.

2.6 Summary

In conclusion, we successfully observed the characteristics of PhC lasers when there is an optical absorber in the PhC laser structure, and observed the changes in the characteristics of the PhC lasers when the optical absorber changes. Three experiments were carried out to investigate the change of the PhC resonance mode by the optical absorber.

First, we integrated the graphene with window pattern on the PhC L3 cavity laser structure and investigated the PL intensity variation of the PhC laser according to the window size. As the area of the window pattern increases, the interaction with the cavity mode decreases and the PL intensity increases. Also, the graphene with window pattern can be used to perform a single mode operation of the PhC cavity laser.

Second, we observed the characteristics of PhC band-edge lasers by arranging the grating patterns of the graphene on the antinodes and nodes of the resonant mode of the square lattice PhC band-edge lasers. When the graphene grating is arranged on the antinode, the laser operation is suppressed due to the strong interaction with the band-edge mode. However, when the graphene grating is arranged on the node, the laser operation is observed because the interaction of the graphene with the band-edge mode is not large.

Third, in the honeycomb lattice PhC band-edge laser structure, the characteristics of the PhC band-edge laser according to the optical absorber were observed using gold particles as an optical absorber. When the gold particle is arranged on the antinode of the band-edge mode, the PL intensity of the PhC laser is rapidly attenuated as the particle size increases. However, when the gold particle is arranged on the node of the band-edge mode, the PL intensity of the PhC laser tends to be retained even if the particle size increases.

Although it is meaningful to investigate the effect of the optical absorber on the resonance mode of the PhC, we think that this research can be applied for the contact design of the electrically driven PhC laser.

References

[1] R. R. Nair, P. Blake, A. N. Grigorenko, K. S. Novoselov, T. J. Booth, T. Stauber, N. M. R. Peres, and A. K. Geim, "Fine Structure Constant Defines Visual Transparency of Graphene," Science **320**, 1308 (2008).

[2] S. J. Koester, and M. Li, “Waveguide-Coupled Graphene Optoelectronics,” IEEE Journal of selected topics in quantum electronics **20**, 84-94 (2014)

[3] M. Liu, X. Yin, E. Ulin-Avila, B. Geng, T. Zentgraf, L. Ju, F. Wang, and X. Zhang, "A graphene-based broadband optical modulator," Nature **474**, 64-67 (2011).

[4] S. J. Koester, and M. Li, “High-speed waveguide-coupled graphene-on-graphene optical modulators,” Appled Physics Letters **100**, 171107 (2012)

[5] F. Xia, T. Mueller, Y. Lin, A. Valdes-Garcia, and P. Avouris, "Ultrafast graphene photodetector," Nature Nanotechnology **4**, 839-843 (2009).

[6] X. Gan, R. Shiue, Y. Gao, I. Meric, T. F. Heinz, K. Shepard, J. Hone, S. Assefa, and D. Englund, “Chip-integrated ultrafast graphene photodetector with high responsivity,” Nature Photonics **7**, 883-887 (2013)

[7] X. Gan, K. Mak, Y. Gao, Y. You, F. Hatami, J. Hone, T. Heinz, D. Englund, "Strong Enhancement of Light–Matter Interaction in Graphene Coupled to a Photonic Crystal Nanocavity," Nano Letter **12**, 5626-5631 (2012).

[8] K. Kim, M. Hwang, H. Kim, J. Choi, Y. No, and H. Park, “Direct observation of exceptional points in coupled photonic crystal lasers with assymmetric optical gains,” Nature Communications **7**, 13893 (2016)

[9] M. Hwang, H. Kim, K. Kim, K. Jeong, J. Park, J. Choi, J. Kang, J. Lee, W. Park, J. Song, M. Seo, and H. Park, "Switching of Photonic Crystal Lasers by Graphene," Nano Letter **17**, 1892-1898 (2017).

[10] Y. Akahane, T. Asano, B. Song, and S. Noda, “Fine-tuned high-Q photonic crystal nanocavity,” Optics Express **13**, 1202-1214 (2005)

[11] H. Li, Y. Anugrah, S. J. Koester, and M. Li, "Optical absorption in graphene integrated on silicon waveguides," Appl. Phys. Lett. **101**, 111110 (2012)

[12] Y. No, H. Ee, S. Kwon, S. Kim, M. Seo, J. Kang, Y. Lee, and H. Park, “Characteristics of dielectric-band modified single-cell photonic crystal lasers,” Optics Express **17**, 1679-1690 (2009)

[13] C. Cho, J. Jeong, J. Lee, and H. Jeon, “Photonic crystal band edge laser array with a holographically generated square-lattice pattern,” Applied Physics Letters **87**, 161102 (2005)

[14] S. Noda, M. Yokoyama, M. Imada, A. Chutinan, and M. Mochizuki, “Polarization mode control of two-dimensional photonic crystal laser by unit cell structure design,” Science **293**, 1123-1125 (2001)

[15] A. Chutinan, and S. John, “Light trapping and absorption optimization in certain thin-film photonic crystal architectures,” Physical Review A **78**, 023825 (2008)

[16] A. Kazemi, X. He, S. Alaie, J. Ghasemi, N. M. Dawson, F. Cavallo, T. G. Habteyes, S. R. J. Brueck, and S. Krishna, “Large-area semiconducting graphene nanomesh tailored by interferometric lithography,” Scientific Reports **5**, 11463 (2015)

[17] H. Kim, H. Jung, D. Lee, K. Lee, and H. Jeon, “Period-chirped gratings fabricated by laser interference lithography with a concave Lloyd’s mirror,” Applied Optics **55**, 354-359 (2016)

[18] H. Park, S. Kim, S. Kwon, G. Kim, S. Kim, H. Ryu, S. Kim, and Y. Lee, “Single-mode operation of two-dimensional photonic crystal laser with central post,” IEEE Photonics Technology Letters **15**, 1327-1329 (2003)

[19] H. Park, S. Kim, S. Kwon, Y. Ju, J. Yang, J. Baek, S. Kim, and Y. Lee, “Electrically driven single-cell photonic crystal laser,” Science **305**, 1444-1447 (2004)

[20] K. Jeong, Y. No, Y. Hwang, K. Kim, M. Seo, H. Park, and Y. Lee, “Electrically driven nanobeam laser,” Nature Communications **4**, 2822 (2013)

[21] S. Chung, M. Jang, S. Ji, H. Im, N. Seong, J. Ha, S. Kwon, Y. Kim, H. Yang, and Y. Hong, “Flexible high-performance all-inkjet-printed inverters: organo-compatible and stable interface engineering,” Advanced Materials **25**, 4773-4777 (2013)

[22] Y. Kim, S. Kwon, J. Lee, M. Hwang, J. Kang, W. Park, and H. Park, “Graphene-contact electrically driven microdisk lasers,” Nature Communications **3**, 1123 (2012)

Chapter 3

Electrical modulation of PhC band-edge laser with graphene monolayer

3.1 Introduction

Since its discovery, graphene, a two-dimensional carbon atoms network arranged in a honeycomb-lattice, has been attracting an enormous attention owing to its unique physical properties, such as the strong mechanical tensile strength [1], high charge-carrier mobility [2, 3], large thermal conductivity [4], etc. In terms of optical properties, graphene is a broadband optical absorber; a single graphene monolayer sheet can absorb as much as ~2.3% of the incident light despite the extremely short atomic-scale optical path length [5]. Using these outstanding properties, many graphene-based photonic devices have been developed, including broadband polarizers (as shown in Fig. 3-1-1) [6], optical modulators (as shown in Fig. 3-1-2) [7], and ultrafast photodetectors [8].

It is worth noting that the optical absorption by graphene can be directly controlled by tuning the Fermi-level, which can be accomplished by electrical gating [9] or chemical doping [10]. Among the two methods, electrical gating is preferred owing to its compatibility with optoelectronic devices, which provides higher application potentials. In principle, the absorption by graphene can be modulated at high speed and low power consumption owing to the high carrier mobility of graphene. However, the specific capacitances that can be obtained using conventional gate dielectrics, such as SiO_2, Al_2O_3, and HfO_2, are in the range of 10–1000 nF/cm^2 [11-13], which is too small to affect the Fermi level of graphene at low gate voltages. This challenge can be overcome by utilizing electrolyte gating, where an ion-gel film is employed as the gate dielectric. Ion-gel consists of an ionic liquid that has a large

ion conductivity and triblock copolymer that forms a cross-linked network. It exhibits a very large specific capacitance ($C \approx 10\ \mu F/cm^2$) [13-15], which provides a Fermi-level tuning at low gate voltages of a few volts, owing to the nanometer-thick electrical double layers (EDL) formed at the interface between the electrolyte and electrode [12, 16]. Furthermore, an ion-gel can be prepared at low temperatures and transferred in a solvent-free environment; hence, it can be applied to almost any substrate [13].

Graphene has been employed in PhC structures to induce extraordinary photonic properties, as reported in the pioneering studies on the enhanced optical absorption by a graphene-capped passive PhC nano-cavity [17-19]. Figure 3-1-3 shows strong enhancement of light-matter interaction in graphene coupled to a PhC nanocavity and Fig. 3-1-4 shows the electrically controllable passive PhC device of silicon PhC cavity structure with graphene. Recently, research was reported that employment of the above idea in a PhC cavity laser (as shown in Fig. 3-1-5), an active photonic device that has a wavelength-sized tiny cavity, in order to electrically modulate the laser output [20]. Although a cavity-based PhC laser consumes very low power, which makes it applicable as a single photon source, it may not be suitable for future photonic integrated circuits (PICs), owing to its low laser output power and fixed laser emission direction (only along the direction perpendicular to the 2D PhC plane, unless the quality factor Q of the cavity is intentionally deteriorated). In this context, photonic band-edge (PBE) lasers could be more desirable for PIC applications. PBE lasers are a special type of PhC lasers; they have a fully periodic structure without defects and exhibit a standing-wave modal profile. The output power of a PBE laser can be easily scaled by adjusting the active device area. In addition, the direction of the laser emission can be tailored by controlling the PBE modes. The PBE mode at the Brillouin zone center (Γ-point) corresponds to a vertical emission, while the PBE mode at the zone boundary corresponds to an in-plane emission. In this study, we demonstrate a direct modulation of the laser output by electrical tuning of the Fermi-level of a graphene monolayer sheet attached to a PBE laser device. The electrical

modulation is facilitated at a low gate voltage operation by the electrolyte gating, where the graphene sheet is covered by an ion-gel film. We observe that the high output power from an optically excited PBE laser can be enhanced or reduced (partially or completely) by applying a DC gate voltage smaller than 1 V.

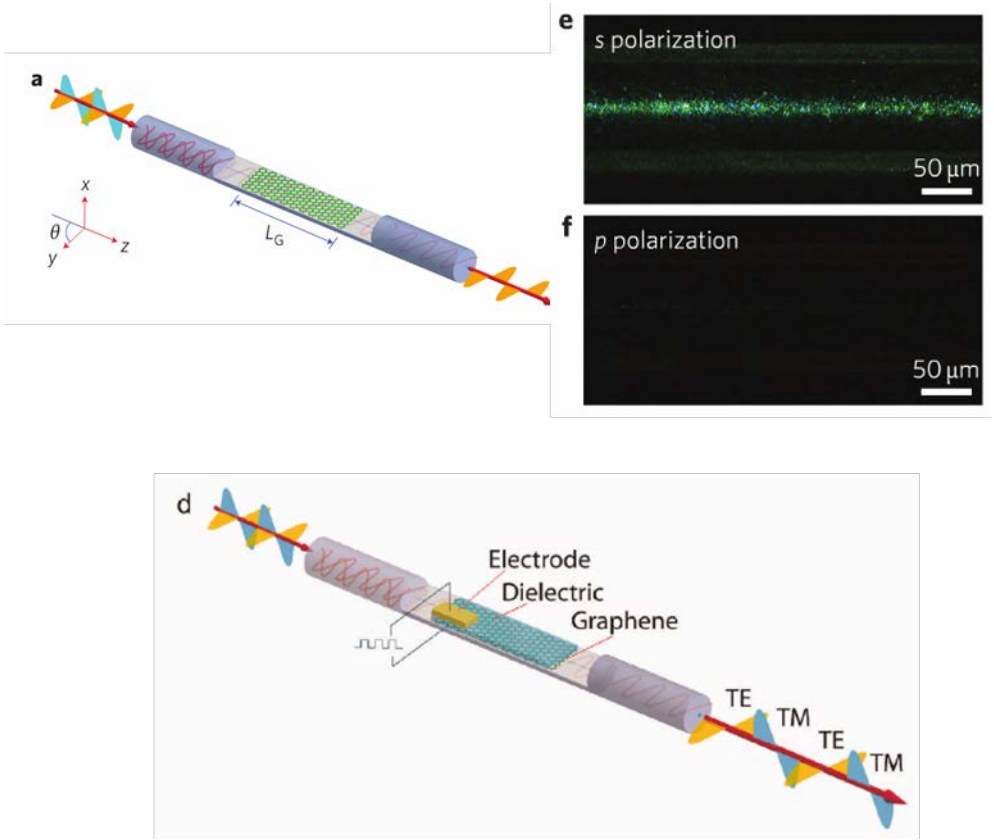

Figure 3-1-1 Broadband graphene polarizer [6].

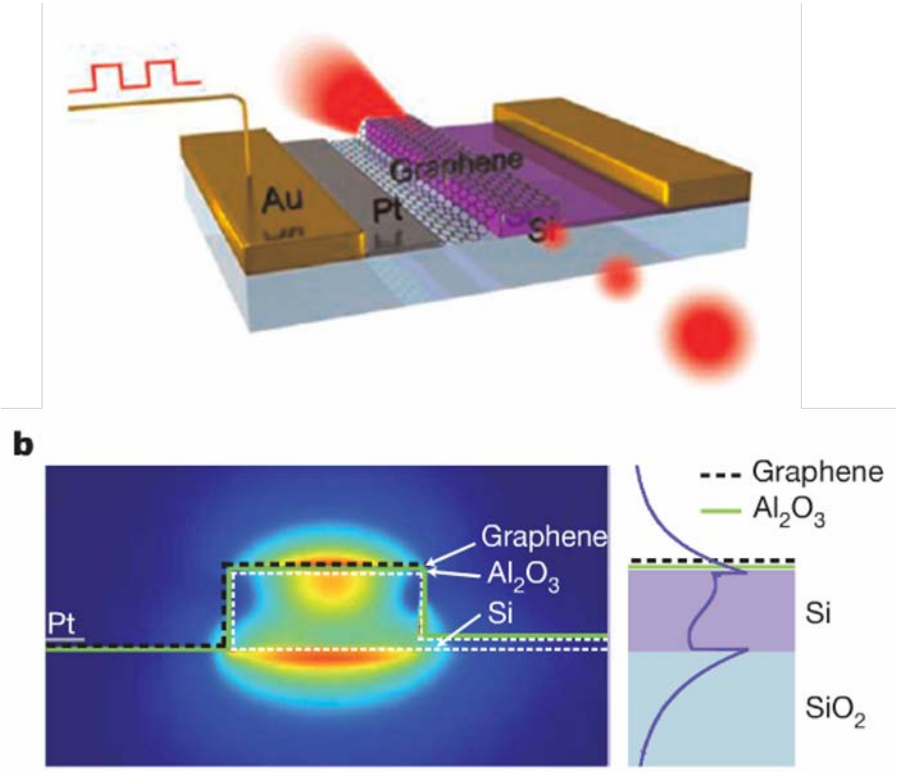

Figure 3-1-2 A graphene-based broadband optical modulator [7].

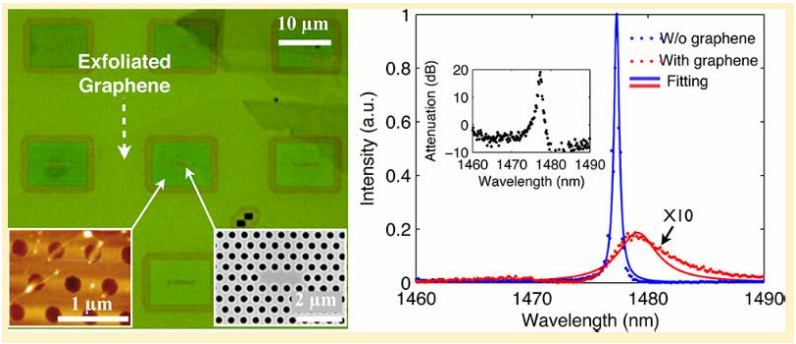

Figure 3-1-3 Strong enhancement of light-matter interaction in graphene coupled to a PhC nanocavity [17].

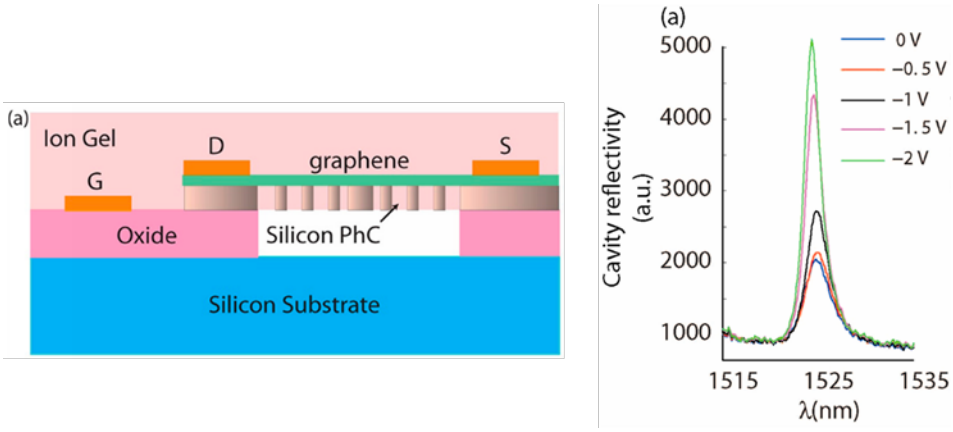

Figure 3-1-4 Electrical control of silicon PhC cavity by graphene [18].

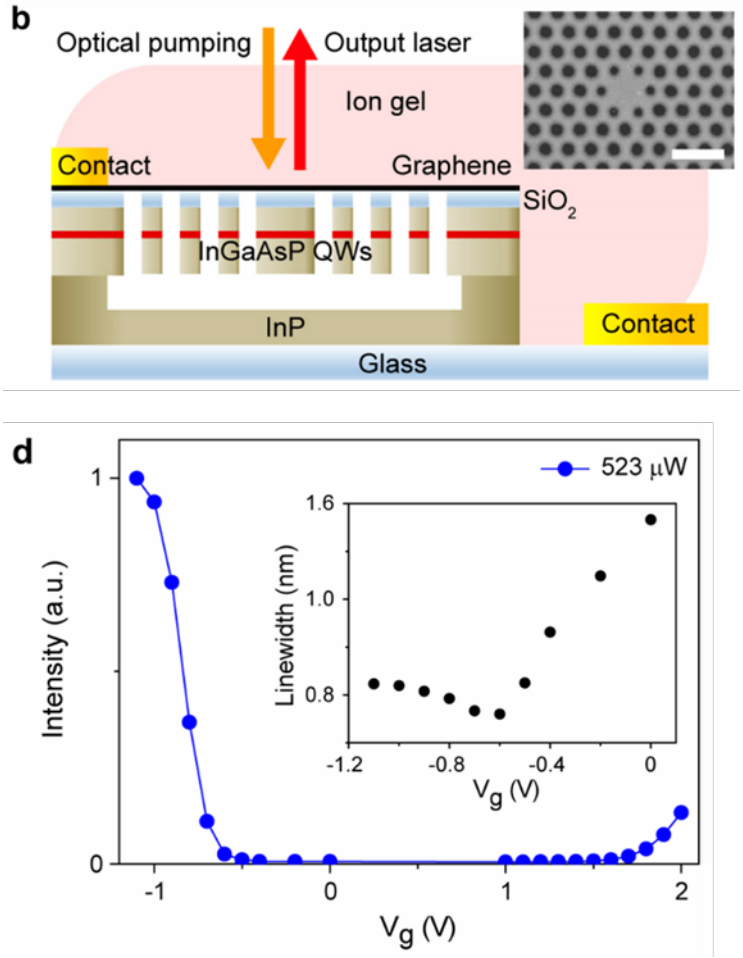

Figure 3-1-5 Switching of PhC lasers by graphene [20].

3.2 Tuning of optical absorption of graphene monolayer

3.2.1 Electric field effect in monolayer graphene

Since the isolation of graphene in 2004 by Andre Geim and Konstantin Novoselov at the University of Manchester, people were interested in graphene transistors. So, it is early known that graphene changes carrier densities due to external electric fields, and hence electrical conductivity [9] as shown in Fig. 3-2-1.

Similarly, studies have been conducted to observe the change of the absorption rate by graphene when there is an external electric field in the graphene [7]. When holes are injected into the valence band of the graphene or electrons are injected into the conduction band by an external electric field, the absorption rate of graphene is decreased. The Figure 3-2-2- shows the change in absorption rate of waveguide mode due to graphene according to the gate voltage at waveguide-graphene structure. The inhibition of the band transition by adjusting the graphene Fermi level is called Pauli blocking.

Applying the Pauli blocking principle, not only the absorption of the waveguide mode but also the interaction between the resonance mode of the PhC and the graphene can be controlled. Therefore, as in the waveguide mode, the modulation of the PhC band-edge laser can be realized by electrically controlling the absorption rate of graphene.

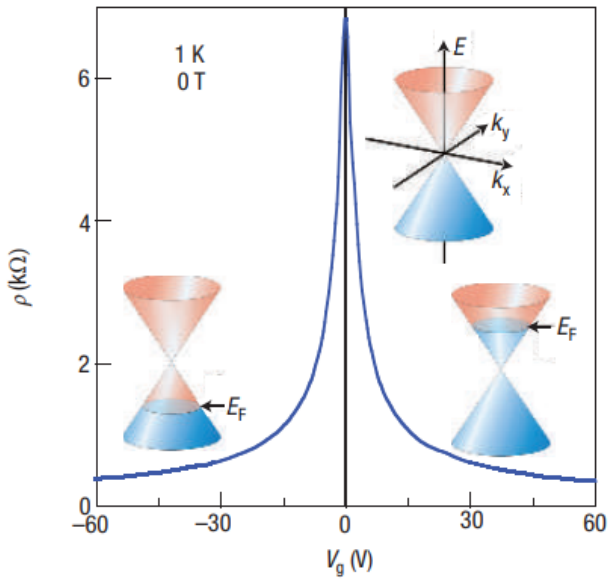

Figure 3-2-1 Ambipolar electric field effect in single-layer graphene [21].

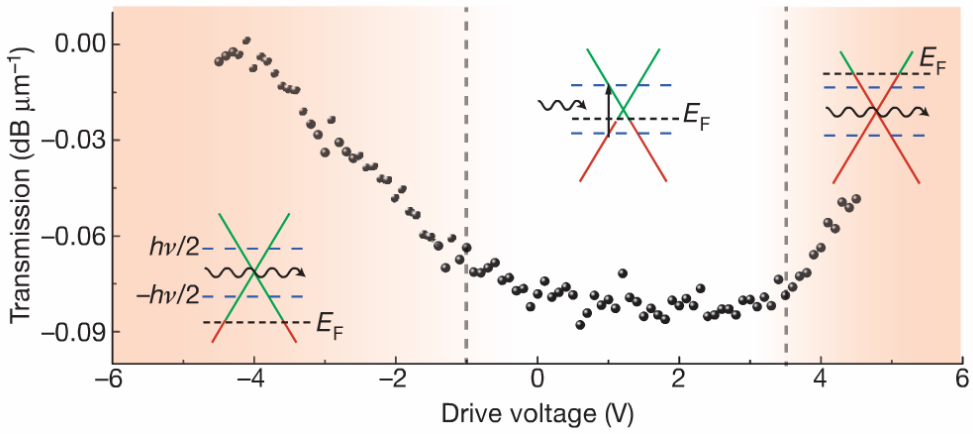

Figure 3-2-2 Static electro-optical response of the device at different drive voltages [7].

3.2.2 Identification of graphene monolayer by Raman spectroscopy

The Fermi level of a monolayer graphene can be tuned across the Dirac point by electrical gating [22]. In order to ensure that our graphene sheet is a high-quality monolayer, we performed Raman spectroscopy measurements. For this purpose, we prepared a dedicated sample by directly transferring a graphene sheet onto a 100-nm-thick SiO_2 layer deposited on a silicon substrate. Figure 3-2-3 shows a Raman spectrum of the graphene sample. We can clearly identify both G and 2D peaks. In particular, the 2D peak at ~2,700 cm^{-1} and the intensity ratio between the two peaks $I_{2D}/I_G > 1$ are direct proof of the existence of a graphene monolayer sheet [23]. The intensity ratio between the two peaks is $I_{2D}/I_G \approx 1.5$, which is much lower than the values observed by others, indicating that our graphene layer is not neutral but doped unintentionally [24]. In addition, the D peak (at ~1,350 cm^{-1}) is negligible, which suggests that our graphene sheet has a high quality and very low amount of defects created during the growth and transfer process [25].

To determine the degree of Fermi level shift in graphene monolayer, I-V characteristics were measured in a graphene FET structure as shown in Fig. 3-2-4. The measured Dirac voltage was V_0 ~58 V. This is consistent with the analysis that graphene is doped in Raman spectrum analysis. Since the theoretical Fermi level shift is $E_F = \hbar v_F \sqrt{\frac{\pi \varepsilon_0 \epsilon_r}{ed} \left| V_g - V_0 \right|}$, we obtained a Fermi level shift of ~250 meV.

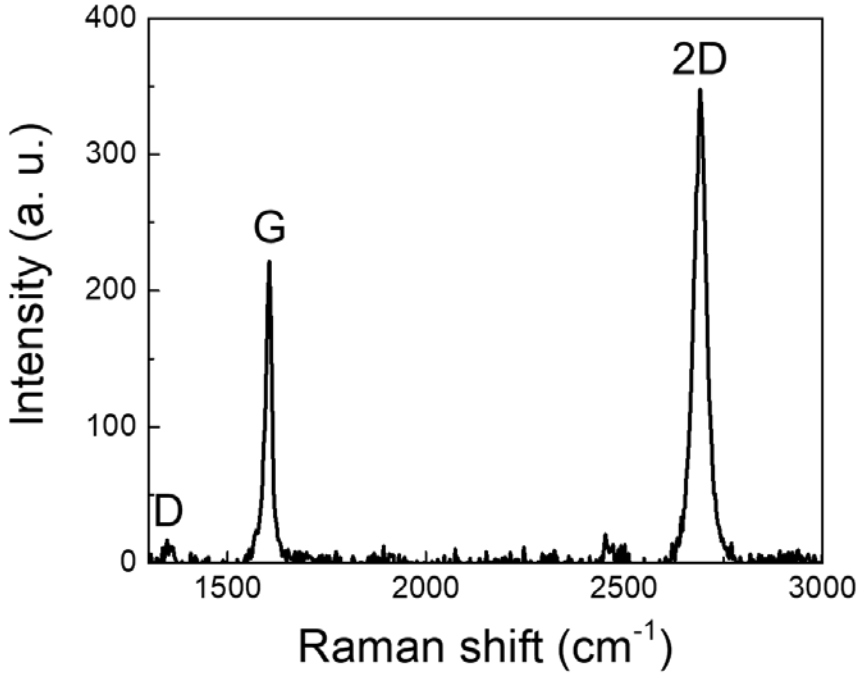

Figure 3-2-3 Raman spectrum taken for a monolayer graphene sheet.

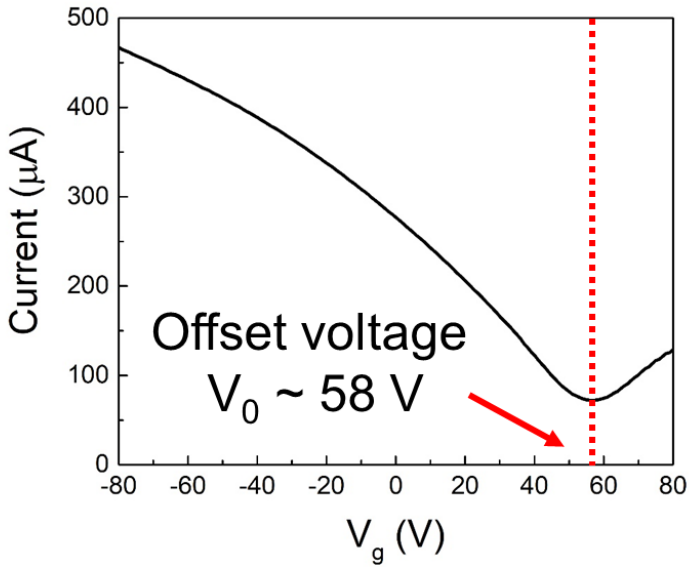

Figure 3-2-4 I-V curve of the monolayer graphene FET device.

3.2.3 Tuning of optical absorption of graphene monolayer

In order to demonstrate the effects of electrical gating on the optical absorption by graphene, we prepared a blank device as shown in Fig. 3-2-5, composed of a graphene monolayer, electrode, and ion-gel film, produced on a microscope slide. The blank device is almost the same as the full device shown in Fig. 3-3-5, except for the lack of the PBE laser and SiO_2 spacer layer. We then applied a gate voltage to the blank device and investigated the changes of the optical transmittance through the graphene sheet, using a 1550 nm continuous-wave laser diode (LD). The measured transmittance T values at the gate voltage range of $-1.0\ \text{V} \leq V_g \leq 1.0\ \text{V}$ are summarized in Fig. 3-2-6. The optical transmittance changes monotonically from ~88.1% at $V_g = -1.0$ V to ~86.8% at $V_g = +1.0$ V. The overall trend is in a good agreement with the FDTD-calculated transmittance change ΔT (red curve in Fig. 3-2-5). This demonstrates that with the aid of ion-gel, the optical loss at the graphene sheet can be controlled by adjusting the gate voltage (smaller than 1 V). For an undoped neutral graphene, the Fermi-level tuning occurs either by electron extraction from the valence band or by electron injection into the conduction band, depending on the polarity of the gate bias voltage. The Fermi-level tuning changes the graphene absorption through the Pauli blocking. However, for our sample, the charge neutrality, at which the Fermi level is aligned with the Dirac point and the transmittance (absorbance) reaches its minimum (maximum) value, occurred at a positive gate voltage. We believe that this is caused by the unintentional doping of the graphene sheet such that the Fermi level at $V_g = 0$ V is below the Dirac point. By fitting the measured data with the simulations results, we estimated that the charge neutrality in the graphene sheet was obtained at $E_F \approx 350$ meV. This is higher than the Fermi level shift measured previously via the graphene FET. The larger fermi level shift appears

to be due to the ion-gel film. The Dirac gate voltage, which has the minimum transmittance through the fermi level shift, is about 1.25V. Therefore, in this study, we adjusted the gate voltage within the negative range of $-1.0\ V \leq Vg \leq 0\ V$. The insets of Fig. 3-2-6 illustrate the optical absorption in the unintentionally p-doped graphene.

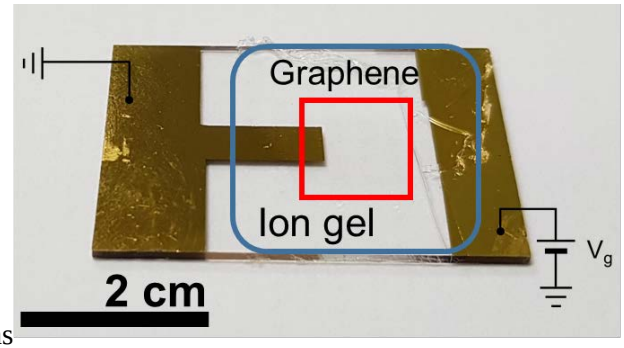

Figure 3-2-5 Photograph of fabricated device for measurement of the change of transmittance of graphene monolayer.

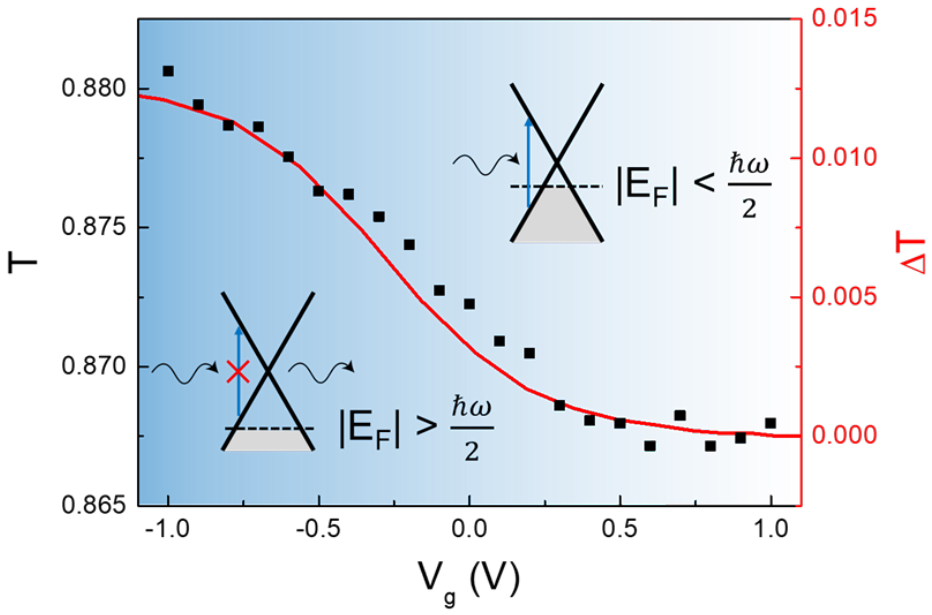

Figure 3-2-6 Optical transmittance through a graphene monolayer measured at 1550 nm as a function of gate voltage. It also shows the transmittance change, which is simulated using the FDTD method.

3.3 Electrical modulation of PhC band-edge laser with graphene monolayer

3.3.1 PhC-graphene device structure

Figure 3-3-1 shows a schematic of the device structure. A honeycomb-lattice 2D PhC pattern was generated on an InP-based MQW epilayer using electron-beam lithography. The PhC pattern was then transferred to the underlying MQW layer using a reactive-ion etch, followed by a selective wet chemical etch of the InP etch-sacrificial layer underneath the MQW epilayer to produce an air-bridge type PhC PBE laser device. A 60-nm-thick SiO_2 spacer layer was then deposited on top of the PhC PBE laser using PECVD. Subsequently, a graphene monolayer sheet was transferred on the obtained structure. The SiO_2 spacer layer determines the distance between the MQW slab waveguide and graphene sheet, which affects the degree of optical loss at the graphene sheet. After the deposition of a Ti/Au electrode on the PhC device and microscope slide using an electron-gun evaporator, the PhC device was mounted on the microscope slide. Then, an ion-gel film was attached to the entire structure to complete the device fabrication (see Section 3.3.2 for a detailed description). Figure 3-3-5 shows a photograph of the fabricated device. The area enclosed by the red square corresponds to the illustration in Fig. 3-3-1. The rounded blue box approximately outlines the boundary of the ion-gel film. Figure 3-3-2 shows a scanning electron microscope (SEM) image of the 2D PhC pattern. Although it is challenging to notice it in the figure, the PhC structure is actually covered by a graphene layer, which indicates the high-quality growth and transfer of the graphene monolayer sheet. The distance between two nearest air-holes is a = 450 nm, while the air-hole radius is $r = 0.32a$. Figure 3-3-3 shows the corresponding photonic band structure of the honeycomb-lattice PhC membrane structure, calculated for the transverse-electric (TE) polarization using the PWE method. For the modeling, all structural parameters were chosen such that the second zone center PBE mode (Γ_2)

matches with the emission band of the InGaAsP MQW, which is shaded in light-blue in the figure. Inset of Fig. 3-3-2 shows the TE field ($E_{\parallel} = \sqrt{E_x^2 + E_y^2}$) distribution profile of the Γ_2 PBE mode, calculated using the FDTD method. One can easily notice that the high-electric-field region significantly overlaps with the active MQW region.

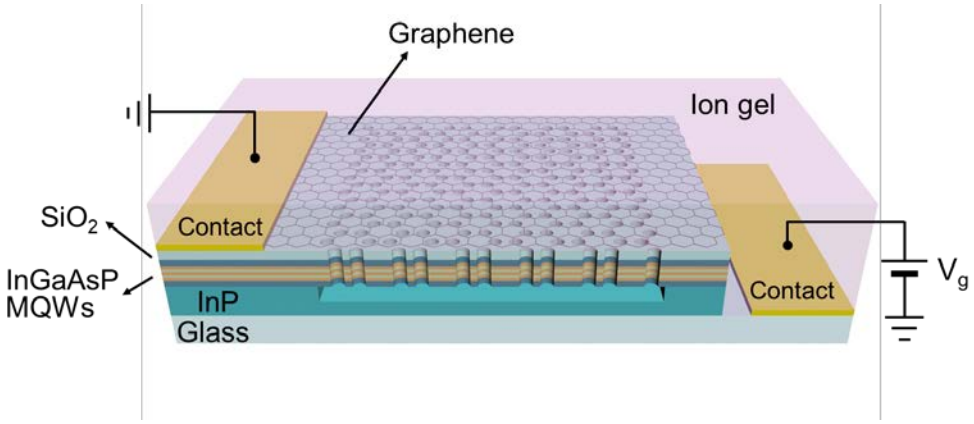

Figure 3-3-1 Schematic of the entire device structure.

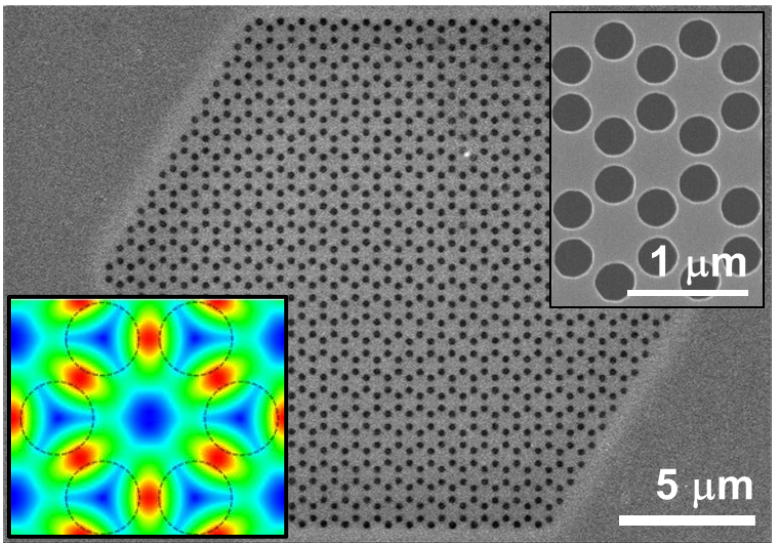

Figure 3-3-2 SEM image of a graphene-covered PhC structure. Shown in the inset is a magnified image and Transverse electric field profile.

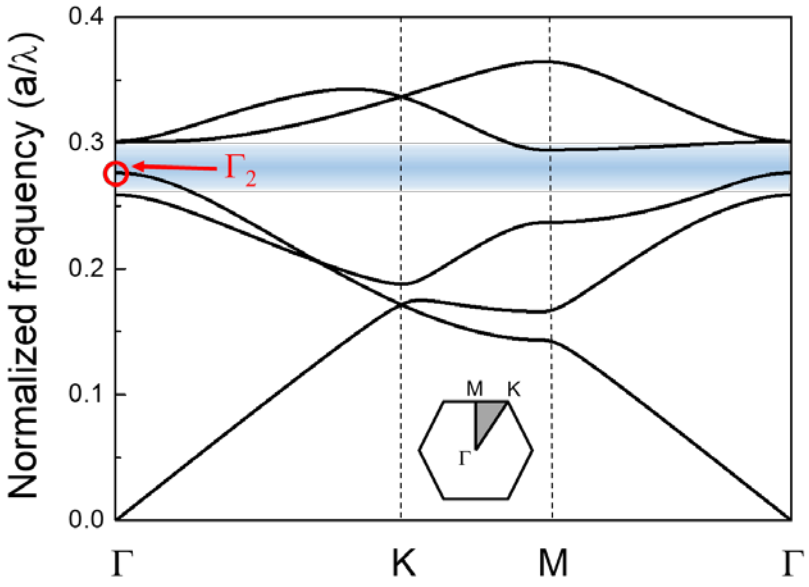

Figure 3-3-3 Band structure calculated for the honeycomb lattice PhC structure.

3.3.2 Device fabrication

Figure 3-3-4 is a schematic image of the device fabrication process. Device fabrication began with the deposition of a 50-nm-thick Si_3N_4 hardmask layer on a semiconductor epi structure, composed of a 230-nm-thick InGaAsP multi-quantum well layer and a 1000-nm-thick InP sacrificial layer, using PECVD method. An array of honeycomb-lattice PhC patterns were generated by electron-beam lithography. The distance between the two nearest air-holes was 450 nm while the air-hole radius was 0.32*a*. The size of each PhC pattern was ~ 18×18 μm^2. The PhC patterns were transferred down to the Si_3N_4 and MQW layers sequentially by RIE using the gas mixtures of O_2/CF_4 and CH_4/H_2, respectively. Then, wet-etching was performed at 4°C using HCl aqueous solution (3:1) to selectively remove the InP sacrificial layer, which resulted in a completed PBE laser sample in a free-standing membrane form. Next, a 60-nm-thick SiO2 spacer layer was deposited on the sample by PECVD.

A monolayer graphene sheet, which was grown on a Cu foil by TCVD method, was procured commercially from Graphene Square. After a PMMA layer was spin-coated directly on the graphene sheet as a temporary handling layer, we removed the Cu foil in a $FeCl_3$ solution to obtain in a free-standing PMMA/graphene film floating on water. The PMMA/graphene film was then transferred onto the PBE laser sample. The PMMA layer was removed with acetone, and dried by the CPD method to prevent the suspended portions of the graphene sheet on the PhC membrane from being damaged by surface tension during the drying process. The Ti/Au (15/200 nm) gate electrodes were deposited on both the graphene surface of the sample and also on the glass substrate by electron-gun evaporator. Then, the PBE laser sample was bonded on the glass substrate using epoxy, and the graphene sheet on the sample and one of the electrodes on the glass substrate were electrically connected to each other using carbon paste. Finally, an ion-gel film for electrolyte gating was transferred and bonded on the fabricated device. Figure 3-3-5 shows a photograph of the fabricated device.

The ion-gel film was synthesized following the literature [13]. Briefly, an ion-gel solution was prepared first by dissolving poly (vinylidene fluoride-co-hexafluoropropylene), P(VDF-HFP), as the polymer, and 1-ethyl-3-methylimidazolum bis(trifluoromethylsulfonyl)amide, [EMI][TFSA], as the ion liquid, in acetone in a weight ratio of 1:4:7. In the P(VDF-HFP) polymer, the PHFP block is selectively dissolved in the ion liquid whereas the PVDF block is not, making the ion-gel solution gelated. After the ion-gel solution was spin-coated on a substrate to form an ion-gel film, it was cured in a vacuum oven at 80°C for 24 hours to remove the residual solvent. The completed ion-gel film was cut into an appropriate size using a razor blade, which was then transferred onto the fabricated device using a tweezer.

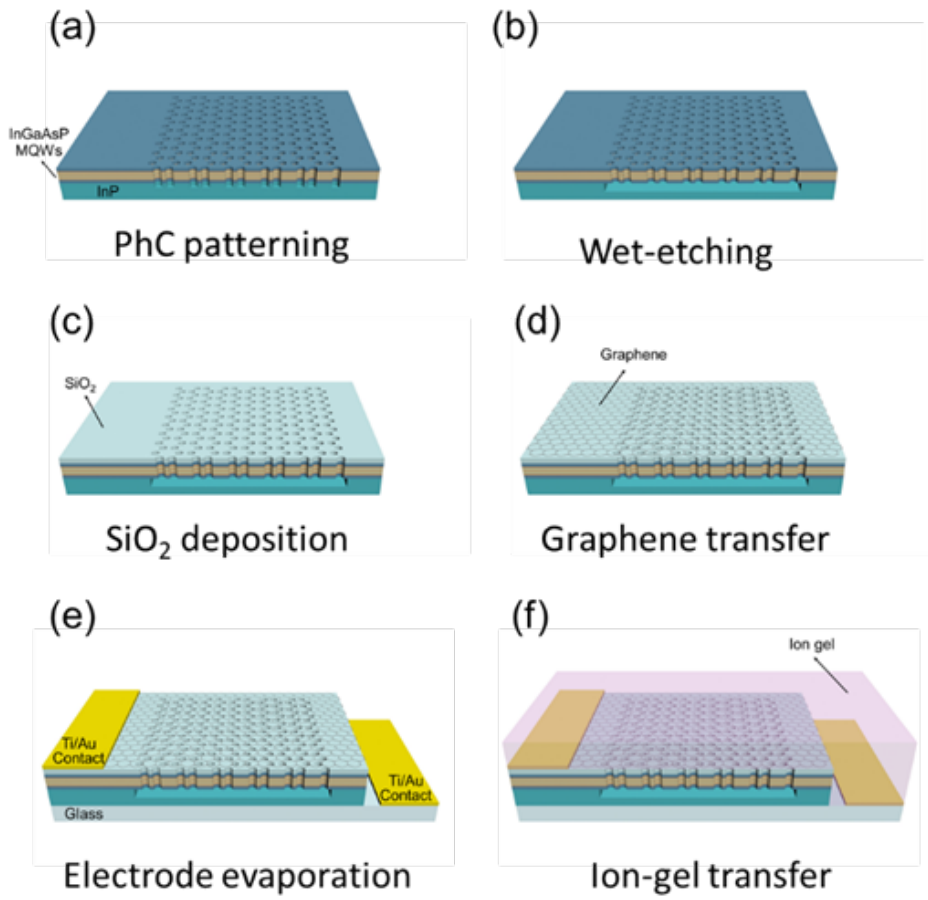

Figure 3-3-4 Fabrication steps for the PhC band-edge laser device. (a) Patterning and etching of PhC patterns on the InGaAsP MQW slab by e-beam lithography and RIE. (b) Selective wet-chemical etching of the InP sacrificial layer in HCl solution. (c) SiO2 spacer layer deposition by PECVD. (d) Transfer of a graphene sheet onto the PBE laser sample. (e) Ti/Au deposition on the graphene and glass substrate using e-gun evaporator, and epoxy bonding of the PBE laser sample on the glass substrate. (f) Transfer of an ion-gel film onto the entire device.

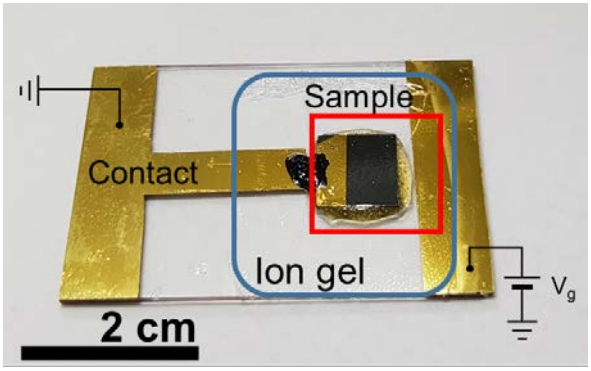

Figure 3-3-5 Photograph of a fabricated device.

3.3.3 Measured PL spectra

In order to induce a PBE lasing, the fabricated devices were optically excited using a 1064 nm pulsed LD (500 kHz frequency; 1% duty cycle). For a simultaneous optical excitation and spectral measurement, we employed a compact micro-photoluminescence (μ-PL) setup based on a 1 X 2 wavelength-division-multiplexing optical fiber coupler [26]. Figure 3-3-6 is a schematic of the optical fiber based μ -PL measurement setup. As the fiber probe tip was in a close proximity (< 30 μm) to the sample during the measurement, the optically excited area (~70 μm in diameter) was estimated to be slightly larger than the core diameter of the optical fiber (62.5 μm). During the pulsed optical excitation, a gate voltage was applied across the ion-gel film using a DC power supply. We obtained a low leakage current (smaller than 1 μA) for the entire gate voltage range. The μ-PL spectra were measured at various optical excitation levels and gate voltages to obtain a performance map of the PBE laser.

Figure 3-3-7 shows the μ-PL spectra measured at various optical excitation levels; the gate voltage was fixed at $V_g = -1.0$ V. At excitation power densities smaller than ~0.45 kW/cm^2, we did not observe any sign of lasing. However, at higher excitation densities, a sharp single emission peak emerged, and its intensity continuously increased, which is a clear sign of single-mode lasing with a well-defined threshold. We identified that the lasing peak corresponded to the Γ_2 PBE mode, as the PhC structure was designed such that the Γ_2 mode was positioned (spectrally) at the center of the MQW emission band (Fig. 3-3-3). Repeated measurements at different gate voltages showed that the single-mode lasing action was sustained but with different threshold values, as summarized in Fig. 3-3-8. It is shown that the PBE laser threshold rapidly increased with the increase of the gate voltage from ~0.46 kW/cm^2 at $V_g = -1.0$ V to ~0.54 kW/cm^2 at $V_g = -0.5$ V. These results are a clear indication that the PBE laser performance can be electrically controlled. We did not observe any lasing action for gate voltages larger than −0.5 V, most likely owing to the very high absorption loss at the graphene monolayer.

More relevant for the direct electrical modulation should be the relationship between the laser output and gate voltage. Figure 3-3-9 shows laser spectra recorded for various gate voltages, at a fixed optical excitation power density of ~0.55 kW/cm^2. For $V_g > -0.5$ V, there is no (or it is very weak) sign of lasing. However, a well-defined single-mode laser peak appeared at 1596 nm for $V_g \leq -0.5$ V, while the PBE laser output increased monotonously with the decrease of the gate voltage. Figure 3-3-10 summarizes the maximum output intensity as a function of the gate voltage, which directly demonstrates that the PBE laser output can be modulated by applying a gate voltage in the range of -1.0 V $\leq V_g \leq -0.5$ V.

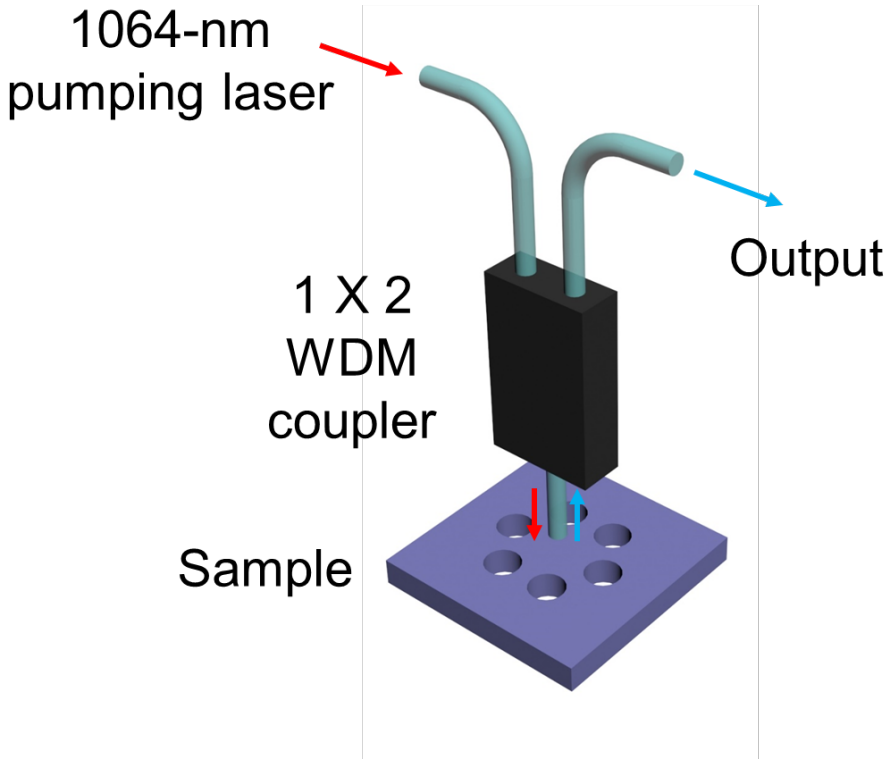

Figure 3-3-6 Schematic of the optical fiber based micro-PL measurement setup.

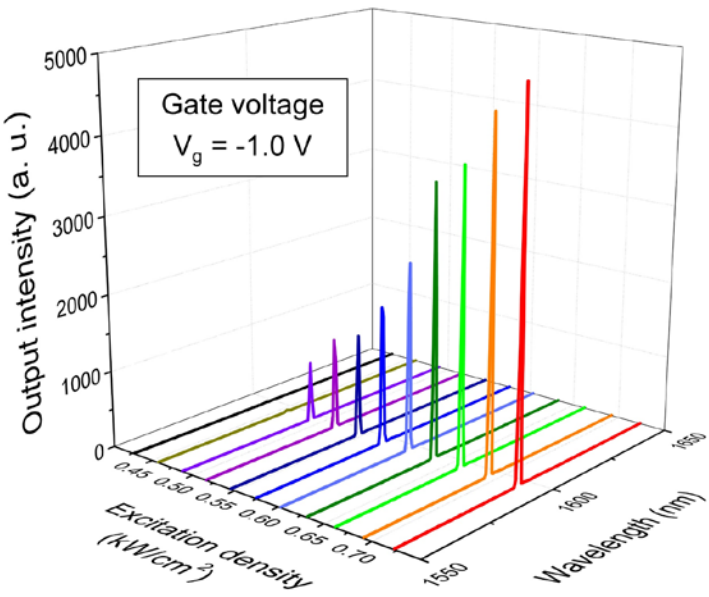

Figure 3-3-7 Micro-photoluminescence spectra measured at various optical excitation levels, at a fixed gate voltage of V_g = -1.0 V.

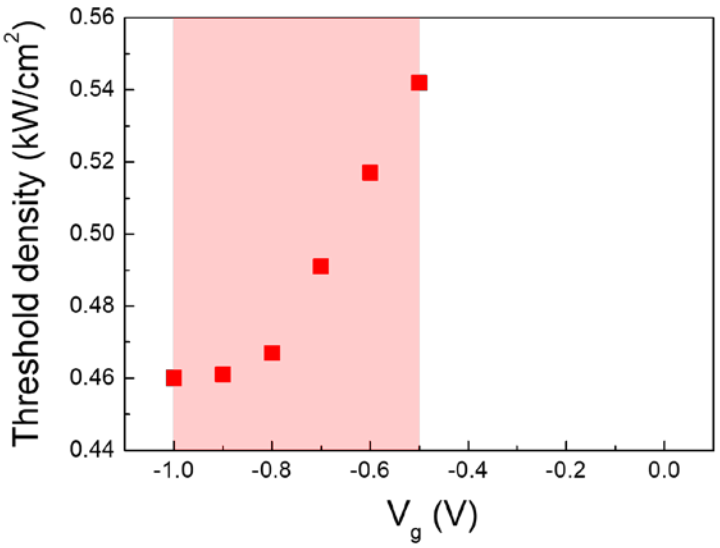

Figure 3-3-8 Laser thresholds determined for different gate voltages.

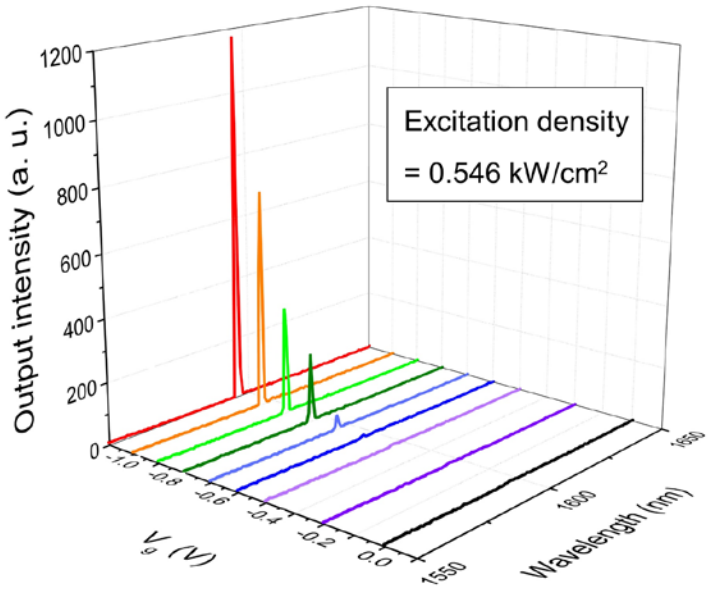

Figure 3-3-9 Micro-photoluminescence spectra measured at various gate voltages within the range of -1.0 V≤V_g≤0 V, but at a fixed optical excitation level.

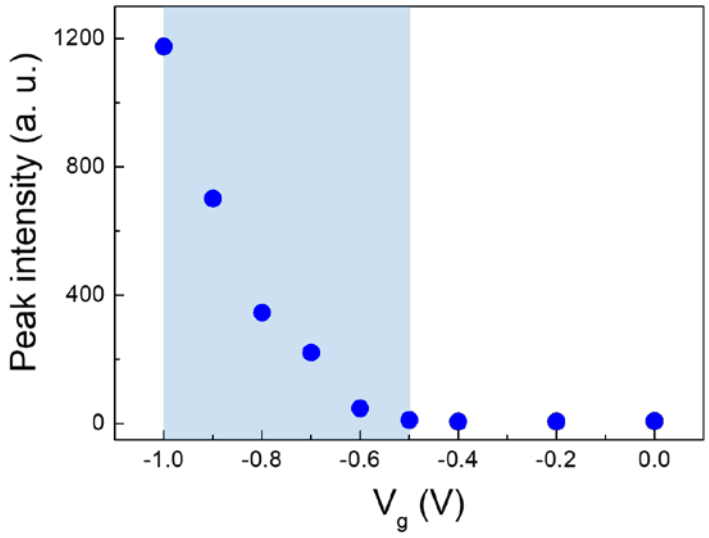

Figure 3-3-10 Peak laser intensity as a function of gate voltage, all measured at a fixed optical excitation level.

3.3.4 Calculated optical absorption and Q-factor of PhC-graphene structure by FDTD method

For a theoretical confirmation, we performed FDTD simulations on a model device structure. Figure 3-3-11 shows the calculated absorption by the graphene monolayer sheet in the PhC-graphene structure. As the interband transitions of electrons are responsible for the optical absorption by the graphene monolayer, the value of the optical power dissipation can be obtained by analyzing the interaction between the corresponding optical conductivity and resonant Γ_2 PBE mode.

Optical loss of graphene can be described by optical conductivity σ [27]. In the Kubo formalism, the optical conductivity is contributed by both the interband and intraband transitions ($\sigma = \sigma_{inter} + \sigma_{intra}$), which can be formulated by [28]

$$\sigma_{inter}(\omega, \mu_c, \Gamma, T) = \frac{ie^2(\omega - i2\Gamma)}{\pi\hbar^2}\int_0^\infty \frac{f_d(-\varepsilon) - f_d(\varepsilon)}{(\omega - i2\Gamma)^2 - 4(\varepsilon/\hbar)^2} d\varepsilon \qquad (1)$$

and

$$\sigma_{intra}(\omega, \mu_c, \Gamma, T) = \frac{-ie^2}{\pi\hbar^2(\omega - i2\Gamma)}\int_0^\infty \varepsilon\left(\frac{\partial f_d(\varepsilon)}{\partial\varepsilon} - \frac{\partial f_d(-\varepsilon)}{\partial\varepsilon}\right) d\varepsilon. \qquad (2)$$

where $f_d(\varepsilon) = [e^{(\varepsilon-\mu_c)/k_BT} + 1]^{-1}$ is the Fermi-Dirac distribution function, ω is the angular frequency, Γ is the scattering rate, μ_c is the chemical potential, T is temperature, $-e$ is the electron charge, $\hbar$ is the reduced Plank constant, and k_B is the Boltzmann constant.

In general, the optical absorption of a graphene monolayer occurs predominantly by the interband transition so that the optical power absorbed by graphene on the x-y plane can be expressed as

$$\langle P \rangle = \frac{1}{2}\int \boldsymbol{J} \cdot \boldsymbol{E}\, dxdy = \frac{\sigma_{inter}}{2}\int (|E_x|^2 + |E_y|^2) dxdy, \qquad (3)$$

where $\boldsymbol{J}$ is the surface current density given by Ohm's law, $\boldsymbol{J}=\sigma_{inter}\boldsymbol{E}$, and $\boldsymbol{E}$ is the transverse electrical field [29].

We calculated the transverse electric field distribution at the graphene plane of the PhC-graphene structure by FDTD simulation. Then we obtained the optical absorption in the PhC-graphene system by substituting the simulated transverse electric field distribution of the PBE mode and the interband conductivity (1) into the power absorption equation (3). The parameters used in the simulation are Γ = 0.015 eV [30], T = 300 K, and 0 eV ≤ μ_c ≤ 0.5 eV. We assumed that the thicknesses of InGaAsP slab, SiO_2 spacer layer, and ion-gel film were 230 nm, 60 nm, and 2 μm, respectively, while their refractive indices were assumed to be 3.4, 1.4 and 1.4, respectively. Resultant optical absorption is presented in Fig. 3-3-11 as a function of gate voltage. The total absorption by graphene in the ungated state (V_g = 0 V) is ~54%, which is reduced to ~21% at V_g = -1.0 V.

Figure 3-3-11 shows that the optical absorption by the graphene monolayer increases with the gate voltage. The general trend is qualitatively consistent with the experimentally determined laser thresholds shown in Fig. 3-3-8. In addition, we calculated the photon decay rate in the PhC-graphene structure for various gate voltages, as shown in Fig. 3-3-12. We synchronously excited multiple electric dipoles that were distributed randomly across the device structure and monitored the subsequent time evolution of the accumulated optical power of the Γ_2 PBE mode. We obtained the value of the photon decay rate γ by fitting the results using the equation, $P(t) = P_0 e^{-2\gamma t}$. The simulation results clearly show that the photons decay more rapidly at higher gate voltages; the overall behavior is very similar to the independently calculated optical absorbance data shown in Fig. 3-3-11. The Q-factor of the cavity can be estimated using the photon decay time $(\tau = 1/\gamma)$ and equation $\tau = 2Q/\omega_0$, where ω_0 is the Γ_2 resonance frequency. The Q-factor obtain such are shown in Fig. 3-3-12. As the InGaAsP MQWs are assumed to be lossless in the simulations, possible loss mechanisms are the radiation loss (owing to the device

structure) and optical absorption (by the graphene monolayer). The total Q factor of the PhC-graphene structure can be expressed as: $Q^{-1} = Q_{\mathrm{rad}}^{-1} + Q_{\mathrm{G}}^{-1}$, where Q_{rad} and Q_{G} are the Q-factors that correspond to the radiation loss and graphene absorption, respectively. However, we can easily distinguish Q_{G} from Q_{rad}, as only Q_{G} depends on the gate voltage. Using the above arguments, we can conclude that the background Q value (~1000) corresponds to Q_{rad}, while the V_{g}-dependent Q (in the range of ~1000–2000) corresponds to Q_{G} (Fig. 3-3-12).

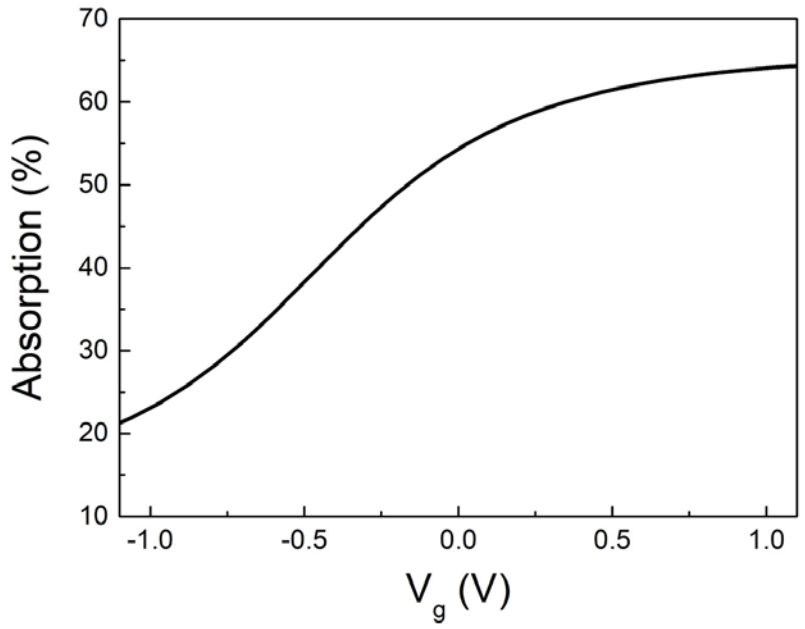

3-3-11 FDTD simulated optical absorption as a function of gate voltage.

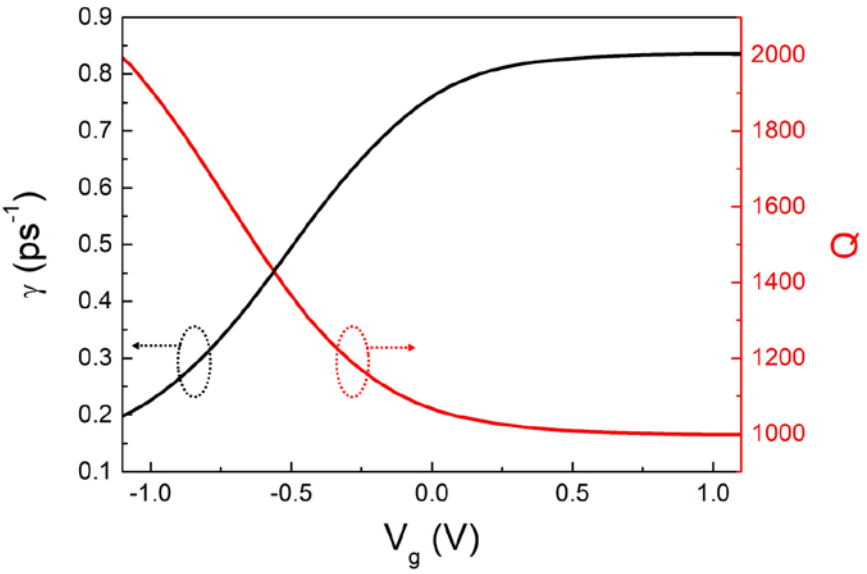

3-3-12 Gate voltage dependence of photon decay rate γ and cavity Q-factor, obtained from FDTD simulations.

3.3.5 Measured optical power and time response

As mentioned above, the high output power and tailored emission direction are unique advantages of the PBE lasers. Therefore, a successful electrical modulation of a PBE laser could produce a directly modulated large laser power in a predefined emission direction, which is highly desirable for future PIC applications. On the other hand, a fast signal modulation should be of a key importance for real applications. In order to assess the modulation characteristics of the proposed device, we examined the temporal response of the PBE laser output to an abrupt change of the gate voltage: from 0 V to −1.0 V for a laser turn-on and from −1.0 V to 0 V for a laser turn-off. The measurements were performed conveniently by connecting the output port of the fiber-based μ-PL setup to an optical power meter (AQ2201, Yokogawa), instead of a spectrometer. Figures 4a and 4b show the time responses to a laser turn-on and turn-off, respectively. Throughout the measurements, the 1064 nm optical excitation power density was fixed at ~0.72 kW/cm^2. At this excitation condition, the steady-state PBE laser output power at Vg = -1.0 V was ~2.2 μW. It is worth mentioning that this value of the output power is ~1000 times larger than the nanowatt-level output power of conventional cavity-based PhC lasers [31]. The rise and fall times, estimated by fitting the experimental data in Figs. 4a and 4b, are $\tau_{rise} \approx 0.45$ s and $\tau_{fall} \approx 25.7$ s, respectively. Both responses are too slow for practical applications. The slow electrical response is an intrinsic issue of the ion-gel, not of the PBE laser or graphene. The ion-gel performance relies on the mobility of the constituent ions inside the electrolyte, which is very low. This notion explains the discrepancy of the rise and fall times. During the turn-on, ions move relatively rapidly in response to the applied electrical field; however, during the turn-off, ions diffuse back to their original random state, which lasts significantly longer. We may expect faster temporal responses of PBE lasers (in principle, of any PhC-based laser) with the introduction of an ion-gel that has a significantly improved ion conductivity or with the use of alternative ingenious electrical methods that can control the Fermi level of graphene.

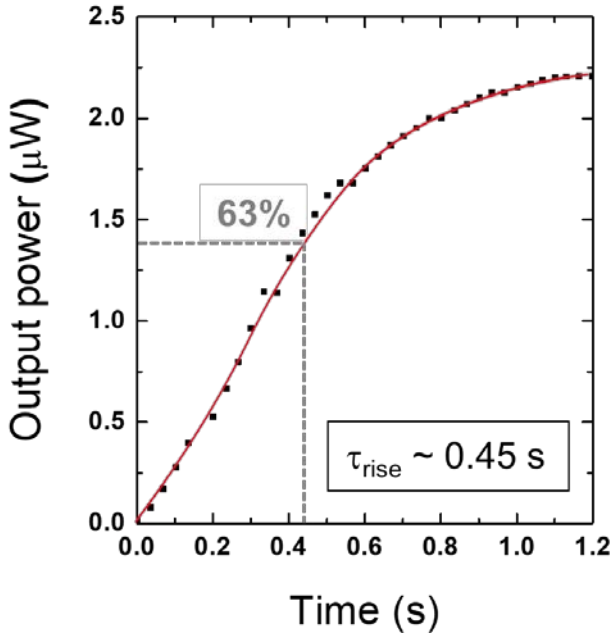

Figure 3-3-13 Temporal response. Fiber-coupled laser output power measured as a function of time: after laser turn-on (V_g switched from 0 to -1.0 V).

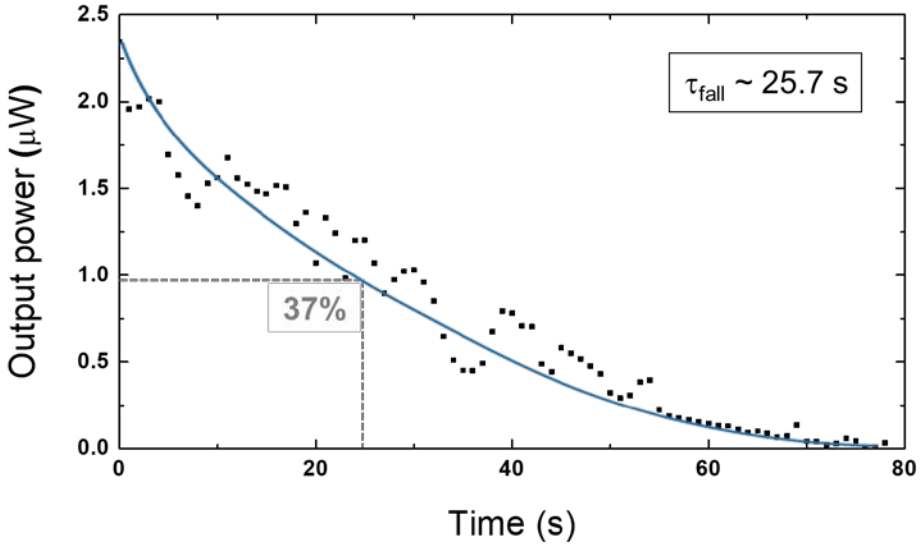

Figure 3-3-14 Temporal response. Fiber-coupled laser output power measured as a function of time: after laser turn-off (V_g switched from -1.0 to 0 V).

3.4 Summary

In conclusion, we successfully demonstrated a direct electrical modulation of a PBE laser by controlling the Fermi level of the graphene monolayer attached in close proximity to the PBE laser. A low voltage modulation at $|V_g| < 1$ V was achieved by electrolyte gating, where an ion-gel was used as the gate dielectric. By combining a graphene monolayer and ion-gel film, we showed that a low gate voltage can modify the optical absorption of graphene. Then, we applied the low-voltage electrical gating method to an optically excited InGaAsP MQW PBE laser device. We successfully directly modulated a microwatt-level PBE laser output within gate voltages smaller than 1 V. Although the challenges with the modulation speed remain, this study demonstrates that the graphene monolayer is sufficiently effective to control the performance of various PhC-based photonic devices, which extends the applicability of graphene. We believe that future studies could achieve an electrical modulation of the Fermi level of graphene at low voltages and fast speeds, which can improve the performances of the existing photonic devices.

References

[1] C. Lee, X. Wei, J. W. Kysar, and J. Hone, "Measurement of the Elastic Properties and Intrinsic Strength of Monolayer Graphene," Science **321**, 385-388 (2008).

[2] K. I. Bolotin, K. J. Sikes, Z. Jiang, M. Klima, G. Fudenberg, J. Hone, P. Kim, and H. L. Stormer, "Ultrahigh electron mobility in suspended graphene," Solid State Communications **146**, 351-355 (2008).

[3] Y. Zhang, Y. Tan, H. L. Stormer, and P. Kim, "Experimental observation of the quantum Hall effect and Berry's phase in graphene," Nature 438, 201-204 (2005).

[4] A. A. Balandin, S. Ghosh, W. Bao, I. Calizo, D. Teweldebrhan, F. Miao, and C. Lau, "Superior Thermal Conductivity of Single-Layer Graphene," Nano Letter **8**, 902-907 (2008).

[5] R. R. Nair, P. Blake, A. N. Grigorenko, K. S. Novoselov, T. J. Booth, T. Stauber, N. M. R. Peres, and A. K. Geim, "Fine Structure Constant Defines Visual Transparency of Graphene," Science **320**, 1308 (2008).

[6] Q. Bao, H. Zhang, B. Wang, Z. Ni, C. Lim, Y. Wang, D. Tang, and K. Loh, "Broadband graphene polarizer," Nature Photonics **5**, 411-415 (2011).

[7] M. Liu, X. Yin, E. Ulin-Avila, B. Geng, T. Zentgraf, L. Ju, F. Wang, and X. Zhang, "A graphene-based broadband optical modulator," Nature **474**, 64-67 (2011).

[8] F. Xia, T. Mueller, Y. Lin, A. Valdes-Garcia, and P. Avouris, "Ultrafast graphene photodetector," Nature Nanotechnology **4**, 839-843 (2009).

[9] K. S. Novoselov, A. K. Geim, S. V. Morozov, D. Jiang, Y. Zhang, S. V. Dubonos, I. V. Grigorieva, and A. A. Firsov, "Electric Field Effect in Atomically Thin Carbon Films," Science **306**, 666-669 (2004).

[10] H. Liu, Y. Liu, and D. Zhu, "Chemical doping of graphene," Journal of Materials Chemistry **21**, 3335-3345 (2011).

[11] A. Facchetti, M. Yoon, T. J. Marks, "Gate Dielectrics for Organic Field-Effect Transistors: New Opportunities for Organic Electronics," Advanced Materials **17**, 1705-1725 (2005).

[12] J. Cho, J. Lee, Y. Xia, B. Kim, Y. He, M. J. Renn, T. P. Lodge, and C. D. Frisbie, "Printable ion-gel gate dielectrics for low-voltage polymer thin-film transistors on plastic," Nature Materials **7**, 900-906 (2008).

[13] K. Lee, M. Kang, S. Zhang, Y. Gu, T. P. Lodge, and C. D. Frisbe, "“Cut and Stick” Rubbery Ion Gels as High Capacitance Gate Dielectrics," Advanced Materials **24**, 4457-4462 (2012).

[14] B. Kim, H. Jang, S. Lee, B. Hong, J. Ahn, and J. Cho, " High-Performance Flexible Graphene Field Effect Transistors with Ion Gel Gate Dielectrics," Nano Letter **10**, 3464-3466 (2010).

[15] J. Lee, M. J. Panzer, Y. He, T. P. Lodge, and C. D. Frisbie, "Ion Gel Gated Polymer Thin-Film Transistors," Journal of the American Chemical Society **129**, 4532-4533 (2007).

[16] V. Narasimhan, S. Park, "An Ion Gel as a Low-Cost, Spin-Coatable, High-Capacitance Dielectric for Electrowetting-on-Dielectric (EWOD)" Langmuir **31**, 8512-8518 (2015).

[17] X. Gan, K. Mak, Y. Gao, Y. You, F. Hatami, J. Hone, T. Heinz, D. Englund, "Strong Enhancement of Light–Matter Interaction in Graphene Coupled to a Photonic Crystal Nanocavity," Nano Letter **12**, 5626-5631 (2012).

[18] A. Majumdar, J. Kim, J. Vuckovic, and F. Wang, "Electrical Control of Silicon Photonic Crystal Cavity by Graphene," Nano Letter **13**, 515-518 (2013).

[19] X. Gan, R. Shiue, Y. Gao, K. Mak, X. Yao, L. Li, A. Szep, D. Walker, Jr., J. Hone, T. F. Heinz, and D. Englund, "High-Contrast Electrooptic Modulation of a Photonic Crystal Nanocavity by Electrical Gating of Graphene," Nano Letter **13**, 691-696 (2013).

[20] M. Hwang, H. Kim, K. Kim, K. Jeong, J. Park, J. Choi, J. Kang, J. Lee, W. Park, J. Song, M. Seo, and H. Park, "Switching of Photonic Crystal Lasers by Graphene," Nano Letter **17**, 1892-1898 (2017).

[21] A. K. Geim, and K. S. Novoselov, “The rise of graphene,” Nature materials **6**, 183-191 (2007)

[22] Y. Yu, Y. Zhao, L. E. Brus, K. S. Kim, and P. Kim, "Tuning the Graphene Work Function by Electric Field Effect," Nano Letter **9**, 3430-3434 (2009)

[23] A. C. Ferrari, "Raman spectroscopy of graphene and graphite: Disorder, electron-phonon coupling, doping and nonadiabatic effects," Solid State Communications **143**, 47-57 (2007).

[24] A. Das, S. Pisana, B. Chakraborty, S. Piscanec, S. K. Saha, U. V. Waghmare, K. S. Novoselov, H. R. Krishnamurthy, A. K. Geim, A. C. Ferrari, and A. K. Sood, “Monitoring dopants by Raman scattering in an electrochemically top-gated graphene transistor,” Nat. Nanotechnology **3**, 210-215 (2008).

[25] A. C. Ferrari, J. C. Meyer, V. Scardaci, C. Casiraghi, M. Lazzeri, F. Mauri, S. Piscanec, D. Jiang, K. S. Novoselov, S. Roth, and A. K. Geim, "Raman Spectrum of Graphene and Graphene Layers," Physics Review Letter **97**, 187401 (2006).

[26] C. Han, H. Kim, H. Jung, S. Lee, P. G. Jablonski, and H. Jeon, "Origin and biomimicry of weak iridescence in black-billed magpie feathers," Optica **4**, 464-467 (2017).

[27] J. M. Dawlaty, S. Shivaraman, J. Strait, P. George, M. Chandrashekhar, F. Rana, M. G. Spencer, D. Veksler, and Y. Chen, "Measurement of the optical absorption spectra of epitaxial graphene from terahertz to visible," Appl. Phys. Lett. **93**, 131905 (2008)

[28] G. W. Hanson, "Dyadic Green's functions and guided surface waves for a surface conductivity," J. Appl. Phys. **103**, 064302 (2008).

[29] H. Li, Y. Anugrah, S. J. Koester, and M. Li, "Optical absorption in graphene integrated on silicon waveguides," Appl. Phys. Lett. **101**, 111110 (2012)

[30] A. Majumdar, J. Kim, J. Vuckovic, and F. Wang, " Electrical Control of Silicon Photonic Crystal Cavity by Graphene," Nano Lett. **13**, 515-518 (2013).

[31] M. Loncar, T. Yoshie, A. Scherer, P. Gogna, and Y. Qiu, "Low-threshold photonic crystal laser," Applied Physics Letter **81**, 2680-2682 (2002).

Chapter 4

Conclusion and Perspective

In this thesis, we observed the effect of the optical absorber on the PhC resonance mode and demonstrated the electrical modulation of the PhC band-edge laser with graphene monolayer.

First, the effect of the optical absorber on the PhC laser structure was experimentally characterized. Graphene monolayer with the partially removed around the cavity structure was integrated on the PhC cavity laser structure. It was confirmed that as the removal region of graphene is widened, the interaction between graphene and PhC cavity mode is reduced and the output of the laser is increased. In addition, it was confirmed that the single-mode laser operation of the PhC cavity laser is possible with the partially removed graphene monolayer. The characteristics of the PhC band-edge laser integrated graphene or metal patterns on the PhC band-edge laser structure were also observed. When the absorber is placed at the antinode of the resonant mode, the resonant mode is attenuated and the laser oscillation is suppressed by the strong interaction between the absorber and the resonant mode. While, when the absorber is placed at the node of the resonance mode, the interaction between the absorber and the resonance mode is not large and the laser oscillation is maintained. In addition, we confirmed that the tendency of the absorber is consistent with the results obtained by FDTD simulation. This study is meaningful in that it has experimentally characterized the effect of light absorber on the PhC resonance mode.

Second, electrical modulation of the PhC band-edge laser was demonstrated by controlling the optical absorption of graphene monolayer on the PhC band-edge laser

structure. When an electric field is applied to the graphene, the Fermi level of the graphene shifts and the absorption of light can be controlled by inhibiting the band transition. A gate voltage was applied to the graphene to observe a 1.5% of transmittance change. In this experiment, the ion-gel film used as a dielectric material has an advantage that it can be operate at a low gate voltage because of its large capacitance. Then, the electrical modulation of the PhC band-edge laser was demonstrated using the change in transmittance of graphene. When the gate voltage was not applied, the laser oscillation was suppressed due to the absorption of the resonance mode by the graphene. However, when a gate voltage of -1.0 V was applied, the laser emission was successful and the characteristics of the laser according to the gate voltage were observed. Observed characteristics are consistent with the results calculated by FDTD simulation, then we have successfully demonstrated the electrical modulation of the PhC band-edge laser.

As applications of PhC laser, PhC lasers are promising light source in the optical communication area due to their compact size and low power consumption. However, for commercialization, the electrical drive and electrical modulation of the PhC laser must precede. Contact design in electrically driven PhC lasers is a complicated problem. This is because the electrode absorbs light while injecting current. Using this study of the optical absorber, it may be helpful for contact design for electrically driven PhC lasers. The modulation of the light source is also a key technology in optical communication. If we further improve the modulation characteristics of PhC lasers, we expect it to be used in on-chip integration applications such as photonic integrated circuits.

국문 초록

광자 결정은 유전율이 다른 두 가지 이상 물질들이 빛의 파장 스케일로 주기적으로 배열된 구조를 말한다. 광자 결정을 통과하는 빛은 균일한 매질을 통과하는 빛에서는 볼 수 없는 독특한 광분산관계를 가진다. 광자 결정에서 나타나는 독특한 광 특성 중에 대표적인 것이 광 밴드갭과 밴드에지 현상이다. 광 밴드갭은 광자의 모드가 존재할 수 없는 주파수 영역으로, 광 밴드갭을 이용하여 캐비티 내에 빛을 강하게 가두는 방식으로 광자 결정 캐비티 레이저를 제작할 수 있다. 또한, 빛의 군속도가 영에 가까워지는 밴드에지를 이용하면 광 이득 물질 내에 정상파 형태의 공진 모드를 형성하여 광 이득을 강화할 수 있고, 이를 이용하여 광자 결정 밴드에지 레이저를 제작할 수 있다.

광자 결정 레이저는 좁은 면적에 제작할 수 있고 소비 전력이 적다는 점에서 잠재력이 큰 레이저이다. 하지만 광자 결정 레이저를 실제로 산업에서 사용하기 위해서는 변조 기술이 선행되어야 한다. 일반적으로 광자 결정 레이저를 발진시키는 광 여기 방식에서 여기 레이저의 변조로는 변조 속도에 있어서 한계가 있다. 따라서, 빠른 속도의 변조를 위해서는 전기적으로 흡수율을 조절할 필요가 있는데, 이 때 광 흡수체로 그래핀을 이용하고자 한다. 그래핀은 탄소 원자들이 2차원 평면상에 배열된 물질로 큰 광 흡수율과 페르미 레벨을 조절하여 광 흡수율을 제어할 수 있다는 점이 특징이다.

본 학위 논문에서는, 첫 번째 연구 주제에서는 광자 결정 레이저

구조 위의 광 흡수체가 광자 결정 공진 모드에 미치는 영향을 실험적으로 분석하였다. InGaAsP 다중양자우물에 광자 결정 구조를 이용하여 1.5 μm 영역 대에서 발진하는 광자 결정 벤드에지 레이저와 캐비티 레이저를 제작하였다. 제작한 광자 결정 캐비티 레이저 구조 위에 중심부를 제거한 그래핀을 집적하였다. 이 때, 그래핀의 제거 영역이 넓어질수록 광자 결정 캐비티 모드와의 상호작용이 줄어들어 레이저의 출력이 증가함을 확인하였다. 더불어 광자 결정 캐비티 레이저의 단일 모드 레이저 발진이 가능함을 확인할 수 있었다. 또한, 광자 결정 밴드에지 레이저 구조 위에 그래핀 또는 금속 패턴을 집적하여 밴드 에지 레이저의 특성 변화를 관찰하였다. 광자 결정 밴드에지 모드는 주기적인 정상파 형태로 나타나는데, 흡수체를 공진 모드의 배 부분에 위치시키면 흡수체와 공진 모드의 강한 상호작용으로 밴드에지 모드가 감쇠하여 레이저 발진이 억제되는 반면, 흡수체를 공진 모드의 마디 부분에 위치시키면 흡수체와 공진 모드의 상호작용이 크지 않아서 레이저 발진이 유지됨을 확인할 수 있었다. 또한, 위 흡수체에 의한 경향성은 유한차분 시간영역 시뮬레이션을 통해 계산한 결과와 일치함을 확인하였다. 이번 연구는 광 흡수체에 의한 광자 결정 공진 모드의 영향을 실험적으로 분석하였다는 점에서 의미를 가진다. 나아가, 전기 구동 레이저의 전극 구조 설계에 적용 가능성을 기대한다.

두 번째 연구 주제에서는, 광자 결정 밴드에지 레이저 구조 위의 그래핀 단일층의 광 흡수율을 조절함으로써 광자 결정 밴드 에지 레이저의 전기적인 변조를 구현하였다. 그래핀에 전기장을 가하면

그래핀의 페르미 레벨이 이동하여 밴드 전이를 금지하는 방식으로 빛의 흡수율을 조절할 수 있다. 그래핀에 게이트 전압을 인가하여 1.5%의 투과율 변화를 확인하였다. 이 때, 유전 물질로 사용한 이온 젤은 정전 용량이 커서 낮은 게이트 전압에서 구동할 수 있다는 장점이 있다. 이어서, 그래핀의 투과율 변화를 이용하여 광자 결정 밴드에지 레이저의 전기적 변조를 구현하였다. 게이트 전압을 인가하지 않은 경우 그래핀에 의한 공진 모드의 흡수로 인해 레이저 발진이 억제 되었지만, −1.0 V의 게이트 전압을 인가한 경우에는 레이저 발진에 성공하였으며, 게이트 전압에 따른 레이저의 특성 변화를 관찰하였다. 관찰한 특성 변화 경향성은 유한차분 시간영역 시뮬레이션을 통해 계산한 결과와 일치하는 것으로 광자 결정 밴드에지 레이저의 전기적 변조를 성공적으로 잘 구현하였다. 광자 결정 밴드에지 레이저의 전기적 변조는 추후 광집적회로와 같은 광학적 시스템온칩 기술에의 적용을 기대한다.

결론으로, 이번 논문에서는 광자 결정 레이저 구조에 광 흡수체가 집적된 경우 광자 결정 공진 모드의 변화를 관찰하였다. 나아가, 광자 결정 밴드에지 레이저 구조에 집적된 그래핀 단일층의 흡수율을 조절하여 전기적 변조를 구현하였다. 위 연구 결과는 광자 결정 레이저의 공진 모드와 발진 원리에 대한 이해를 강화하고, 광자 결정 레이저의 시스템온칩 적용에 기여할 것으로 기대한다.

핵심어: 광자 결정, 광자 결정 레이저, 그래핀, 광 흡수, 전기적 변조, 파울리 차단

학번: 2010-20362